Effect of AGN on the ISM of their hosts: A multi-wavelength perspective

A Thesis

Submitted for the Degree of

Doctor of Philosophy

in the Faculty of Science

by

Payel Nandi

(01-07-00-10-11-20-1-18415)

Joint Astronomy Programme
Department of Physics
Indian Institute of Science
Bangalore – 560 012, INDIA

October 2024

Declaration

I hereby declare that the work reported in this doctoral thesis titled "Effect of AGN on the ISM of their hosts: A multi-wavelength perspective" is entirely original and is the result of investigations carried out by me under the Joint Astronomy Programme of the Department of Physics, Indian Institute of Science, Bangalore, under the supervision of Prof. Banibrata Mukhopadhyay from the Department of Physics, Indian Institute of Science and Prof. C. S. Stalin from the Indian Institute of Astrophysics.

I further declare that this work has not formed the basis for the award of any other degree, diploma, fellowship, associateship or similar title of any University or Institution.

Date: October 30, 2024
Bangalore, India

Payel Nandi
Joint Astronomy Programme
Department of Physics
Indian Institute of Science

To my grandparents and parents,

who drove it and will be most pleased

Acknowledgements

I am profoundly grateful to my parents for their unwavering sacrifices and enduring support that have made this journey possible. Though initially cautious about encouraging their daughters to pursue such an uncertain path, they wholeheartedly embraced our dreams and adjusted their expectations to match my ambitions over time. In particular, I wish to acknowledge my mother's contributions. Although she was unable to pursue her education due to family circumstances, she has always encouraged her daughters to achieve their highest potential, even when it meant challenging family expectations. Despite limited familiarity with higher studies, she has an extraordinary ability to inspire and uplift me during difficult and unexpected moments. I want to thank my elder sister, who has always been a source of inspiration and support, standing by me through every step. I also want to express my gratitude to Mr. Prasanata Mondal, my teacher in 12th grade, and the other teachers at my school who introduced me to the world of Physics. In my view, these individuals played pivotal roles in inspiring me to pursue a research career in Physics. I am equally thankful to my undergraduate and postgraduate professors, whose encouragement led me to embark on my Ph.D. journey.

A special note of gratitude goes to my M.Sc. dissertation supervisor, Prof. Sanjay Siwach, who introduced me to the Joint Astronomy Programme (JAP). Thanks to him, I decided to consider Astrophysics other than High Energy Physics and finally enrolled in the Joint Astronomy Programme at the Indian Institute of Science. I am also extremely grateful to Prof. Nirupam Roy and Prof. Banibrata Mukhopadhyay for teaching me the fundamentals of astronomy and astrophysics and Prof. Prateek Sharma for his invaluable instruction in radiative transfer, which extended my basic physics knowledge into the realm of astrophysics. The first semester of coursework made me realize that, even though I had stumbled upon this path by chance, it was the right one for me. I am deeply thankful to the founder of the JAP program, which enabled me to engage with many experts across all branches of astrophysics from four prestigious institutes in Bangalore. I also want to express my appreciation to the faculty members who took the time to explain their research and other opportunities at those

institutes. I would also like to thank the other instructors who taught during my two semesters of coursework.

Now, I would like to express my heartfelt gratitude to my supervisors, Prof. C. S. Stalin and Prof. Banibrata Mukhopadhyay. Meeting Prof. Stalin changed my perspective on mentorship; I never realized a professor could be so humble, flexible (in research topic) and patient. Over the past three years, he has supported me through all my ups and downs and has also taught me to be a better human being, just as my parents did. His constructive criticism has helped me refine my skills, particularly in coding.

Although Prof. Banibrata primarily serves as my pen-and-paper supervisor, he has always been there to assist me during challenging situations. While our work interactions have been limited, his curious questions about my observational studies have always motivated me to push further.

I also extend my gratitude to Prof. Dhruba J Saikia, another deeply knowledgeable and kind person I have been fortunate to meet in my academic journey. From the outset of my work, his insightful advice has helped my research and provided me with calm during challenging times. My thanks also go to Prof. Ram Sagar for his similar support, as well as to all my collaborators, whose advice and suggestions have helped me grow in my field. I am also thankful to all my other collaborators, Prof. Rogemar, Prof. Dominika, Prof. Markus and others whose continuous suggestions inspire me to learn many new things. I thank my comprehensive committee members, including Prof. Nirupam, Prof. Seetha, Prof. Ramadevi, and my two supervisors, Prof. Banibrata and Prof. Stalin, for their constructive comments and suggestions from time to time. At the same time, I also thank the individuals I met during different national and international workshops and conferences for their views on my work.

I also thank CSIR for supporting my journey financially and all the officials who made the process smooth. I also want to acknowledge both IIA and IISc. for their support in my attending national and international conferences, as well as all the funding agencies like COSPAR and the other conference organizers for their partial financial support.

My thanks also go to the office staff at both the IIA BGS office and the IISc. physics department office, as well as to the Deans and Directors of both institutes and all other academic staff. Special thanks go to Mr. K. Sankaranarayanan sir from the IIA BGS office, whose discreet assistance ensured smooth sailing, to Mrs. Vijayalakshmi, who treated me like her own sister, as well as Ms. Sandhya for her service. I also want to mention Prof. Maheswar Gopinathan, the BGS chair, whose suggestions and support were crucial during my time at IIA.

I want to thank the observing staff at the CREST campus and the Hanle staff for taking care of all technical issues of the HCT during observations, as well as AstroSat facilities, whose

data significantly contributed to my thesis. At the same time, I want to acknowledge the people who were behind for other observational facilities that I used for this thesis work.

I am also deeply grateful to all the staff at IIA and Bhaskara, from those in the food services (especially Manju Anna and Bimal Anna) to the electrical maintenance team for their service. Special thanks to the security guards, whose presence allowed me to work and sleep peacefully.

The library at IIA houses an extensive collection, ranging from story books to advanced-level texts in specialized areas, including foundational books on physics, mathematics, and data science. I cannot overlook its significance—without this resource, my knowledge would have been far more limited. I would also like to acknowledge the invaluable online materials and tools that have supported my learning.

I would also like to extend my heartfelt thanks to my dear friends at IIA and IISc. It would be remiss of me not to mention my wonderful seniors at IISc., who spent a lot of time helping me find my interests and suggesting potential supervisors. I am especially grateful to Amit Da, Chayan Da from IIA and Prerana Di, Ashwini Bhaiya, Sangita Di, and Tushar Da for their unforgettable advice and encouragement. The other seniors came at a later point in time but played a significant part in my journey: Bhoomika Di, Indrani Di, Kshama Di, Satabdwa Da (my elder brother at IIA; shared a maternal connection incidentally), Dhimadri Da, Swastic Da, Deepthi Di from IIA. My classmates, seniors, and beloved juniors, both at IISc. and IIA, have all been a significant part of this journey. Special thanks go to my roommate as well as my friend Saraswathi and my friends Khusbu and Nitish, who have supported me for a significant part of this journey.

I would like to express my heartfelt gratitude to my dear friends from my B.Sc. and M.Sc. days, especially Rachana, Manisha, Tanushree, Pratikshya and Pousali, who have always celebrated my academic successes even more than I did. Your encouragement has always lifted me up, especially during moments of criticism. I also extend my thanks to all my friends from school, college, and university. A special shout-out to my M.Sc. batchmates — your collective support meant the world to me during challenging times with the authorities. Without your unity, I would not have made it to this point of writing these words.

Finally, I would like to once again express my deepest gratitude to my family, including my parents, sister, brother-in-law, uncle-in-law, aunt-in-law and other relatives, whose constant support and hope have inspired me to reach this point. I also wish to honour the memory of my late grandfather, who always dreamed of seeing us achieve this success, and my late grandmother, who may no longer be with us physically but whose spirit and attitude continue to live on in us.

Lastly, I must extend my gratitude to those who have criticized me at various stages of both my academic and personal life. I may not have developed the focus and determination to

challenge and prove my capabilities without your critiques. So, if you come across this by any chance, please keep it up!

Preface

Active Galactic Nuclei (AGN) are among the high luminosity ($10^{11} - 10^{14}$ $L_{\odot}$) sources in the observable Universe, believed to be powered by the accretion of matter onto supermassive black holes (SMBHs; $10^{5} - 10^{10}$ $M_{\odot}$) at the centres of galaxies. The energy released from AGN could affect their host galaxies and their large-scale environment through a process called feedback. AGN feedback is generally invoked in galaxy formation models and simulations to explain the observed correlation between the mass of SMBHs and various host galaxy properties. A viable feedback mechanism in AGN is outflows. The driving force behind such outflows, though debated, can have an impact on the interstellar medium (ISM) of their hosts by inhibiting (negative feedback) or enhancing (positive feedback) star formation (SF). In massive galaxies, there are evidences that AGN regulate SF in their hosts via the jets, injecting energy into the gaseous halos and regulating the cooling of gas onto the galaxies. Recent observations available from a limited number of sources point to AGN having both positive and negative impacts on the SF characteristics of their hosts. However, the nature and details of the impact AGN have on the evolution of their host galaxies remain controversial and uncertain. Also, AGN affecting SF was not known in dwarf galaxies before a couple of years ago. But, only very recently, there are observational evidences of dwarf galaxies hosting AGN, thereby challenging theoretical models that generally invoke supernovae feedback in dwarf galaxies. In this thesis, we carried out a systematic investigation on a sample of AGN to find clues to (a) what triggers outflows in AGN, (b) the impact of AGN on the SF of their hosts and (c) the nature of AGN feedback in a dwarf AGN hosted by an intermediate-mass black hole (IMBH; $10^{4} - 10^{5}$ $M_{\odot}$). Towards this, we utilized imaging data from the *Chandra* X-ray Observatory, the *Ultra-Violet Imaging Telescope (UVIT)* aboard *AstroSat*, the *Hubble Space Telescope (HST)*, the *Himalayan Chandra Telescope (HCT)*, and the *Very Large Array (VLA)*. Additionally, we incorporated spatially resolved spectroscopic data in the optical and infrared bands from *Gemini* and *SDSS (MaNGA)*, as well as millimetre data from *ALMA*. The findings of this thesis are summarized in four chapters, as described below.

Chapters 1 and 2 detail the motivation of the research problem and the data and analysis methods adopted in the thesis. In Chapter 3, we tried to find the driver of ionized outflows in AGN. For this, we carried out a systematic investigation of the [O III]λ5007 emission line on a sample of AGN, consisting of radio-detected and radio-undetected sources using *MaNGA* and *Faint Images of the Radio Sky at Twenty cm (FIRST)* survey data. We found radio-detected sources to show an increased outflow detection rate compared to radio-undetected sources. We noticed a strong correlation between outflow characteristics and bolometric luminosity in both samples, except that the correlation is steeper for the radio-detected sample. Our findings suggest (a) ionized gas outflows are prevalent in all types of AGN, (b) radiation from AGN is the primary driver of ionized gas outflows, (c) radio jets play a secondary role in enhancing the gas kinematics over and above that caused by radiation and (d) SF is quenched in the very central regions of the galaxies in the sample studied due to AGN activity (Nandi et al. 2025, ApJ, 984, 20).

In Chapter 4, we investigated the impact of AGN on the SF characteristics of their hosts. This was done by mapping the star-forming regions in galaxies hosting AGN and looking for any correlations between the deduced SF and AGN properties. It is natural to expect that the influence of the central AGN on their hosts could decrease from the centre to the outskirts of the galaxies. In the nearby Universe, Seyfert and LINER type AGN are ideal targets to investigate this connection as the resolution offered by ground-based imaging observations will enable one to probe SF on scales from a few hundred parsecs to a few tens of kpc. Most studies of SF in Seyfert galaxies have been conducted in the optical, IR, or radio wavelengths using ground and space-based observatories. While there have been a few studies in the UV band using *Galaxy Evolution Explorer (GALEX)*, the resolution provided by *GALEX* is often insufficient to resolve SF on parsec scales. A limited number of studies have used the *HST*, which offers the capability to resolve parsec-scale structures, but it has a restricted field of view, making it observationally expensive to study a large number of sources comprehensively. To address this gap, we undertook a systematic investigation of the SF properties of Seyfert galaxies using *UVIT*. From an investigation of the SF characteristics on a sample of eight AGN, using *UVIT* observations, we found a positive correlation between the total surface density of SF and extinction. For five sources, we found a gradual decline of both the surface density of SF and extinction from the centre to the outer regions. We found the ratio of the star formation rate (SFR) in the nuclear region to the total SFR to be positively correlated with the Eddington ratio. This points to the influence of AGN in enhancing the SF characteristics of the hosts. This impact is found to be dominant only in the central few kpc regions with lesser effect on the larger scales probed in this thesis (Nandi et al. 2024, ApJ, 973,7).

In Chapter 5, we investigated the nature of AGN feedback on a dwarf AGN, NGC 4395. This is important, as dwarf AGN are believed to be powered by the lower mass end of SMBHs. In the literature, theoretical studies on the regulation of SF in dwarf galaxies have been attributed to radiation from young stars and supernova explosions. However, recent theoretical studies do indicate that AGN could play a significant role in regulating SF in dwarf galaxies. Observationally, there is evidence of AGN feedback operating in dwarf galaxies covering angular sizes smaller than about an arcmin. Therefore, detailed studies on SF characteristics of dwarf galaxies hosting AGN are needed, firstly, to characterize their SF properties and secondly, to find evidence of the feedback process, if any, in them. Using data from *UVIT*, we identified a total of 284 star-forming regions extending up to a distance of 9 kpc. Of those, 120 regions were also identified in the Hα continuum subtracted image. The detection of fewer star-forming regions in Hα is attributed to the lower spatial resolution as well as the shallowness of the Hα image relative to UV. On inspection of the spatial distribution of the surface density of SFR in the UV, we found three star-forming regions near the AGN that have a high surface density of SFR. One out of the three star-forming regions in the UV is also found to have a high surface density of SFR in Hα and younger age. This could possibly hint at positive feedback from the AGN. At 1.4 GHz, we found a few complexes having enhanced radio emission. These complexes contain a larger number of star-forming regions, with the majority of them having higher SFR. These complexes are known to host supernova (SN) remnants. The star-forming regions in these complexes have higher SFR in Hα and 24 μm, compared to other star-forming regions, arguing for SN-induced SF (Nandi et al. 2023, ApJ, 950, 81).

In Chapter 6, we aimed to understand the effect of jets on the ISM. There is hardly any observational evidence of jet$-$ISM interaction and its impact on the host galaxies of AGN on parsec scales. This was investigated on the dwarf AGN, NGC 4395, powered by an IMBH. Using high-resolution observations at 15 GHz from the *VLA* and the *HST*, we found evidence of radio jet$-$ISM interaction on the scale of an asymmetric triple radio structure of $\sim$ 10 pc size. The high-resolution radio image and the extended [O III]λ5007 emission, indicative of an outflow, are spatially coincident and are consistent with the interpretation of a low-power radio jet interacting with the ISM. The spatial coincidence of molecular $H_2\lambda$2.4085 along the jet direction, the morphology of ionized [O III]λ5007, and displacement of the CO(2$-$1) emission argues for conditions less favourable for SF in the central $\sim$ 10 pc region (Nandi et al. 2023, ApJ, 959, 116).

Finally, in Chapter 7, we provide a summary of the thesis work, highlighting its key findings and significance. Additionally, we discuss the unique contributions of this research and outline potential future directions that could further enhance our understanding of the topic.

List of Publications

1. **Payel Nandi**, C.S. Stalin, D.J. Saikia; *Ionized gas outflows in Active Galactic Nuclei: What causes it ?*; 2025, ApJ, 984, 20

2. **Payel Nandi**, C.S. Stalin, Poulomi Dam, D.J. Saikia; *UVIT Survey of the Host Galaxies of Active Galactic Nuclei. I. Star Formation Scenarios*; 2024, ApJ, 973, 7

3. **Payel Nandi**, C.S. Stalin, DJ Saikia, Rogemar A Riffel, Arijit Manna, Sabyasachi Pal, OL Dors, Dominika Wylezalek, Vaidehi S Paliya, P Saikia, Pratik Dabhade, Markus-Kissler Patig, Ram Sagar; *Evidence for low power radio jet induced outflow at 10 parsec in the dwarf AGN host NGC 4395*; 2023, ApJ, 959, 116

4. **Payel Nandi**, C.S Stalin, DJ Saikia, S Muneer, George Mountrichas, Dominika Wylezalek, R Sagar, Markus Kissler-Patig; *Star formation in the dwarf Seyfert galaxy NGC 4395: Evidence for both AGN and SNe feedback?*; 2023, ApJ, 950, 81

5. **Payel Nandi**, C.S Stalin; *Star formation characteristics of galaxies hosting AGN*; BSRSL, 2024, 93, 2

Acronyms

AGN	Active Galactic Nucleus/Nuclei
QSO	Quasi Stellar Object
Sy	Seyfert
LINER	Low-ionization nuclear emission-line region
FR I	Fanaroff-Riley type I
FR II	Fanaroff-Riley type II
BLRG	Broad Line Radio Galaxy
NLRG	Narrow Line Radio Galaxy
SSRQ	Steep Spectrum Radio Quasar
FSRQ	Flat Spectrum Radio Quasar
BL Lac	BL Lacertae
BLR	Broad Line Region
NLR	Narrow Line Region
SMBH	SuperMassive Black Hole
IMBH	Intermediate Mass Black Hole
UFO	Ultra-fast Outflows
ISM	Interstellar Medium
IFU	Integral Field Unit
BPT	Baldwin-Phillips-Terlevich
PSF	Point Spread Function
MS	Main Sequence
FoV	Field of View
SFR	Star Formation Rate
ISSDC	Indian Space Science Data Cente
VLA	Very Large Array
FIRST	Faint Images of the Radio Sky at Twenty-Centimeters
ALMA	Atacama Large Millimeter Array
MaNGA	Mapping Nearby Galaxies at APO
HCT	Himalayan Chandra Telescope
UVIT	UltraViolet Imaging Telescope
HST	Hubble Space Telescope
2MASS	Two Micron All Sky Survey
WISE	Wide-field Infrared Survey Explorer

Table of contents

List of figures

List of tables

1

Introduction

1.1 Active Galactic Nuclei

We are all captivated by the mesmerizing night sky, dotted with twinkling stars and distant galaxies. Many of these galaxies, including our own Milky Way, contain an active region at their core known as an Active Galactic Nucleus (AGN). These AGN are among the most luminous objects in the Universe, with luminosities ranging from 10^{40} to 10^{48} erg s^{-1} (Filippenko & Sargent, 1989; Onken et al., 2020). These powerful sources are thought to be fueled by the accretion of material onto supermassive black holes (SMBHs) located at the centres of galaxies. These black holes span a wide mass range from 10^5 to 10^{10} $M_\odot$ (Peterson, 2014; Dullo et al., 2021). They are known to show flux variations on a range of time scales from minutes to days in all observed bands from radio to $\gamma-$ray (see Ulrich et al. 1997 for review).

In 1909, Edward Fath, and later in 1917, V. M. Slipher, observed the spectrum of the galaxy NGC 1068 and identified strong emission lines that were highly unusual compared to the spectra of galaxies dominated by starlight (Fath, 1909; Slipher, 1917). These early observations hinted at the presence of energetic processes in galactic nuclei that could not be explained by stellar activity alone.

In 1943, Carl Seyfert expanded on these findings by studying six "extragalactic nebulae" and noted that they exhibited exceptionally bright nuclei and prominent broad emission lines (Seyfert, 1943). This class of galaxies was later named Seyfert Galaxies in his honor, marking a significant step in the recognition of what we now call AGN.

Interest in AGN surged during the 1950s with the detection of bright, point-like objects at radio wavelengths (Bolton & Stanley, 1948; Bolton, 1948; Smith, 1951). These early discoveries led to systematic radio surveys, such as the Third Cambridge (3C) (Edge et al., 1959) and 3CR surveys (Bennett, 1962, 1963), which revealed a broader population of quasars and radio-loud AGN.

The discovery of optical counterparts to radio sources, such as 3C 48 (Greenstein, 1963) and 3C 273 (Schmidt, 1963; Hazard et al., 1963; Oke, 1963), demonstrated that these objects were not stars but extremely luminous extragalactic sources with significant redshifts, confirming their vast distances. This revelation marked the recognition of quasars as a subclass of AGN. Radio galaxy 3C 295 was also identified as a distant, highly energetic source, further linking radio emissions to AGN (Minkowski, 1960).

In 1959, Woltjer (1959) proposed that the immense energy output of these extragalactic sources could be explained by the concentration of a massive 10^8 $M_\odot$ object within the central 100 pc of the galaxy. By 1963, Hoyle & Fowler (1963) introduced the concept of accretion, suggesting that gas surrounding this massive object, moving at high velocities, could release enormous energy as it fell inward.

The theoretical breakthrough came when the enormous luminosities observed in AGN were linked to the presence of supermassive black holes (SMBHs) at their centres. Salpeter (1964) and Zel'dovich & Novikov (1964) proposed that accretion onto SMBHs, where matter is heated to extreme temperatures as it spirals inward, could explain the observed energy output. These ideas laid the foundation for the modern understanding of AGN as systems powered by accretion onto SMBHs.

This theoretical hypothesis gained further support in the late 1960s with the detection of X-ray emission from known radio sources. The first sources, M87 and 3C 273, were identified as X-ray emitters, followed by NGC 5128 (Friedman & Byram, 1967; Bowyer et al., 1970), detected using a Geiger counter aboard Aerobee sounding rockets (Giacconi et al., 1962). The launch of the first dedicated X-ray astronomy satellite, Uhuru, facilitated the discovery of many more AGN emitting X-rays, paving the way for the understanding of non-thermal emission from galactic centres (Gursky et al., 1971; Tucker et al., 1973). The first gamma-ray detection from an AGN, 3C 273, was made by *COS-B* satellite (Swanenburg et al., 1978). Later, with the launch of the *EGRET* (*Energetic Gamma-Ray Experiment Telescope*) aboard the *Compton Gamma Ray Observatory* (*CGRO*) in 1991, many more extragalactic gamma-ray

sources, dominated by the blazar category of AGN, were identified (von Montigny et al., 1995). These gamma rays are from AGN and are mostly beamed and nonthermal.

1.2 AGN Taxonomy: Different types and their characteristics

Historically, AGN were classified as radio-loud or radio-quiet based on their radio-to-optical flux density ratios. A vast majority of about 85% of AGN are radio-quiet, with only a minority of about 15% being radio-loud. Radio-loud AGN are about 10^3 times brighter in the radio band compared to radio-quiet AGN. This apparent radio-loud/radio-quiet dichotomy is still debated, though it was proposed about five decades ago. It has been recently proposed that AGN may be better classified as jetted and non-jetted AGN (Padovani, 2017).

1.2.1 Radio-quiet AGN

Among the radio-quiet AGN are Seyfert galaxies and radio-quiet quasars. Radio-quiet quasars are the high luminosity counterparts of Seyfert galaxies with the dividing line set with an absolute B-band brightness of -23 mag. Seyfert galaxies are low luminous sources with $M_B > -23$ and quasars are high luminosity sources with $M_B < -23$ (Schmidt & Green, 1983).

1.2.1.1 Seyfert galaxies

These sources exhibit strong emission lines in their spectra, first identified by Carl Seyfert in 1943. They are categorized into Seyfert 1 and Seyfert 2 galaxies based on the optical emission lines observed in their spectra. Seyfert 1 galaxies display both broad permitted lines and narrow forbidden lines, while Seyfert 2 galaxies show only narrow emission lines. The broad lines in Seyfert 1 galaxies are caused by photoionization of clouds in the Broad Line Region (BLR; see section 1.3), whereas the narrow emission lines originate from photoionized gas clouds located farther from the central engine in the Narrow Line Region (NLR; see section 1.3; Khachikian & Weedman 1974a; Koski 1978).

A subclass within Seyfert 1 galaxies, called narrow-line Seyfert 1 galaxies, was first identified by Osterbrock and collaborators about forty years ago. These galaxies are distinguished by their narrow Hβ emission lines with a full width at half maximum of less than 2000 km s^{-1}, weak [O III]λ5007 lines relative to Hβ with an [O III]λ5007/Hβ ratio less than 3, strong Fe II emission, and a relatively low black hole mass in the range of $10^6 - 10^8$ $M_\odot$ (Osterbrock & Pogge, 1985; Mathur, 2000).

1.2.1.2 Radio-quiet quasars

They are the luminous counterparts to Seyfert galaxies with bolometric luminosities of the order of $10^{44} - 10^{47}$ erg s^{-1}. They have a strong continuum in the optical and X-ray bands, along with broad and narrow emission lines in their optical spectra. Based on the optical lines, they are also classified as Type 1 quasars (analogous to Seyfert 1 galaxies) and Type 2 quasars (analogous to Seyfert 2 galaxies).

1.2.1.3 LINERs

Low-ionization nuclear emission-line regions (LINERs) are sources that show strong low-ionization emission lines, with the emission of higher ionization lines being relatively weaker. They are very common, with about one-third of the galaxies in the local Universe being LINERs (Heckman, 1980).

1.2.2 Radio-loud AGN

Among the radio-loud category, AGN are broadly classified as radio galaxies and blazars based on their morphology and spectral features.

1.2.2.1 Radio galaxies

Radio galaxies are a type of AGN that emit large amounts of energy in the radio wavelengths of the electromagnetic spectrum. This emission primarily comes from jets of charged particles and extensive radio lobes that can stretch millions of light-years beyond the host galaxy, making radio galaxies some of the largest structures in the Universe.

Radio galaxies are classified based on morphology, radio luminosity, and spectral characteristics. Based on radio morphology and brightness distribution in their lobes, they are divided into FR I and FR II classes (Fanaroff & Riley, 1974). FR I galaxies have a bright, compact core with diffuse radio lobes, while FR II galaxies are more powerful than FR I galaxies; they have brighter radio lobes with prominent hotspots where the jets terminate. Based on spectral line features, they are classified as Broad Line Radio Galaxies (BLRGs) when broad lines are present and Narrow Line Radio Galaxies (NLRGs) when only narrow lines appear.

Some radio galaxies exhibit very steep radio spectra (spectral index < -0.5) and are known as Steep Spectrum Radio Quasars (SSRQs), and some are relatively flat (typically close to zero or $\alpha \gtrsim -0.5$) and are known as flat spectrum radio quasars (FSRQs).

1.2.2.2 Blazars

They are a peculiar category of radio-loud AGN. They emit over the entire range of the electromagnetic spectrum, with the emission from them dominated by the boosted non-thermal emission from their relativistic jets oriented at small angles to the line of sight to the observer. However, sub-dominant emission from the accretion disk, as well as emission lines from the BLR, are also visible (Cerruti, 2020). They are further divided into flat spectrum radio quasars (FSRQs) and BL Lac objects. While FSRQs have emission lines in their spectra, BL lacs either have weak or no emission lines.

The classification of sources is given in Fig.1.1.

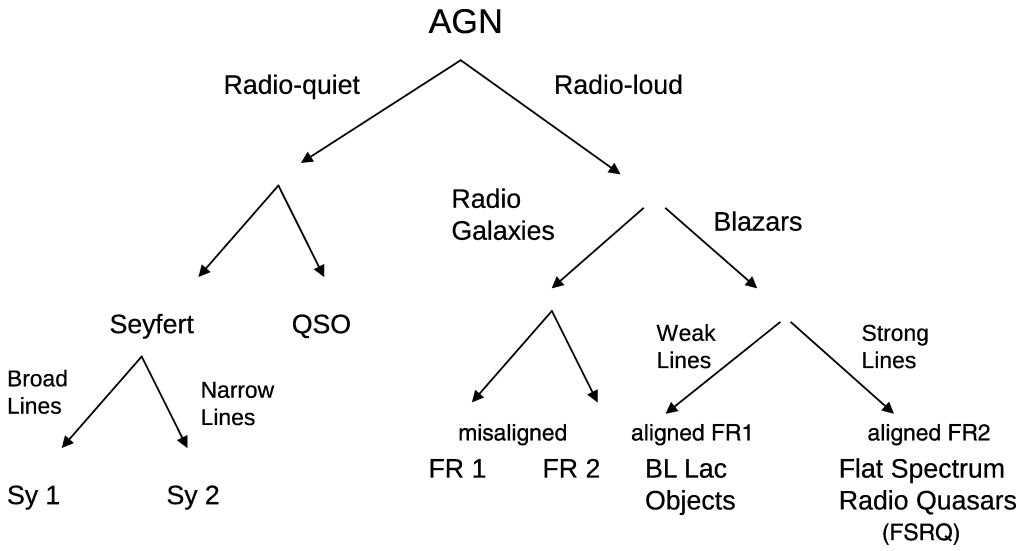

Fig. 1.1 An illustration of AGN taxonomy. Credit: Dermer & Giebels (2016)

1.3 Fundamental Constituents of an AGN

The unification model of AGN posits that the observed differences in the spectrum between different classes of AGN are due to orientation effects. According to the unification scheme (Urry & Padovani, 1995), all AGN either in the radio-loud or radio-quiet category are fundamentally the same, but their appearance varies based on our line of sight, leading to their classification into different types. The constituents of AGN are shown in Fig. 1.2.

They consist of a central black hole, a hot corona, an accretion disk, and a dusty torus, which together produce the observed continuum emission. The hot corona, which is much hotter than the accretion disk, emits predominantly in X-rays. The accretion disk, with temperatures around $10^4 - 10^5$ K, emits UV-optical photons and follows a multi-temperature blackbody

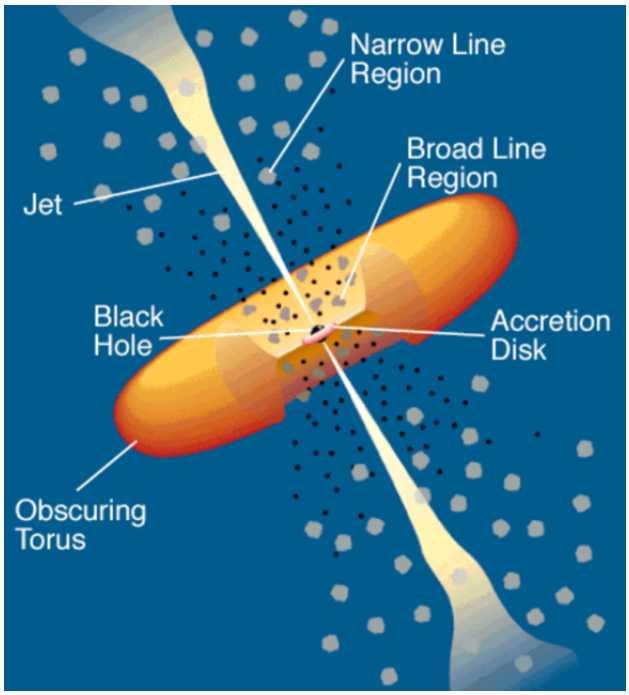

Fig. 1.2 Schematics of different regions of an AGN according to Urry & Padovani (1995).

distribution, appearing as an excess in the U band (3000−4000 Å), often referred to as the "big blue bump" (Abramowicz & Fragile, 2013). The torus, cooler than the accretion disk, is composed of dust and particles arranged in a doughnut-shaped structure around the disk. UV-optical photons from the accretion disk are reprocessed by the dusty torus and re-emitted in the infrared, creating the "infrared hump" in the spectrum (Edge et al., 1959; Peterson, 1997). AGN also contain clumpy regions called BLR and NLR, responsible for the broad and narrow emission lines observed in the UV, optical, and infrared parts of the spectrum. The BLR, located close to the accretion disk, has a high electron density ($10^5 - 10^7 \mathrm{cm}^{-3}$) and produces broad lines in the optical and infrared due to the dynamic behaviour of a gas under the strong gravitational effect of the central black hole. In contrast, the NLR, located farther from the central engine, has a temperature of around 10,000 K and an electron density of $10^3 - 10^4$ cm^{-3}. The NLR is responsible for strong forbidden emission lines, in addition to hydrogen lines, and can extend over kpc scales (Edge et al., 1959; Peterson, 1997). AGN also consists of highly collimated beamed radiation, which is called a jet. This jet, composed of relativistic charged particles, produces synchrotron emission observed mainly in the radio band; however, it is also observed in optical, UV, X-ray and γ-ray bands for some objects. These jets can extend from parsec scales to well beyond the host galaxy. The broad-band emission from AGN with contribution from different regions is shown in Fig. 1.3.

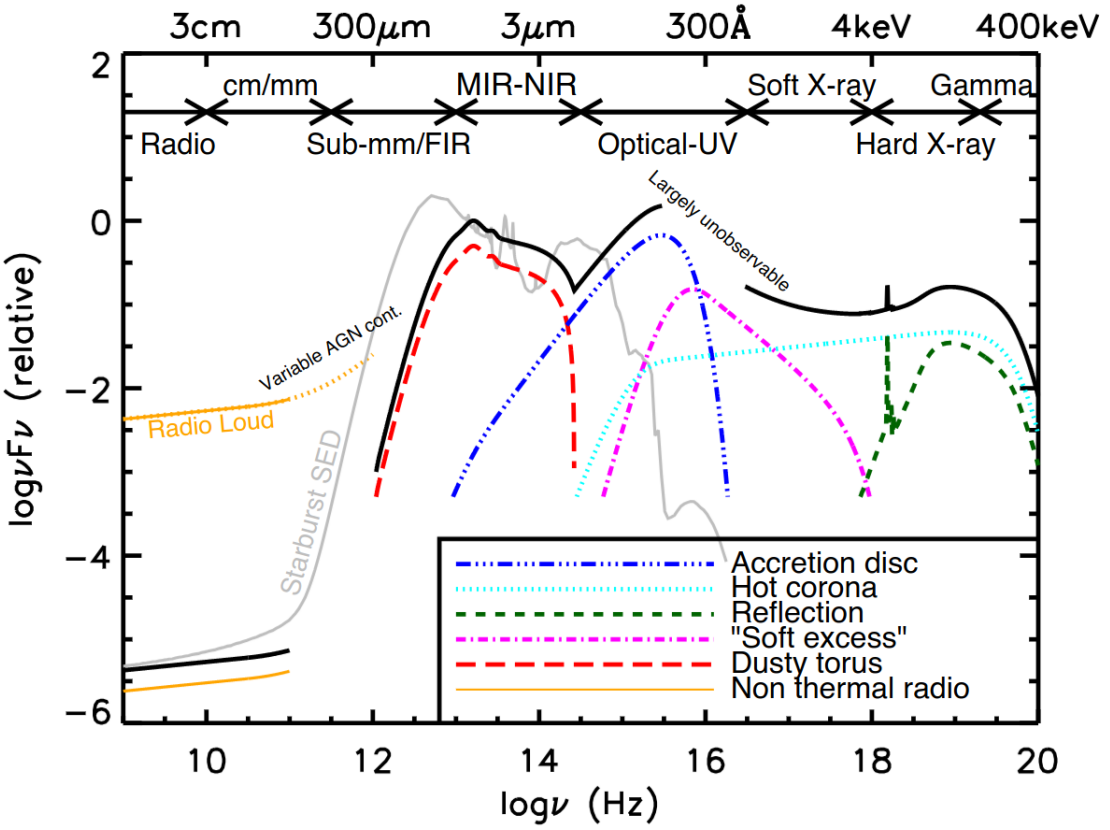

Fig. 1.3 Schematic diagram of the total spectral energy distribution of AGN. Here, emission from different regions of AGN are shown with different lines and colours. Credit: Harrison (2014)

1.4 AGN versus host galaxy evolution

The concept of black holes as astrophysical objects was popularized in the 1960s following theoretical work by John Wheeler, Roger Penrose, and Stephen Hawking, among others. At first, black holes were thought to be relatively isolated phenomena, not directly connected to galaxy formation or evolution. The discovery of quasars in 1963, which are powered by accretion onto SMBHs, hinted at the possibility that black holes could reside in galaxy centres, but their connection to host galaxy properties remained unclear at that time.

A major turning point came in 1998, Magorrian et al. (1998) found that black hole mass (M_{BH}) is correlated with the mass of the bulge (M_{Bulge}) of the host galaxy by analyzing a sample of 36 nearby AGN using observations from the Hubble Space Telescope (HST). Later, Gebhardt et al. (2000) discovered a strong correlation between M_{BH} and the stellar velocity dispersion (σ_e) within a half-light radius ($M_{BH} \propto \sigma_e^{3.75\pm0.3}$) in a study of 26 AGN host galaxies. Following this, Marconi & Hunt (2003) identified a tight relationship between M_{BH} and bulge luminosity

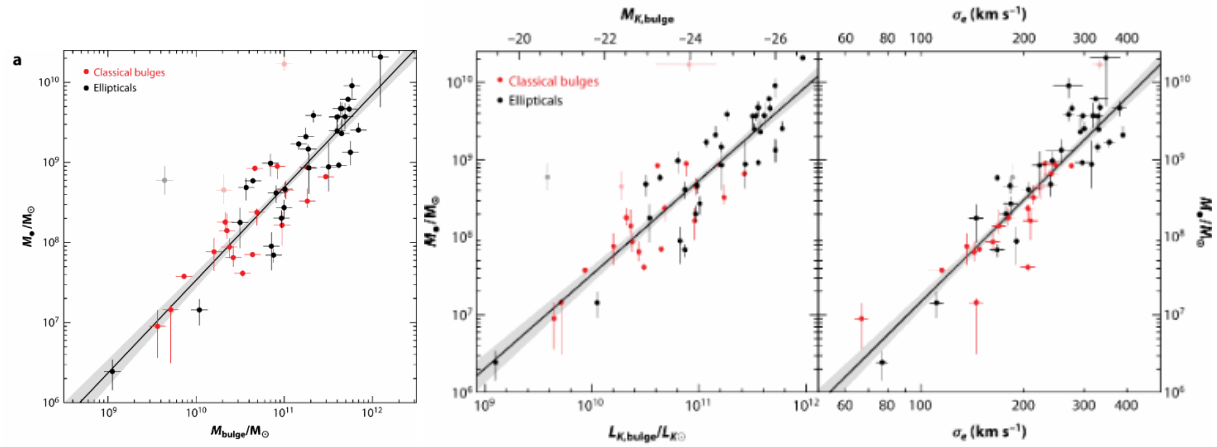

Fig. 1.4 Corelation between M_{BH} and bulge properties. Credit: Kormendy & Ho (2013)

(L_{Bulge}), M_{Bulge}, and stellar velocity dispersion within effective radius. In 2013, Kormendy & Ho (Kormendy & Ho 2013) further refined these relations and the established correlations between M_{BH} and various properties of bulges, including M_{Bulge}, L_{Bulge} and stellar velocity dispersion within the bulge (σ). The relations are $M_{BH} \propto M_{Bulge}^{1.17\pm0.08}$, $M_{BH} \propto L_{Bulge}^{1.22\pm0.08}$, and $M_{BH} \propto \sigma^{4.38\pm0.29}$. These scaling relations are fundamental in understanding the co-evolution of black holes and their host galaxies, as can be seen in Fig. 1.4 (see Kormendy & Ho 2013 for a review).

The $M_{BH} - \sigma$ relation is often seen as the tightest correlation, implying that dynamical processes, like the central bulge's velocity dispersion, play a key role in regulating black hole growth. On the other hand, the $M_{BH} - M_{Bulge}$ and $M_{BH} - L_{Bulge}$ relations emphasize the connection between the bulge of the galaxy and its central black hole. These scaling relations suggest that the growth of SMBHs and the stellar bulge are co-evolutionary processes, likely regulated by common mechanisms such as AGN feedback, mergers, and gas accretion.

1.5 AGN interact with their host galaxies: Role of outflowing materials

The process of accretion in AGN which leads to the release of enormous amounts of energy in the form of radiation (Lynden-Bell, 1969) as well as particles via relativistic jets (Cattaneo & Best, 2009), though, in a small fraction of AGN, is believed to affect their host galaxies via a process called feedback. AGN feedback is invoked to explain the observed correlation between M_{BH} and various host galaxy properties (Zhuang & Ho 2023 and references therein). Such feedback processes are also found to be operative in dwarf galaxies (Schutte & Reines, 2022).

A viable feedback mechanism in AGN is outflows. These outflows are dynamic phenomena, representing the expulsion of vast amounts of matter and energy from the vicinity of SMBHs at the centres of galaxies. They play a critical role in shaping the surrounding environment and influencing the evolution of galaxies (Guo et al., 2023).

They are multifaceted, seen in molecular, neutral and ionized gas (Riffel et al., 2023; Su et al., 2023) and can occur on various scales, spanning from relatively small-scale winds to colossal jets extending over intergalactic distances (Harrison et al., 2014; Izumi et al., 2023). Ultra-fast outflows (UFOs), the hottest phase, reach velocities exceeding 10,000 km s^{-1} and are detected in X-ray spectra, mainly through blue-shifted Fe Kα in emission or strong blue-shifted absorption in high ionization lines such as Fe XXV or Fe XXVI. They are thought to originate very close to the central black hole, likely from the inner accretion disk. Warm ionized outflows are found through mainly forbidden lines in optical and infrared observations, such as [O III]λ5007 and coronal lines, such as [Fe VII] and [Fe X] in the infrared. They are slower ($500-2000$ km s^{-1}) and extend up to several kpc. The molecular phase represents the coldest component of AGN outflows. These outflows are traced primarily by asymmetric absorption in molecular lines such as CO or OH for cold phases and for warm phases via roto-vibrational H_2 lines in the infrared. They are typically slower than their ionized counterparts, originate near the torus and have velocities ranging from a few 100 to 1000 km s^{-1} and extend beyond the nucleus. Neutral outflows are observed in 21 cm absorption lines in radio, sometimes through NaI D absorption lines in the optical (Davies et al., 2024).

These outflowing materials introduce turbulence into the galaxy's ISM during their propagation through the galaxy, which can disrupt the orderly motion of gas clouds, altering SFR and potentially influencing the galaxy's future development. These outflows can deplete a galaxy's reservoir of cold molecular gas, the raw material for star formation, either by expelling it or heating it so that it no longer forms stars efficiently, a process called negative feedback (Maiolino et al., 2012). This is one of the main reasons for the existence of "red and dead" galaxies in the Universe, where AGN activity has halted the process of star formation, leaving behind only older stars. Alternatively, outflows can also compress the gas, leading to enhanced star formation, especially in the galaxy's central regions, a process called positive feedback (Nesvadba et al., 2020; Maiolino et al., 2017). The feedback process can be understood in Fig. 1.5.

This feedback can also affect the overall structure of their host galaxies. For example, AGN jets or large-scale, powerful winds can create cavities in the hot gas halo of a galaxy, which may influence the dynamics of gas accretion and the morphology of the galaxy over time.

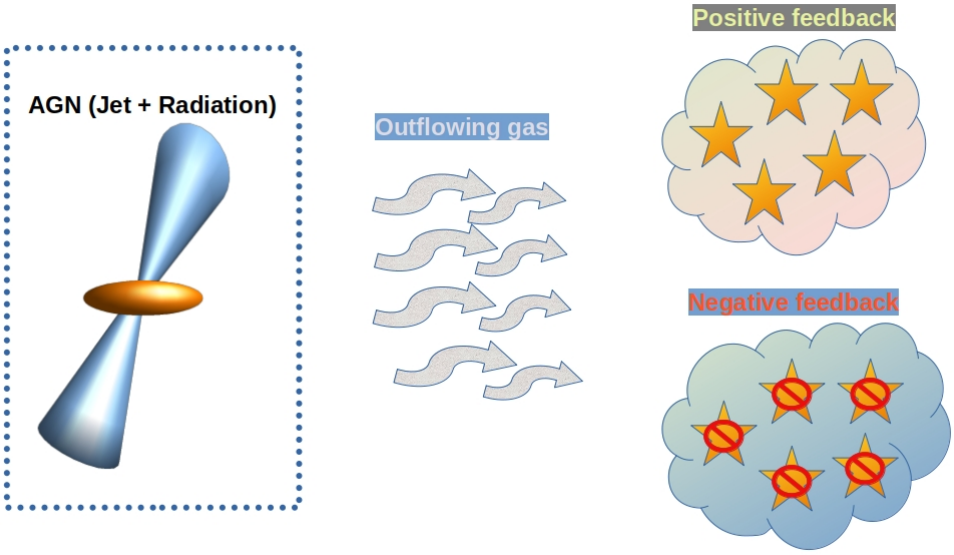

Fig. 1.5 A schematic representation illustrating how AGN (depicted within the blue dotted box) interact with their host galaxies through outflowing gas, influencing them via positive feedback (represented by the yellowish cloud) and negative feedback (represented by the bluish cloud). The blue dotted box encompasses the AGN components, including radiation from the accretion disk and jets, which collectively drive the outflowing gas. Note: The orientation of the jets and outflowing gas in this diagram is purely illustrative and does not convey specific information about the angle between them. Credit: Payel Nandi

1.6 Star formation in AGN host galaxies

The activity of AGN can have an effect on the star formation characteristics of their host galaxies. There are a few parameters through which star formation activities have been understood, such as star formation rate (SFR), age of the stellar population, metallicity, etc. The SFR of a galaxy is an important parameter. Several SFR measures are available in the literature (Calzetti, 2013b; Kennicutt & Evans, 2012). Observationally, the star formation nature of a galaxy can be characterized by measuring its luminosity, which can then be used to find the number of O and B stars. Because of their high luminosity and temperature, Ultra-Violet (UV) observations are the most straightforward SFR indicator. Alternatively, Hα observations in the optical are generally used to estimate SFR (Kennicutt, 1998). As UV photons, and to a lesser extent optical photons, are affected by dust attenuation, observations at other wavelengths are also used to estimate SFR. Other estimators of SFR are via the radio and infrared (IR) emission emitted from the star-forming regions (Kennicutt & Evans, 2012; Calzetti, 2013b). The radio

emission from such regions can be due to thermal free-free (bremsstrahlung) and non-thermal (synchrotron) processes (Condon, 1992). An advantage of using radio emission to trace SFR is that it is free from dust extinction, unlike the observations in the UV and optical bands that are sensitive to dust.

Star formation in AGN host galaxies is influenced by a variety of factors, including the type of AGN, the strength of feedback mechanisms, and the presence of molecular gas. While powerful AGN like quasars and FR II radio galaxies tend to suppress star formation, lower-luminosity AGN like Seyferts and LINERs can coexist with star-forming regions. In cases like ultraluminous infrared galaxies, intense star formation and AGN activity can occur simultaneously, often as part of galaxy mergers. The net effect of AGN on star formation is a balance between negative feedback (quenching) and positive feedback (triggering), and it varies across different AGN types.

Seyferts and LINERs are sources ideally suited to study star formation in galaxies hosting AGN. But LINERs typically show lower-luminosity AGN activity with weaker outflows, leading to less significant feedback compared to quasars or Seyferts. In the Seyfert category of AGN, circumnuclear star formation is commonly observed (Davies et al., 1998; Álvarez-Álvarez et al., 2015; Hennig et al., 2018; Diniz et al., 2019). However, works to clarify the relationships between the central AGN and star formation in their surroundings are still ongoing. There are suggestions for causal and evolutionary connections. The difficulty in establishing the connection is due to differences in the spatial and temporal scales between AGN and starburst activities. Available studies on AGN hosts probe star formation on scales of kpc to a few hundreds of pc (Riffel et al., 2022; Venturi et al., 2021). However, accretion processes that feed the AGN occur on scales of the order of pc. The influence AGN have on their host galaxies is expected to decrease with an increase in the distance of the regions from the central AGN (Tsai & Hwang, 2015). Therefore, to establish the connection between AGN and star formation activities, one needs to probe different spatial scales in the hosts of AGN.

1.7 Our current understanding on star formation and outflows in AGN

There are a number of studies in the literature that focus on star formation properties of Seyfert type AGN using optical observations (Davies et al., 1998; Gu et al., 2001; Hennig et al., 2018). They have also been studied for star formation for more than three decades in different spatial scales as well as at different wavelengths (Cid Fernandes et al., 2004; Davies et al., 2007; Bing et al., 2019; Riffel et al., 2022; Zhang & Ho, 2023). Despite years of research, the nature of star

formation in AGN host galaxies versus normal galaxies is not settled and is highly debated. For example, in a dwarf galaxy, He 2−10 with a central SMBH, Schutte & Reines (2022) found AGN-driven outflows triggering star formation at the central region, causing positive feedback. Considering the far-infrared emission to be due to star formation, Rodriguez Espinosa et al. (1987) found that the far-infrared luminosities of Seyfert galaxies and star-burst galaxies are indistinguishable arguing for the bulk of the far-infrared emission in Seyfert galaxies to be due to star formation. Alternatively, García-González et al. (2016) found that in a few of the Seyfert galaxies studied by them, the bulk of the nuclear far-infrared luminosity is contributed by the dust heated by the AGN. Cid Fernandes et al. (2004) studied star formation history extensively in Seyfert 2 galaxies and found that they are heterogeneous and hosts a mixture of young, intermediate and old stellar populations.

Studies are available in the literature aimed at identifying the main driving mechanism for outflows. They are focused on individual systems as well as on samples of sources. For example, the correlation noticed between the ionized [O III]λ5007 gas outflow and the radio jet in NGC 1068 seems to favour a jet-driven outflow (García-Burillo et al., 2014; Venturi et al., 2021). In IC 5063, Morganti et al. (2015) found evidence of molecular, atomic and ionized outflows and concluded that both the radiation and jet could drive the outflow, however, the jet being the dominant driver. Other studies that find favour of jets triggering outflows include that of NGC 1337 (Aalto et al., 2016), a sample of 10 quasars at $z < 0.2$ (Jarvis et al., 2019), 3C 273 (Husemann et al., 2019), ESO 420−G13 (Fernández-Ontiveros et al., 2020), NGC 5643 (Venturi et al., 2021) and NGC 1386 (Venturi et al., 2021). However, observations of Mrk 231 support radiation from accretion driving the outflow (Feruglio et al., 2015). While the above studies are focused on using high-resolution observations, low spatial resolution studies do exist. Mullaney et al. (2013) from analysis of a larger sample of quasars using the Sloan Digital Sky Survey (SDSS) spectra, found that sources more luminous in radio band tend to have broader [O III]λ5007 line profile, while, Zakamska & Greene (2014) found favour of outflows being driven via radiative output from quasars. From an analysis of SDSS spectra of Type 2 AGN, Woo et al. (2016) found that while outflows are prevalent in them, they are not directly related to radio activity. Alternatively, from an analysis of the SDSS spectra of radio AGN, Kukreti et al. (2023) found that radio jets are more effective in driving outflows when they are young. Molyneux et al. (2019) too found that the chance of finding outflows is more in compact radio sources possibly hosting young radio jets. Recently, from an analysis of a large sample of AGN, Liao et al. (2024) found the outflow velocity to correlate with radio power. However, Ayubinia et al. (2023) conclude that both accretion and radio activity can have a role in driving outflows.

Thus, observations available from a limited number of sources in the literature as of now, point to AGN having both positive and negative impacts on the star formation characteristics of their hosts. However, the nature and details of the impact AGN have on the evolution of their host galaxies remain controversial and uncertain. Also, AGN affecting star formation was not known in dwarf galaxies a couple of years ago. But, only very recently, there are observational evidences of dwarf galaxies hosting AGN, thereby challenging theoretical models that generally invoke supernovae feedback in dwarf galaxies. Similarly, studies in the literature aimed at finding the driver of outflows, whether radiation or jet, have focussed on the comparison between radio-loud and radio-quiet quasars. But radio-quiet quasars are found to have radio jets that could impact the outflow. Also, the separation of quasars into radio-loud and radio-quiet is questioned, and an alternative division of AGN into jetted and non-jetted sources is proposed (Padovani, 2017). Thus, the driver for outflows in AGN also remains unsettled.

1.8 Scientific objectives and outline of the thesis

To overcome the limitations, as outlined earlier, in our understanding of the complex interplay between AGN and their host galaxies through star formation, outflows as well as jet−ISM interaction and motivated by the availability of multi-wavelength data and spatially resolved spectroscopic data, in this thesis, I aimed to address the following

1. *What drives outflows in AGN?* This is addressed in Chapter 3. For this, I carried out a systematic investigation of the [O III]λ5007 emission line on a sample of AGN, consisting of radio-detected and radio-undetected sources using *Mapping Nearby Galaxies at Apache Point Observatory (MaNGA)* and *Faint Images of the Radio Sky at Twenty-Centimeters (FIRST)* survey data.

2. *What is the impact of AGN on the star formation of their host galaxies?* For this, I undertook a systematic investigation of the star formation properties of Seyfert galaxies using the *Ultra Violet Imaging Telescope (UVIT)* and ground-based Hα observations. My sample consists of seven Seyferts and one LINER. I present the results of this in Chapter 4, which aims to understand the complex connection between AGN activity and star formation characteristics of their host galaxies.

3. *What is the nature of feedback in a dwarf AGN?* For this, in Chapter 5, I carried out detailed studies on the star formation characteristics of a dwarf AGN, NGC 4395, firstly to characterise its star formation characteristics and secondly to find evidence of feedback processes in it, if any. For this, data from a range of wavelengths were used.

4. *What is the effect of low-power radio jets in the ISM of their hosts?* There is hardly any observational evidence of jet−ISM interaction and its impact on the host galaxies of AGN on pc scales. Towards addressing this issue in Chapter 6, I carried out a detailed analysis of the dwarf AGN, NGC 4395, that is powered by an intermediate-mass black hole. For this, I used data from low-energy radio/mm to high-energy X-rays.

2

Data Acquisition and Processing

This thesis used multi-band data in X-ray, UV, optical, infrared, radio and millimetre wavelengths acquired using both ground and space-based telescopes. In X-ray, we used the high-resolution imaging data acquired from the *Chandra Observatory* operated by NASA. For UV, we used the data from the *UVIT* onboard *Astrosat*, India's multi-wavelength astronomical observatory. In the optical band, we used imaging observations carried out with the *HST* and the ground-based *Himalayan Chandra Telescope (HCT)*, owned and operated by the Indian Institute of Astrophysics, Bangalore. For spatially resolved spectroscopic data, in the optical band, we used the observations acquired with the *Gemini Multi-Object Spectrograph (GMOS)* instrument in *Gemini-North telescope* and the *MaNGA* survey data from *SDSS*. In the infrared, we used the Near-infrared spectroscopic instrument in the integral field unit (IFU) mode at the *Gemini-North telescope*. In the radio band, we used the data acquired with the *Very Large Array (VLA)* operated by *National Radio Astronomical Observatory (NRAO)*, while for the millimetre band, we used the high-resolution data from *Atacama Large Millimeter Array (ALMA)*. Details of the observations and/or data and the procedures adopted to reduce the observations acquired at different wavelengths are described in the subsequent sections.

2.1 X-ray data

We used the archival X-ray data in the energy range of 0.5−7 keV, acquired with the *Advanced CCD Imaging Spectrometer (ACIS)* on the *Chandra* X-ray Observatory (Weisskopf et al., 2002). We reduced the data using the Chandra Interactive Analysis of Observations (*CIAO*, version 4.14) software and calibration files (*CALDB* version 4.9.8) [1]. We reprocessed the data by running the task *chandra_repro* to generate the cleaned and calibrated event files. We then combined the event files, computed the exposure maps and generated the exposure-corrected image at different energy bands (broad-band: 0.5−7 keV; soft band: 0.5−1.2 keV, medium band: 1.2−2.0 keV and hard band: 2.0−7.0 keV) using the task *merge_obs*.

2.2 Ultraviolet

The UV observations for the sample studied in this thesis were from *UVIT*. *UVIT* observes simultaneously in the far UV (FUV; 1300−1800 Å) and the near UV (NUV; 2000−3000Å) over a $\sim 28'$ diameter field with a spatial resolution better than $1.5''$ in multiple filters. The FUV and NUV channels operate in the photon counting mode, while the visual channel (VIS; 3200−5500 Å) operates in the integration mode. Images from the VIS channel are used to monitor the drift of the satellite. We used the science-ready data available in the archives of the *Indian Space Science Data Center (ISSDC*[2]). These science-ready images were generated by the *UVIT* Payload Operations Center (*UVIT*-POC) using the *UVIT*-L2 pipeline (Ghosh et al., 2022) and transferred to *ISSDC* for archival and dissemination.

For most of the sources, the filter-wise combined images taken from *ISSDC* have exposure time smaller than the sum of the individual orbit-wise images. Also, the final astrometry has large errors. Therefore, we first aligned the individual images using the *Image Reduction and Analysis Facility* (IRAF; Tody 1986) and combined those aligned individual images to create the combined image filter-wise. Astrometry on the combined images was carried out using stars available on the image frames with their (α, δ) positions taken from *Gaia-DR3* (Gaia Collaboration et al., 2022) through custom developed *Python* scripts. These astrometrically corrected combined image frames were used for further analysis. The measured counts/sec of the sources of interest were converted to physical units using the calibrations given in Tandon et al. (2020). For objects observed multiple times, to generate the final combined images, we used only those orbit-wise images that had sufficient signal.

[1] https://cxc.cfa.harvard.edu/ciao/threads/
[2] https://astrobrowse.issdc.gov.in/astro_archive/archive/Search.jsp

2.3 Optical

2.3.1 HCT

Narrow-band Hα imaging observations for some of the sources studied in this thesis were carried out using the *Himalayan Faint Object Spectrograph and Camera (HFOSC)* mounted on the 2m *HCT*, situated at the Indian Astronomical Observatory, Hanle, India (Prabhu, 2014). For our study, we used two narrow-band filters centred at 6563 Å and 6724 Å each with a bandwidth of 100 Å. In addition to the two narrow-band filters, we also acquired data through one broad R-filter whose central wavelength is 6020 Å and bandwidth is 1000 Å. The detector is a 2k×2k CCD with a pixel scale of 0.296″, thereby covering $10' \times 10'$. For our observations, we used Amplifier A in high gain mode. The gain and readout noise for this configuration is 1.22 e^-/ADU and 4.8 e^-. The typical seeing observed through this telescope is 1.5″.

We reduced the data from *HCT* using the standard procedures in *IRAF* (Tody, 1986). In the first step, we trimmed each frame, including bias, flat and science frames. For flat, we used twilight during the start and end of the observation. Then we followed median combined method using `Zerocombine` task in `noao.imred.ccdred` in IRAF and got a master-bias for each day of observation. After getting the master-bias, we subtracted it from all the frames, including science and flat frames. Then, we combined (median) all the flat frames and created a master-flat for corresponding filters each day using the `flatcombine` task of the previous package in IRAF, followed by normalising the master flat and getting a normalised master-flat. Then, we corrected each science frame for the pixel-to-pixel sensitivity using the normalised master-flat. Finally, after correcting all the detector and electronic noise, we aligned frames and stacked them for each target. And we got the corrected combined frame for each target. Then, finally, we performed astrometry using `ccmap` and `ccsetwcs` and coordinates from Gaia DR3 catalogue (Gaia Collaboration et al., 2022). Now, we have science-ready images for each filter. For calibrating the narrow-band Hα observations, we also observed one standard spectrophotometric star, Feige 66. We convolved the observed spectrum of Feige 66 from Oke (1990) with the Hα filter response and estimated the magnitude. The derived magnitude in the Hα observation was converted to a standard magnitude using the difference between the instrumental and standard magnitude of Feige 66. To get the standard magnitude in the R band, we used the technique of differential photometry in conjunction with the relations from *SDSS*. The transformation equations from *SDSS* were used to get the standard R-band magnitude of a few stars in the acquired R-band image based on their *SDSS* u, g, r, i, and z magnitudes.

2.3.2 HST

We also used the archival *WFC3-UVIS2* filter image from *HST* [3] for our study. We mainly used the data in two filters, one F502N, which is centred at 5009.87 Å and the other F547M, which is centred around the nearby continuum at 5756.9 Å.

2.3.3 GMOS/Gemini-North

We used the archival data from *GMOS* (Hook et al., 2004) in *Gemini-North*. *GMOS* with a field of view (FoV) of $5.0'' \times 3.5''$ covers the spectral range from 4500−7300 Å. The data cubes in *GMOS* observations have a spatial sampling of $0.05''$/pixel. The spectral resolution is 90 km s^{-1} and the angular resolution is $0.5''$.We processed the *GMOS* data using the *GEMINI.GMOS* package in *IRAF* (refer to Brum et al. 2019 for details). The reduction steps included trimming the frames, applying bias corrections, and performing flat-field corrections, following a procedure similar to that described in Section 2.3.1. Wavelength calibration was carried out using the arc lamp, and flux calibration was performed using a standard star.

2.3.4 MaNGA/SDSS

We also used optical IFU data from *MaNGA* (Bundy et al., 2015) survey. It uses a fibre-based IFU spectroscopic technique. *MaNGA* has observed 10,010 unique sources with redshift 0.01 to 0.15 (Wake et al., 2017), in different IFU configurations. The FoV varies from $12''$ to $32''$ depending upon its IFU configurations. The spatial resolution is between $2''$ to $2.5''$ with a pixel scale of $0.5'' \times 0.5''$. It covers the wavelength range of 3600−10000 Å with a spectral resolution ($\lambda/\Delta\lambda$) of ≈2000.

2.4 Infrared

In the infrared band, we used archival data in J, H and Ks bands from the *Two Micron All Sky Survey (2MASS*; Skrutskie et al. 2006) and the W1(3.4 μm), W2(4.6 μm), W3(12 μm) and W4(22 μm) bands from the *Wide-field Infrared Survey Explorer (WISE*; Wright et al. 2010). Also, in the far-IR, we used data at 24μm, 70μm, and 160 μm from the *Multiband Imaging Photometer for Spitzer (MIPS)* instrument (Rieke et al., 2004) on *Spitzer*. The measurements obtained at these wavelengths were converted to flux units using known scaling factors. For example, in the case of the images from *2MASS*, to convert from instrumental measurements to flux units, we used the factors given in the respective image headers. For *WISE*, we used the

[3] https://archive.stsci.edu/

factors available online. Similarly, for *MIPS*, we followed the procedure given in the *MIPS* instrument handbook [4].

We used the archival data from the adaptive optics assisted K-band observations acquired with the *Near-Infrared Integral Field Spectrometer (NIFS*; McGregor et al. 2003). The K-band centered at 2.2 μm covers a FoV of $3.4'' \times 3.4''$. The data cubes in the *NIFS* observations have a spatial sampling of $0.05''$/pixel. The spectral resolution is 45 km s^{-1} and the angular resolution is $0.2''$ (see Lemoine-Busserolle et al. 2019 and Brum et al. 2019 for details).

2.5 Millimetre

We used the archival data observed with the high-resolution *ALMA* with 12 m antennas in band 6. We reduced the data using the *Common Astronomy Software Application (CASA v5.4.1)* with the standard data reduction pipeline of the ALMA observatory. To generate the spectral data cubes, we used the task *TCLEAN*.

2.6 Radio

In the radio band, we used observations from the *VLA* carried out at 1.4 GHz in its C-configuration, at 4.8 GHz in B-configuration and at 15 GHz in A-configuration. The 4.8 GHz observations were reduced after flagging bad data sets, followed by phase and flux calibrations in *Astronomical Image Processing System (AIPS)*. We reduced the 15 GHz data using standard procedures that include flagging bad data using *CASA* (see Saikia et al. 2018 for details). We also used 21 cm HI emission line data from the *Westerbork Synthesis Radio Telescope (WSRT)* (see Heald & Oosterloo 2008 for more details).

[4] https://irsa.ipac.caltech.edu/data/SPITZER/docs/mips/mipsinstrumenthandbook/41/

3

What Fuels Warm Ionized Gas Outflows in Active Galactic Nuclei?

A viable feedback mechanism in AGN is outflows. These outflows are dynamic phenomena, representing the expulsion of vast amounts of matter and energy from the vicinity of SMBHs at the centres of galaxies. However, what drives these outflows is debated. They play a crucial role in shaping the surrounding environment and influencing the evolution of galaxies (Guo et al., 2023). They are multifaceted, seen in molecular, neutral and ionized gas (Nandi et al., 2023b; Riffel et al., 2023; Su et al., 2023; Izumi et al., 2023) and can occur on various scales, spanning from relatively small-scale winds to colossal jets extending over intergalactic distances (Harrison et al., 2014; Izumi et al., 2023; Guo et al., 2023). They can profoundly impact the galaxy's evolution by regulating the rate of star formation, distributing elements crucial for planetary systems, and even influencing the growth of SMBHs (Nandi et al., 2023a; Venturi et al., 2023). Irrespective of outflows being prevalent in AGN, questions such as (a) what drives these outflows and (b) at what scales they operate are not conclusively known

This Chapter is based on Nandi et al. (2025)

and are highly debated. The potential mechanisms that could drive these outflows could be radiation and/or radio jets (Wylezalek & Morganti, 2018).

Studies are available in the literature aimed at identifying the main driving mechanism for outflows. They are focused on individual systems as well as on a sample of sources. For example, jet-driven outflows have been suggested in NGC 1068 and IC 5063, where both radiation and jets may contribute, but jets dominate (García-Burillo et al., 2014; Venturi et al., 2021; Morganti et al., 2015). In contrast, radiation-driven outflows are evident in Mrk 231 (Feruglio et al., 2015). Some low-resolution statistical studies indicate that radio-luminous sources tend to have broader outflow features (Mullaney et al., 2013), while others suggest radiative outputs are the primary drivers (Zakamska & Greene, 2014). Compact radio sources, possibly hosting young jets, are more likely to drive outflows, with some studies finding correlations between outflow velocity and radio power (Liao et al., 2024). The debate persists regarding whether outflows are driven by accretion or radio activity.

3.1 Sample

Our initial sample of sources is derived from the MaNGA (Mapping Nearby Galaxies at Apache Point Observatory; Bundy et al. 2015) survey, a spectroscopic program under SDSS-IV. MaNGA employs a fiber-based integral field unit (IFU) spectroscopic technique, utilizing the two BOSS spectrographs mounted on the 2.5-meter Sloan Foundation Telescope at Apache Point Observatory. MaNGA has observed 10,010 unique galaxies with redshifts ranging from 0.01 to 0.15 (Wake et al., 2017), using different IFU configurations. The spatial resolution achieved is between $2''$ and $2.5''$, with a spectral resolution of approximately 2000. The program's field of view varies from $12''$ to $32''$, depending on the IFU configuration, covering a spatial range of 1.5 to 2.5 effective radii of the observed galaxies. We cross-correlated the sources in the MaNGA catalogue (Wake et al., 2017) with the latest version of the Million Quasars Catalogue (MILLIQUAS; Flesch 2023) to identify genuine AGN in the MaNGA catalogue, using a search radius of $2''$. MILLIQUAS is a collection of all published AGN and quasars till 30 June 2023, amounting to a total of 1,021,800 sources. Our cross-correlation of MaNGA sources with MILLIQUAS led to a sample of 1,142 AGN. As these sources were pulled from various surveys in MILLIQUAS, we checked the position of these 1142 sources in the Baldwin-Phillips-Terlevich diagram (BPT; Baldwin et al. 1981) for homogeneity. We took an aperture of 500×500 square pc box centred on the source and calculated the flux values of [OIII]λ5007, Hβ, Hα, [NII]λ6584, [SII]λ6718 and [SII]λ6732 lines from the Data Analysis Pipeline (DAP) products (Westfall et al., 2019) of MaNGA. Then, we plotted the flux ratio between [OIII]λ5007 and Hβ, [SII]λ(6717+6732) and Hα and also

the flux ratio between [OIII]λ5007 and Hβ, [NII]λ6584 and Hα in for the sources in the BPT diagrams. Then, Out of these 1142 sources, 718 are above the star-forming line in the [SII]λ(6717+6732)/Hα vs [OIII]λ5007/Hβ diagram and 740 sources lie above the star formation line in the [NII]λ6584/Hα vs [OIII]λ5007/Hβ diagram with 688 common sources in both the BPT diagrams. We considered these 688 AGN for our analysis out of which 252 are Seyferts, and 436 are LINERs.

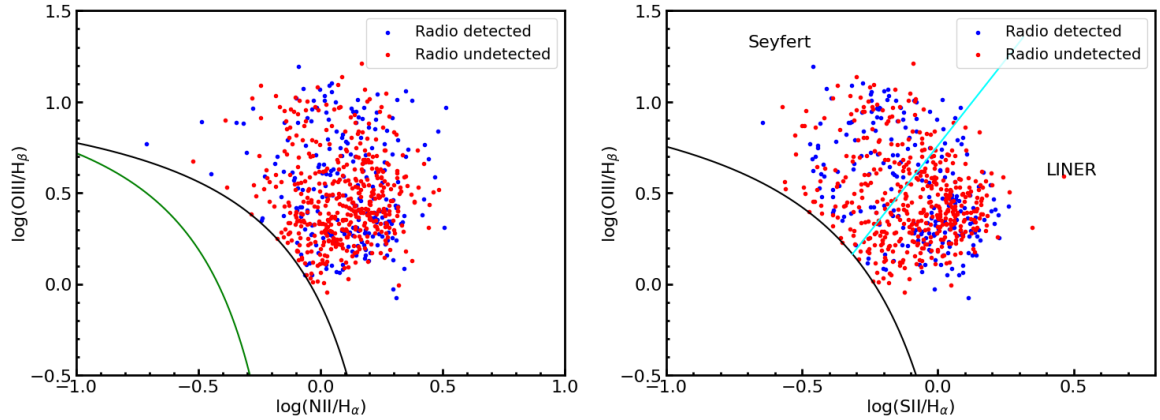

Fig. 3.1 Position of the sources in the [N II]/Hα BPT diagram (left) and [S II]/Hα BPT diagram (right). The black and green solid lines separate the region occupied by AGN and star-forming galaxies according to Kewley et al. (2001) and Kauffmann et al. (2003a), respectively. The cyan solid line separates Seyfert galaxies and LINERs (Kewley et al., 2001). Filled blue and red circles refer to radio-detected and radio-undetected sources.

We cross-matched these 688 AGN with the VLA Faint Images of the Radio Sky at Twenty-Centimeters (FIRST) survey (Becker et al., 1995) using an angular separation of 3″. The FIRST survey, conducted with the NRAO Very Large Array in its B-configuration, provides radio maps of the sky at 20 cm (1.4 GHz) with a beam size of approximately 5.4″, a typical root mean square (rms) noise level of 0.14 mJy beam^{-1}. Through this cross-matching process, we identified 217 AGN with radio counterparts in the FIRST catalogue, exhibiting flux densities greater than 0.5 mJy, classifying them as radio-detected. The remaining 471 AGN, lacking radio counterparts in the FIRST survey, were categorized as radio-undetected. Out of these 471 sources, 18 sources are not covered by the FIRST survey. Not considering those 18 sources, our final radio-undetected sample consists of 453 sources. Of the 217 radio-detected sample 95 sources are Seyfert type AGN while 122 are LINERs. Similarly, among the 453 radio-undetected sample, 149 sources are Seyfert type AGN while 304 sources are LINERs. The positions of these sources in the BPT diagrams are shown in Figure 3.1. Both the radio-detected and the radio-undetected samples have similar distributions in the redshift and optical B-band brightness plane (see Fig. 3.2). A Kolmogorov-Smirnov (KS) test carried out on

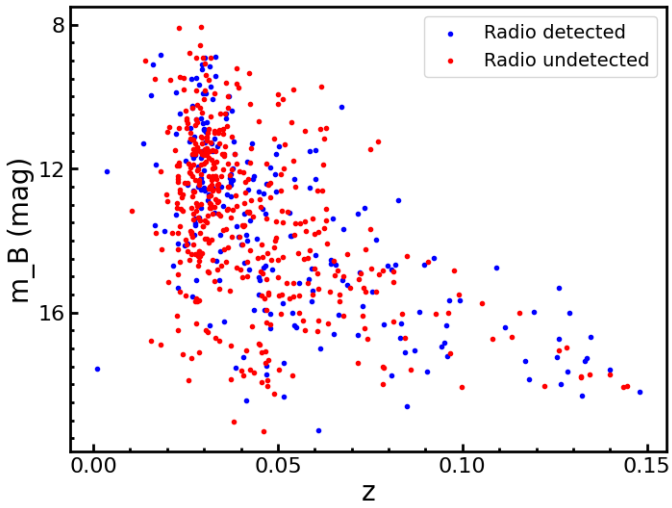

Fig. 3.2 Distribution of sources in the redshift versus B-band brightness plane. Here, the filled blue and red circles refer to the radio-detected and radio-undetected sources, respectively.

their distributions of redshift and B-band brightness indicates that the two samples are indeed indistinguishable with statistics of 0.07 and a p-value of 0.12.

3.2 Analysis

We focussed our analysis on a total of 217 AGN with radio detection and 453 AGN without radio detection in the FIRST survey. For this, we used the data reduction pipeline (DRP) products (Law et al., 2016) LOGCUBE of SDSS DR17. The DRP products contain the processed, and calibrated spectra for each spaxel in the field of view in form of cube for each source.

For each of the sources studied in this work, we generated summed spectra in the rest frame of the sources over a square with the length of the side of 500 pc. The choice of 500 pc is due to our requirement of having at least one spaxel to generate the spectra for most of the sources.

We fitted the [OIII]λ5007 profile with multiple Gaussian components along with a first order polynomial for the continuum using the nonlinear least square fitting algorithm within the `curvefit` module in the `Scipy` library. We fitted [OIII]λ5007 because we are only interested in the warm ionised phase of outflow that is traced by the forbidden bright line [OIII]λ5007. During the fit, we kept the width, peak and amplitude of each of the components as free parameters. Also, we restricted the fitting to those sources for which the signal-to-noise ratio (SNR) of the line is more than 3.0. Here, SNR refers to the ratio of the flux at the peak of the line to the standard deviation of continuum fluxes on either side of the line. We used a total of

80 Å width for the spectral region (4977−5057 Å) during the fitting. For some sources, the [OIII]λ5007 line profile was adequately modelled with a single Gaussian component. However, in cases where the residual, defined as (data - model)/data, exceeded 10%, additional Gaussian components were considered. The residual was reassessed after each addition and compared to the previous fit. If including an additional Gaussian reduced the residual and smoothed fluctuations in both the surrounding continuum and the line region, the extra component was adopted. Otherwise, the fit was restricted to the minimum number of Gaussian components required. For cases where more than one Gaussian component was necessary, an additional criterion was applied: the peak of the second and third components have to exceed three times the standard deviation of the continuum fluxes to confirm their statistical significance. In the radio-detected sample, the SNR of the first outflow component ranges from 10 to 306, while the SNR of the second outflow component ranges from 8 to 331. In the radio-undetected sample, the SNR of the first outflow component ranges from 4 to 199, and the SNR of the second outflow component ranges from 3 to 122. We show in Fig. 3.3, that spectral fits to three sources, one requiring a single Gaussian component, while the others requiring two and three Gaussian components, respectively. We also manually inspected each of the fitted spectra to ensure their fitting was correct.

After the fitting, we corrected the measured outflow fluxes for galactic extinction using Cardelli et al. (1989) and the E(B−V) values given in the header of DRP files. The fluxes were also corrected for internal extinction using the Hα and Hβ ratio taken from DAP products and following Miller & Mathews (1972); Veilleux et al. (1995) and Calzetti et al. (2000). Under the theoretical assumption of case B recombination, the intrinsic Hα/Hβ ratio was taken as 3.1 (Osterbrock & Ferland, 2006).

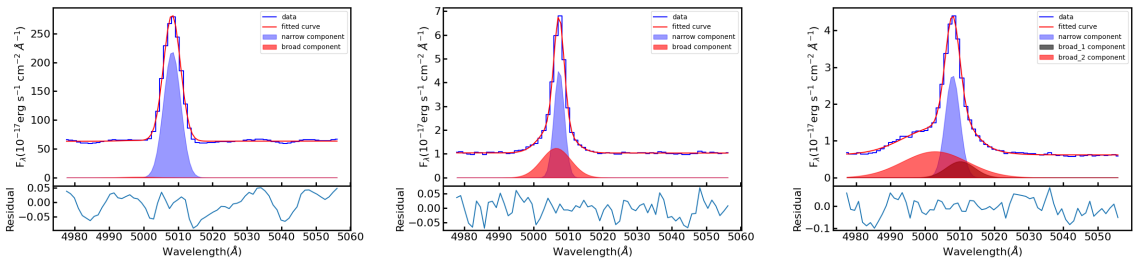

Fig. 3.3 Example line fits to the [O III]λ5007 line for an outflow undetected (left panel) and an outflow detected (middle and right panels) source. A single Gaussian profile nicely describes the observed line profile (left panel), while two and three Gaussian components (two phases of outflow) were required for the observed line profile in the middle and right panels. The broad Gaussian components in the middle and right panels showed the presence of outflow.

3.3 Results and Discussion

3.3.1 Detection of outflows

For both the radio-detected and the radio-undetected samples, we searched for the signature of outflows over a region of 500 × 500 square pc centered on each of the sources. The [OIII]λ5007 line was detected at the 3σ limit for 197 sources in the radio-detected category and 341 sources in the radio-undetected category. Our final sample thus consists of a total of 538 sources with strong [OIII]λ5007 for further analysis.

For the radio-detected sample, out of 197 sources, for 86 sources, a single Gaussian component proved sufficient for fitting the [OIII]λ5007 line, for 77 sources, two Gaussian components were needed to fit the line, while for 34 sources three Gaussian components were needed to model the line. Considering sources that require more than one Gaussian component to well represent the [OIII]λ5007 line, in the radio-detected category, a total of 111 out of 197 sources (56$\pm$7%), prominently showed discernible signatures indicative of outflows.

Similarly, in the radio-undetected sample, out of the 341 sources, 257 sources required a single Gaussian component to well represent the [OIII]λ5007 line, while 69 sources required two Gaussian components and 15 sources needed three Gaussian components to well model the line. Thus, in the radio-undetected sample, we detected outflows for 84 sources i.e. 25$\pm$3% of the sources showed signatures of outflows. This clearly indicates that the outflow detection rate is higher in the radio-detected sample compared to the radio-undetected sample.

We also classified our sample into Seyferts and LINERs based on their location in the BPT diagram to investigate their prevalence of outflows. In the radio-detected sample, we have 92 Seyferts and 105 LINERs for which [OIII]λ5007 was significantly detected. Of these, we detected outflows in 81 Seyferts and 30 LINERs. Similarly, in the radio-undetected sample, we detected [OIII]λ5007 line in 131 Seyferts and 210 LINERs. Of these, we detected outflows in 66 Seyferts and 18 LINERs. The results of the analysis are summarised in Table 3.1 and in Fig. 3.4.

Considering the total sample, we found that 66$\pm$7% of Seyferts show outflows, compared to only 15 $\pm$ 2% LINERs. In radio-detected Seyferts, outflows are detected in 88 $\pm$ 13% sources, while in radio-detected LINERs, it is 29$\pm$6%. In the case of the radio-undetected sample, we detected outflows for 50 $\pm$ 8% Seyferts and 8 $\pm$ 2% LINERs. Thus Seyferts consistently show more frequent outflows than LINERs, both in radio-detected and radio-undetected samples. This is in agreement with a recent study by Torres-Papaqui et al. (2024) who, too, from a systematic analysis of the SDSS spectra of a large sample of Seyferts and LINERs, found that the probability of detecting outflows in LINERs is lower compared to that of Seyferts.

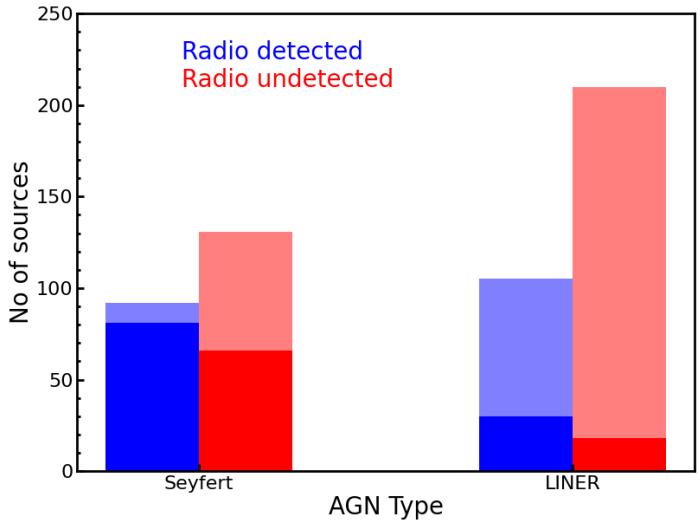

Fig. 3.4 Bar chart of the different types of AGN (Seyferts and LINERs) used in this study. Here, the large blue bar refers to the total radio-detected sources, and the large red bar refers to the total radio-undetected sources. Dark shaded regions refer to outflow detected sources.

	Total Sample		radio-detected			radio-undetected		
	Seyferts	LINERs	Total	Seyferts	LINERs	Total	Seyferts	LINERs
Total number of sources	223	315	197	92	105	341	131	210
Number of source with one Gaussian component	76	267	86	11	75	257	65	192
Number of sources with two Gaussian components	99	47	77	47	30	69	52	17
Number of sources with three Gaussian components	48	1	34	34	0	15	14	1
Number of sources with outflow	147	48	111	81	30	84	66	18
Outflow detection rate in percentage	66±7	15±2	56±7	88±13	29±6	25±3	50±8	8±2

Table 3.1 Summary of the sources analysed for ionised outflows in the [OIII]λ5007 line.

3.3.2 A comparison of the kinematics properties of the outflow

In the following sections, we compared the kinematic properties of outflow in our sample of sources. In cases where two outflowing components were detected, we initially consider only the brightest of the two in the analysis of the kinematic properties of the outflow. We later also considered the outflowing component of lower brightness, and also the one with the higher velocity. The values for the brighter component are tabulated in Table 3.2 for the total sample, the Seyferts and LINERs and among them separately into radio-detected and radio-undetected samples. Similar Tables for the other two cases are presented in Tables 3.3 and 3.4, respectively.

3.3.2.1 Velocity shift

We measured the velocity shift (V_{shift}) of the outflowing component relative to the narrow component of the [OIII]λ5007 emission line. In this definition, a negative value of V_{shift} corresponds to the broad blueshifted component and a positive value of V_{shift} corresponds to the broad redshifted component. The distribution of V_{shift} for both the radio-detected and radio-undetected sample of sources is shown in the upper left panel of Fig. 3.5. The KS test reveals that the distributions of the two samples are not statistically different, with a p-value of 0.4. For the radio-detected sample, V_{shift} ranges from -782 km s^{-1} to 463 km s^{-1}, with a mean of -178 km s^{-1} and a median of -163 km s^{-1} with median uncertainty of 46 km s^{-1}. Similarly for the radio-undetected sample, V_{shift} ranges from -628 km s^{-1} to 108 km s^{-1}, with a mean of -234 km s^{-1} and a median of -167 km s^{-1} with median uncertainty of 70 km s^{-1}. In both our samples, we found more sources ($\sim$ 80%) to show blue asymmetries of their [OIII]λ5007 line relative to red asymmetry. This could be because of the redshifted part of the bipolar outflow being obscured by dust and/or seen at a lower S/N than the blue-shifted component and thus undetected (Belli et al., 2024).

3.3.2.2 Velocity dispersion

We parameterise the emission line profile of the outflowing component using the dispersion of the line parameter ($\sigma_{measured}$) obtained from the fitting of the [OIII]λ5007 line. This measured velocity dispersion of the outflowing component, $\sigma^2_{measured} = \sigma^2_{out} + \sigma^2_{inst}$, where σ_{out} and σ_{inst} are the intrinsic velocity dispersion of the outflowing component and the dispersion of the instrumental line spread function. For MaNGA, the 1σ width of the instrumental line spread funciton is $\sim$70 km s^{-1} (Law et al., 2022). To estimate σ_{out}, we subtracted σ_{inst} from $\sigma_{measured}$ in quadrature. From the estimated σ_{out}, we calculated the full width at half maximum (FWHM) of the outflowing component as $FWHM_{out} = 2\sqrt{2ln2}\ \sigma_{out} = 2.35\sigma_{out}$, which is valid for a true

Gaussian profile. The distribution of $FWHM_{out}$ is shown in the upper middle panel of Fig. 3.5 for both the radio-detected and radio-undetected samples.

For the radio-detected category, FWHM$_{out}$ ranges from 169 km s^{-1} to 1398 km s^{-1}, with a mean value of 646 km s^{-1} and a median of 626 km s^{-1} with median uncertainty of 59 km s^{-1}. For the radio-undetected category, FWHM$_{out}$ ranges from 140 km s^{-1} to 1171 km s^{-1} and it is lower compared to radio-detected sample, with a mean of 526 km s^{-1} and a median of 518 km s^{-1} along with median uncertainty of 82 km s^{-1}. Therefore, this larger range and higher values of FWHM$_{out}$ for radio-detected sources indicate that the outflowing material in them is more kinematically disturbed compared to radio-undetected sources.

3.3.2.3 Outflow velocity

We define the outflow velocity, V_{out}, as the sum of the velocity difference ($|V_{shift}|$) between the outflowing component and the narrow component, plus two times the standard deviation of the outflowing component (σ_{out}), i.e., $V_{out} = |V_{shift}| + 2\sigma_{out}$ (Parlanti et al., 2024). The distribution of V_{out} is shown in the upper right panel of Fig. 3.5 for both the radio-detected and radio-undetected samples. The KS test indicates that the distributions of the radio-detected and radio-undetected populations are statistically distinct, with a p-value of 6×10^{-3}. This low p-value suggests that the likelihood of these two distributions being drawn from the same parent population is very low.

For the radio-detected sample, the outflow velocity V_{out} spans from 271 km s^{-1} to 1970 km s^{-1}, with an average velocity of 788 km s^{-1} and a median velocity of 705 km s^{-1} with median uncertainty of 74 km s^{-1}. In contrast, the radio-undetected sources exhibit a range of V_{out} from 118 km s^{-1} to 1387 km s^{-1}, with a lower mean velocity of 691 km s^{-1} and a median of 610 km s^{-1} along with median uncertainty of 98 km s^{-1}. The higher velocities in the radio-detected sample may imply that radio emission is linked to more powerful or sustained outflows, possibly associated with jet-driven mechanisms or enhanced AGN activity. The contrast in median and mean velocities between the two samples supports the idea of a significant difference in outflow dynamics related to the presence of radio emission.

3.3.2.4 Asymmetric index

To evaluate the asymmetry of the total [OIII]λ5007 line profile, we utilize the asymmetry index (AI). Following Zakamska & Greene (2014), the AI is defined as

$$AI = \frac{(V95 - V50) - (V50 - V05)}{V95 - V05} \tag{3.1}$$

Here V95, V50 and V05 are the velocities at which 95%, 50% and 5% of the emission line flux is found. A value of zero indicates a symmetric profile, a positive value suggests redshifted wings, and a negative value indicates blueshifted wings. The middle left panel of Fig. 3.5 displays the distribution of asymmetry index (AI) values for both the radio-detected and radio-undetected samples. Statistically, these distributions differ, with a KS test statistic of 0.32 and a p-value of 0.04, suggesting a significant but moderate distinction between the two groups.

For the radio-detected sample, AI values range from -0.46 to 0.12, with an average of -0.15 and a median of -0.16 with median uncertainty of 0.05. In contrast, the radio-undetected sample has a wider range from -0.51 to 0.16, with a mean value of -0.18 and a median of -0.17 with median uncertainty of 0.10. The consistently negative AI in both the samples suggests the dominance of the blueshifted component of the bipolar outflow relative to the redshifted component of the outflow, as discussed in section 3.3.2.1.

3.3.2.5 Outflow mass

We determined the mass of the outflowing gas (M_{out}) following Carniani et al. (2024) as

$$M_{out} = 0.8 \times 10^8 \left(\frac{L_{[OIII]out}}{10^{44} ergs^{-1}}\right) \left(\frac{500 cm^{-3}}{n_e}\right) \left(\frac{Z_\odot}{Z}\right) M_\odot \tag{3.2}$$

here, $L_{[OIII]out}$ is the luminosity of the outflowing component calculated from the flux of the outflowing component of [OIII]λ5007 and corrected for dust extinction following the procedure given in Section 3.2. The outflow mass also depends on both the electron density (n_e) and the gas phase metallicity of the medium. We calculated n_e using the ratio of [SII]λ6718 to [SII]λ6732, assuming an electron temperature of 10,000 K, using *pyneb* (Luridiana et al., 2015). We also determined the gas phase metallicity using [OIII]$\lambda\lambda$4959,5007, [NII]$\lambda\lambda$6548,6584, and the Balmer lines (Hα and Hβ), as described by do Nascimento et al. (2022).

The distribution of M_{out} for both the radio-detected and radio-undetected samples is illustrated in the middle panel of Fig. 3.5. A KS test shows that the two distributions are statistically distinct, with a p-value of 6×10^{-4}. For the radio-detected sample, M_{out} ranges from 181 $M_\odot$ to 2.4×10^6 $M_\odot$, with a mean of 1.1×10^5 $M_\odot$ and a median of 3.5×10^4 $M_\odot$ with median uncertainty of 1.4×10^3 $M_\odot$. In contrast, the radio-undetected sample, shows M_{out} values ranging from 30 $M_\odot$ to 1.5×10^5 $M_\odot$, with a mean of 2.5×10^4 $M_\odot$ and a median of 9.6×10^3 $M_\odot$ along with median uncertainty of 8.6×10^2 $M_\odot$. This finding suggests that outflow masses are notably higher in radio-detected sources than in radio-undetected sources.

3.3.2.6 Mass outflow rate

We calculated the mass outflow rate ($\dot{M}_{out}$), which represents the mass of gas outflowing per unit time as

$$\dot{M}_{out} = \frac{V_{out} M_{out}}{R} \tag{3.3}$$

We considered R as 500 pc. The distribution of $\dot{M}_{out}$ for both the radio-detected and radio-undetected samples is illustrated in the middle right panel of Fig. 3.5. According to the KS test, the distributions differ significantly, with a p-value of 5×10^{-5}.

For the radio-detected sample, $\dot{M}_{out}$ ranges from 2.3×10^{-4} to 5.1 $M_\odot$ yr^{-1}, with a mean of 0.17 $M_\odot$ yr^{-1} and a median of 0.04 $M_\odot$ yr^{-1} with median uncertainty of 0.004 $M_\odot$ yr^{-1}. For the radio-undetected sample, $\dot{M}_{out}$ ranges from 8.0×10^{-5} to 0.2 $M_\odot$ yr^{-1}, with a mean of 0.03 $M_\odot$ yr^{-1} and a median of 0.01 $M_\odot$ yr^{-1} with median uncertainty of 0.002 $M_\odot$ yr^{-1}. These results indicate that $\dot{M}_{out}$ is consistently higher in radio-detected sources compared to radio-undetected ones.

3.3.2.7 Power of outflows

The kinetic power of outflows (KP_{out}) is defined as

$$KP_{out} = \frac{1}{2} \dot{M}_{out} V_{out}^2 \tag{3.4}$$

The distribution of KP_{out} for our sample of sources is shown in the bottom left panel of Fig. 3.5. The figure shows that radio-detected sources exhibit more powerful outflows than radio-undetected sources. From KS test, we found that the distributions of KP_{out} for the radio-detected and radio-undetected samples are indeed different with a p-value of 2×10^{-7}.

For the radio-detected sample, KP_{out} ranges from 2.0×10^{37} to 1.8×10^{42} erg s^{-1}, with a mean of 4.6×10^{40} erg s^{-1} and a median of 4.8×10^{39} erg s^{-1} with median uncertainty of 1.8×10^{39} erg s^{-1}. In the radio-undetected sample, KP_{out} varies from 3.3×10^{37} to 7.0×10^{40} erg s^{-1}, with a mean of 4.2×10^{39} erg s^{-1} and a median of 1.3×10^{39} erg s^{-1} with median uncertainty of 5.9×10^{38} erg s^{-1}.

This indicates that radio-detected sources consistently exhibit higher outflow power compared to radio-undetected sources. This difference could suggest that radio emission is likely associated with more energetic outflows, possibly jets, potentially amplifying the AGN's feedback impact on the surrounding gas. Higher outflow power in radio-detected galaxies may be a sign of more efficient energy transfer from the AGN to the host galaxy's interstellar medium, possibly affecting star formation and the overall galactic environment (King & Pounds, 2015).

3.3.2.8 Momentum rate of outflows

The momentum rate of outflows ($\dot{P}_{out}$) is defined as $\dot{P}_{out} = \dot{M}_{out} V_{out}$. The distribution of $\dot{P}_{out}$ (outflow momentum rate) for the sample is shown in the bottom middle panel of Fig. 3.5. According to the KS test, $\dot{P}_{out}$ is significantly higher in radio-detected sources than in radio-undetected ones, with a p-value of 9×10^{-7}.

For radio-detected sources, $\dot{P}_{out}$ spans from 8.3×10^{29} to 3.4×10^{34} g cm s^{-2}, with a mean of 9.2×10^{32} g cm s^{-2} and a median of 1.7×10^{32} g cm s^{-2} with median uncertainty of 3.0×10^{31} g cm s^{-2}. For the radio-undetected sources, $\dot{P}_{out}$ ranges from 5.8×10^{29} to 1.2×10^{33} g cm s^{-2}, with a mean of 1.1×10^{32} g cm s^{-2} and a median of 5.1×10^{31} g cm s^{-2} and with median uncertainty of 1.5×10^{31} g cm s^{-2}. This indicates that $\dot{P}_{out}$ is nearly an order of magnitude higher in radio-detected sources compared to radio-undetected sources.

The elevated $\dot{P}_{out}$ in radio-detected sources suggests a stronger coupling between the AGN energy and the outflow momentum, enhancing feedback effects on the host galaxy. Given the higher outflow power (KP_{out}) and mass outflow rates ($\dot{M}_{out}$) in these sources, it appears that radio activity is correlated with more efficient AGN feedback. This combination of higher momentum, power, and mass flow may drive larger-scale gas movements, which could potentially lead to star formation suppression or triggering in the host galaxy more effectively than in radio-undetected sources (Fabian, 2012; King & Pounds, 2015; Tadhunter, 2016).

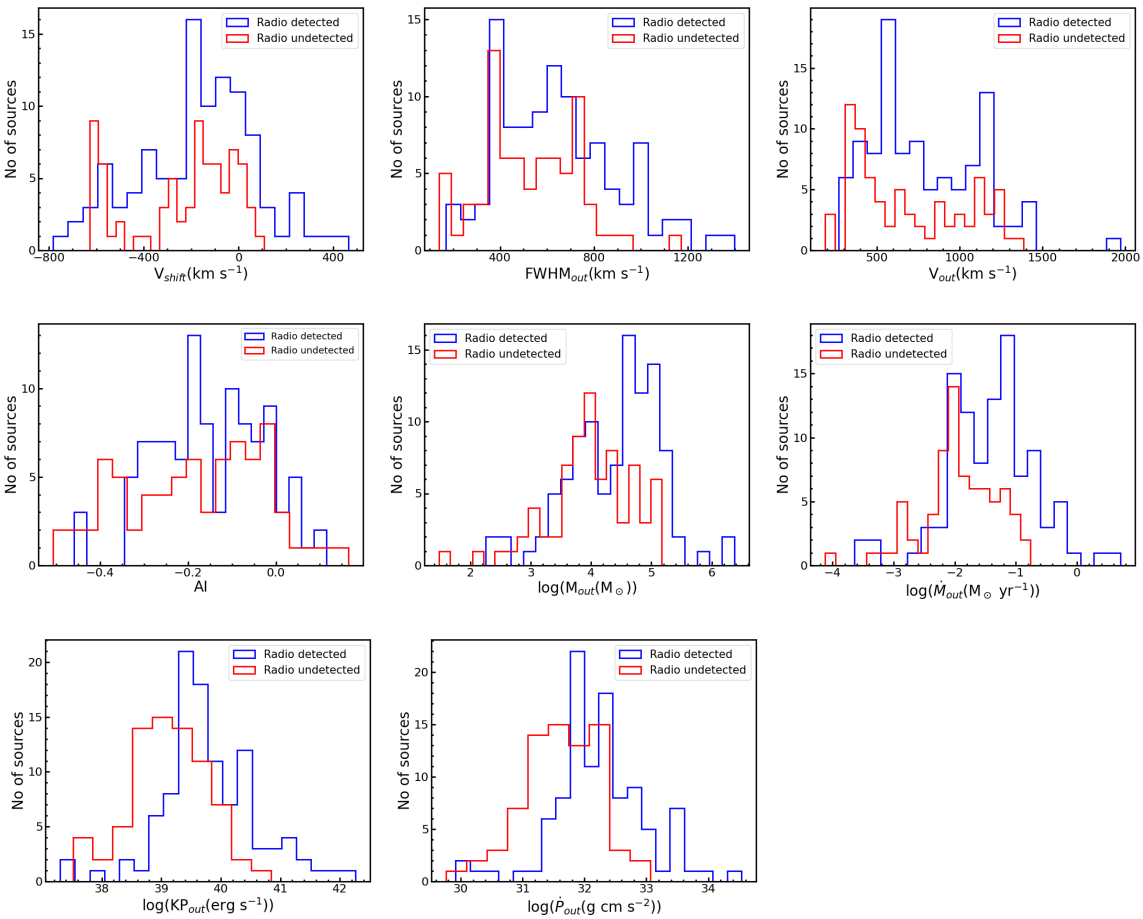

Fig. 3.5 Histograms of different kinematics properties of outflows. The parameters are labelled in the respective plots. The blue and red histograms are for the radio-detected and radio-undetected samples, respectively.

Parameter	Total			Seyferts			LINERs		
	Range	Mean	Median	Range	Mean	Median	Range	Mean	Median
V_{shift}(km s^{-1})	−782 to 463	−178	−163	−782 to 463	−106	−89	−695 to 258	−376	−449
FWHM$_{out}$(km s^{-1})	169 to 1398	646	626	169 to 1398	635	611	257 to 1018	678	737
V_{out}(km s^{-1})	271 to 1970	788	705	271 to 1970	720	642	378 to 1400	973	1084.0
AI	−0.46 to 0.12	−0.15	−0.16	−0.34 to 0.12	−0.14	−0.15	−0.46 to 0.11	−0.18	−0.16
M_{out}(10^2 M$_\odot$)	1.81 to 23681.85	1069.71	348.47	1.89 to 23681.85	1362.98	507.71	1.81 to 2120.98	273.70	41.16
$\dot{M}_{out}$(10^{-3} M$_\odot$ yr^{-1})	0.23 to 5112.32	166.56	43.28	0.23 to 5112.32	212.13	59.45	0.33 to 424.39	42.87	8.02
KP$_{out}$(10^{38} erg s^{-1})	0.20 to 18166.25	461.92	48.25	0.24 to 18166.25	591.12	55.63	0.20 to 1425.12	111.26	34.40
$\dot{P}_{out}$ (10^{30} g cm s^{-2})	0.83 to 34222.09	923.43	165.39	0.83 to 34222.09	1177.20	198.87	0.91 to 2761.69	234.64	60.19

(a) Radio-detected

Parameter	Total			Seyferts			LINERs		
	Range	Mean	Median	Range	Mean	Median	Range	Mean	Median
V_{shift}(km s^{-1})	−628 to 108	−234	−167	−628 to 108	−173	−134	−624 to −211	−526	−585
FWHM$_{out}$(km s^{-1})	140 to 1171	526	518	140 to 865	485	443	580 to 1171	720	672
V_{out}(km s^{-1})	118 to 1387	691	610	188 to 1274	598	487	849 to 1387	1137	1136
AI	−0.51 to 0.16	−0.18	−0.17	−0.51 to 0.16	−0.15	−0.13	−0.44 to −0.01	−0.33	−0.37
M_{out}(10^2 M$_\odot$)	0.30 to 1488.24	252.60	96.10	4.70 to 1488.25	288.80	114.74	0.30 to 616.59	79.95	33.35
$\dot{M}_{out}$(10^{-3} M$_\odot$ yr^{-1})	0.080 to 173.53	26.34	11.34	0.95 to 173.53	27.85	12.61	0.08 to 151.93	19.11	7.42
KP$_{out}$(10^{38} erg s^{-1})	0.33 to 696.00	42.20	12.92	0.33 to 296.34	33.46	12.88	0.36 to 696.00	83.90	22.41
$\dot{P}_{out}$ (10^{30} g cm s^{-2})	0.58 to 1154.74	106.05	50.95	1.99 to 793.52	98.54	49.45	0.58 to 1154.74	141.85	50.95

(b) Radio-undetected

Table 3.2 Kinematic properties of the brightest outflow

We have so far focused on the brightest outflowing component in this Section 3.3.2 when multiple components were detected. This approach may lead to an over representation of highly ionized outflows while potentially underestimating those with higher velocities but lower ionization. To assess this potential bias, we conducted two additional analyses: one considering the less luminous outflows and another focusing on the outflows with higher velocities. The results of these analyses are provided in Tables 3.3 and 3.4, respectively. Across all cases, we observe that radio-detected sources consistently exhibit higher velocities, mass outflow rates, outflow powers, and outflow momentum rates compared to their radio-undetected counterparts.

Parameter	Total			Seyferts			LINERs		
	Range	Mean	Median	Range	Mean	Median	Range	Mean	Median
V_{shift}(km s^{-1})	−695.0 to 882.0	−194.0	−198.0	−583.0 to 882.0	−127.0	−163.0	−695.0 to 258.0	−376.0	−449.0
FWHM$_{out}$(km s^{-1})	156.0 to 1401.0	653.0	635.0	156.0 to 1401.0	644.0	619.0	257.0 to 1018.0	678.0	737.0
V_{out}(km s^{-1})	308.0 to 1503.0	823.0	818.0	308.0 to 1503.0	768.0	733.0	378.0 to 1400.0	973.0	1084.0
AI	−0.46 to 0.12	−0.15	−0.16	−0.34 to 0.12	−0.14	−0.15	−0.46 to 0.11	−0.18	−0.16
M_{out}(10^2 M$_\odot$)	1.11 to 23558.28	775.31	235.03	1.11 to 23558.28	960.12	348.17	1.81 to 2120.98	273.7	41.16
$\dot{M}_{out}$(10^{-3} M$_\odot$ yr^{-1})	0.07 to 5112.32	145.64	33.95	0.07 to 5112.32	183.5	43.07	0.33 to 424.39	42.87	8.02
KP$_{out}$(10^{38} erg s^{-1})	0.02 to 18166.25	489.61	47.73	0.02 to 18166.25	629.0	62.1	0.2 to 697.58	124.27	57.6
$\dot{P}_{out}$ (10^{30} g cm s^{-2})	0.14 to 34222.09	922.0	134.0	0.14 to 34222.09	1175.24	181.62	0.91 to 2761.69	234.64	60.19

(a) Radio-detected

Parameter	Total			Seyferts			LINERs		
	Range	Mean	Median	Range	Mean	Median	Range	Mean	Median
V_{shift}(km s^{-1})	−657.0 to 227.0	−277.0	−235.0	−657.0 to 227.0	−225.0	-186.0	−624.0 to −211.0	−526.0	−585.0
FWHM$_{out}$(km s^{-1})	152.0 to 1171.0	560.0	577.0	152.0 to 1151.0	527.0	505.0	580.0 to 1171.0	720.0	672.0
V_{out}(km s^{-1})	237.0 to 1387.0	769.0	733.0	237.0 to 1343.0	692.0	643.0	849.0 to 1387.0	1137.0	1136.0
AI	−0.51 to 0.16	−0.18	−0.17	−0.51 to 0.16	−0.15	−0.13	−0.44 to −0.01	−0.33	−0.37
M_{out}(10^2 M$_\odot$)	0.3 to 1481.81	202.86	78.37	4.7 to 1481.81	228.63	91.57	0.3 to 616.59	79.95	33.35
$\dot{M}_{out}$(10^{-3} M$_\odot$ yr^{-1})	0.08 to 247.09	24.88	9.87	1.08 to 247.09	26.1	11.58	0.08 to 151.93	19.11	7.42
KP$_{out}$(10^{38} erg s^{-1})	0.36 to 1053.8	59.27	14.97	0.46 to 1053.8	54.11	14.42	0.36 to 696.0	83.9	22.41
$\dot{P}_{out}$ (10^{30} g cm s^{-2})	0.58 to 1812.07	123.71	52.05	2.63 to 1812.07	119.91	55.32	0.58 1154.74	141.85	50.95

(b) Radio-undetected

Table 3.3 Kinematic properties of the low luminous outflow

3.3.3 Outflows in Seyferts vs LINERs

From Tables 3.2, 3.3 and 3.4 it is evident that the $FWHM_{out}$ and V_{out} are significantly greater in LINERs relative to Seyferts, suggesting higher outflow velocities in them. Additionally, a comparison of V_{shift} reveals that the outflows are more blueshifted in LINERs than Seyferts. This larger velocity structure in LINERs may be linked to shock-dominated emission, as suggested by Dopita & Sutherland (1995). However, when considering the mass outflow rate, outflow power and outflow momentum rate, Seyferts exhibit notably higher values, along with a greater outflow detection rate, as discussed in Section 3.3.1. This contrast is likely due to LINERs being at the low luminosity end of AGN, with ionizing power and accretion rate lower than that of Seyferts (Heckman, 1980; Ho, 2008; Márquez et al., 2017), producing less outflowing material, thereby resulting in lower detection rates and less powerful outflows.

3.3.4 Infrared properties of outflows

Of the sources analysed in this work, more than half of them are found to show outflows as evidenced by the presence of shifted broad asymmetric wings in their [OIII]λ5007 line. Such observed line profile could be the result of gas outflows from the central region of these sources (Zamanov et al., 2002). Such outflows can also be from the inner narrow line region (NLR) related to the winds from AGN (Elvis, 2000). Alternatively, outflows can also be driven by star formation processes via winds from massive stars and/or Type 2 supernova explosions (Parlanti et al., 2024). Studies available in the literature point to infrared observations being an effective tool to distinguish between these two processes, namely AGN driven and star formation driven outflows. Therefore, to investigate the infrared properties of the sources with outflows, we cross-correlated our sources with the *Wide-field Infrared Survey Explorer* (WISE;Wright et al. 2010) catalog[1] using a search radius of 3 arcsec for both our samples. To ensure reliable data for analysis, we only included sources with a signal-to-noise ratio (SNR) greater than 3.0 in the W3 band. Since the WISE catalogue provides magnitudes in the Vega system by default, we converted them to the AB magnitude system following the guidelines provided at https://wise2.ipac.caltech.edu/docs/release/allsky/expsup/sec4_4h.html.

We generated a colour-colour diagram using W2−W3 and W1−W2 in the AB system for both the radio-detected and radio-undetected samples, and this is depicted in the left and middle panels of Fig. 3.6. Sources in this plot are classified into star formation and AGN, with a division at W2−W3 =0.8 According to this division (Sabater et al., 2019), sources to the left are AGN dominated, and sources to the right are star formation dominated. Thus, in our radio-detected and radio-undetected sample, a large fraction of sources with outflows lie in

[1] https://irsa.ipac.caltech.edu/Missions/wise.html

Parameter	Total			Seyferts			LINERs		
	Range	Mean	Median	Range	Mean	Median	Range	Mean	Median
V_{shift}(km s^{-1})	−782.0 to 882.0	−198.0	−193.0	−782.0 to 882.0	−133.0	−133.0	−695.0 to 258.0	−376.0	−449.0
FWHM$_{out}$(km s^{-1})	176.0 to 1401.0	728.0	682.0	176.0 to 1401.0	731.0	679.0	257.0 to 1018.0	678.0	737.0
V_{out}(km s^{-1})	337.0 to 1970.0	879.0	864.0	337.0 to 1970.0	844.0	826.0	378.0 to 1400.0	973.0	1084.0
AI	−0.46 to 0.12	−0.15	−0.16	−0.34 to 0.12	−0.14	−0.15	−0.46 to 0.11	−0.18	−0.16
$M_{out}(10^2$ M$_\odot$)	1.81 to 23558.28	831.92	239.35	1.89 to 23558.28	1037.58	384.92	1.81 to 2120.98	273.7	41.16
$\dot{M}_{out}(10^{-3}$ M$_\odot$ yr^{-1})	0.23 to 5112.32	163.81	42.14	0.23 to 5112.32	208.36	56.62	0.33 to 424.39	42.87	8.02
KP$_{out}(10^{38}$ erg s^{-1})	0.2 to 18166.25	602.86	62.1	0.24 to 18166.25	783.98	101.5	0.2 to 1425.12	111.26	34.4
$\dot{P}_{out}$ (10^{30} g cm s^{-2})	0.83 to 34222.09	1079.06	180.65	0.83 to 34222.09	1390.16	267.04	0.91 to 2761.69	234.64	60.19

(a) Radio-detected

Parameter	Total			Seyferts			LINERs		
	Range	Mean	Median	Range	Mean	Median	Range	Mean	Median
V_{shift}(km s^{-1})	−657.0 to 177.0	−278.0	−235.0	−657.0 to 177.0	−225.0	−185.0	−624.0 to −211.0	−526.0	−585.0
FWHM$_{out}$(km s^{-1})	172.0 to 1171.0	575.0	580.0	172.0 to 1151.0	545.0	536.0	580.0 to 1171.0	720.0	672.0
V_{out}(km s^{-1})	312.0 to 1387.0	777.0	733.0	312.0 to 1343.0	701.0	657.0	849.0 to 1387.0	1137.0	1136.0
AI	−0.51 to 0.16	−0.18	−0.17	−0.51 to 0.16	−0.15	−0.13	−0.44 to −0.01	−0.33	−0.37
$M_{out}(10^2$ M$_\odot$)	0.3 to 1488.25	207.14	84.41	4.7 to 1488.25	233.8	94.93	0.3 to 616.59	79.95	33.35
$\dot{M}_{out}(10^{-3}$ M$_\odot$ yr^{-1})	0.08 to 247.09	26.72	9.97	1.08 to 247.09	28.32	11.58	0.08 to 151.93	19.11	7.42
KP$_{out}(10^{38}$ erg s^{-1})	0.36 to 1053.8	63.07	14.99	0.46 to 1053.8	58.71	14.98	0.36 to 696.0	83.9	22.41
$\dot{P}_{out}$ (10^{30} g cm s^{-2})	0.58 to 1812.07	133.73	52.05	2.63 to 1812.07	132.02	55.32	0.58 to 1154.74	141.85	50.95

(b) Radio-undetected

Table 3.4 Kinematic properties of the high speed outflow

the region occupied by star-forming galaxies. Recently, Salem et al. (2024) found that sources with $W2-W3<0.16$ in the AB system have very low specific star formation rate (sSFR) of $10^{-11.5}$ yr^{-1}.

We also investigated the W3−W4 colour, of our sample of sources with detected outflows, the distribution of which is shown in the right panel of Fig. 3.6 in the Vega system. Here, too, sources with W3−W4 <2.5 are AGN dominated, while sources with W3−W4 >2.5 are star formation dominated (Caccianiga et al., 2015). The infrared colour-colour diagram and the W3−W4 colour indicate that a significant fraction of sources with detected outflows falls within the region typically associated with star-forming galaxies, despite all our sources being classified as AGN based on the BPT diagram. This suggests that infrared colour is not a reliable metric for distinguishing between AGN-dominated and star-formation dominated sources.

Our analysis indicates that sources exhibiting outflows tend to have redder infrared (IR) colours, as illustrated in Fig. 3.6. We also examined the IR colours W1−W2 and W3−W4 in relation to the luminosity of the outflowing component and found a positive correlation in both cases. Interestingly, the correlation is stronger for the W3−W4 colour compared to W1−W2. This pattern is consistent across both the radio-detected and radio-undetected samples. These correlations suggest that dust in the vicinity of the outflows is likely the dominant contributor to the observed mid-infrared (MIR) emission.

Furthermore, the AGN in our sample, classified based on their BPT diagnostics, display increased redness in outflowing sources, which can be attributed to polar dust scattering. Dust grains absorb ultraviolet (UV) and optical radiation, re-emitting it in the IR and thus producing the observed redder colors. This process not only affects the IR emission but also alters the ionization conditions of the surrounding gas, potentially influencing the chemical composition of the outflows and aiding the formation of various molecules (Järvelä et al., 2022).

Our results are in agreement with Zhang et al. (2013) who found that the MIR covering factor (the ratio of MIR luminosity to bolometric luminosity) correlates with the outflow component of [OIII]λ5007, with the correlation strengthening at longer wavelengths. This was interpreted as evidence for IR emission produced by dust embedded within the outflows. Observations of several Seyfert galaxies also reveal that a significant fraction of their MIR emission originates along their polar directions, extending from a few parsecs to several hundred parsecs from the central engine. This emission is likely due to dust in the narrow-line region and/or dust driven by outflows (Hönig et al., 2013; Stalevski et al., 2019; Haidar et al., 2024).

3.3.5 Contribution of star formation to the outflows

In the previous section, it was observed that the infrared properties of outflows reveal a redder colour similar to that of star-forming galaxies. This raises the need to assess the contribution of

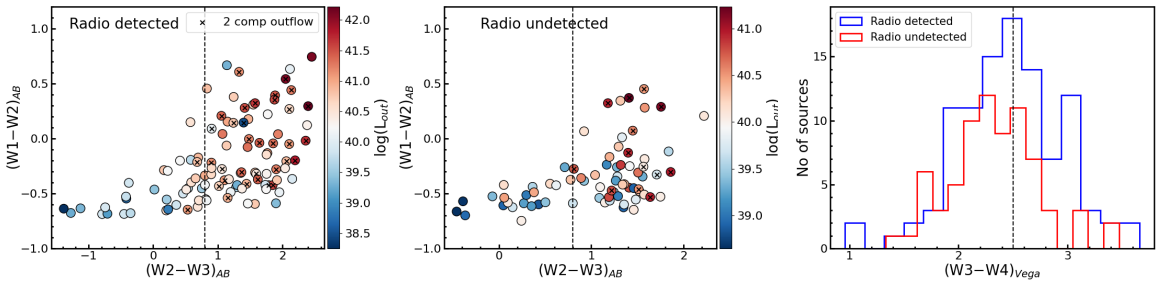

Fig. 3.6 Infrared colour-colour diagram for the sources with outflows in the radio-detected sample (left panel) and radio-undetected sample (middle panel). Black crosses refer to sources with two outflow components. The colour bar on the right indicates the total luminosity of the outflowing gas, and the vertical dashed line is the dividing line between AGN (left) and star-forming (right) according to Sabater et al. (2019). The right panel shows the distribution of W3−W4 colour. Here too, the vertical line at W3−W4 in 2.5 is the dividing line between AGN (left of the line) and star-forming (right of the line) sources (Caccianiga et al., 2015).

star formation to the outflows in our sample of sources, where outflows were detected. Though the sources are classified as AGN according to the BPT diagrams, the influence of nuclear star formation could still be present in them. We aimed to assess the role of star formation in influencing outflows in the central 500 × 500 square pc region, which necessitates investigation of the star formation characteristics. Numerous well-established tracers of star formation exist, such as strong emission lines in optical and infrared bands, as well as continuum emission from ultraviolet to radio wavelengths (Kennicutt & Evans, 2012). However, these tracers are often contaminated by AGN emission. Recently, Spindler et al. (2018) demonstrated that the sSFR derived from the Balmer 4000 Å break strength (D_n4000) is less impacted by AGN emission lines and thus can be a better diagnostic to constrain star formation (Wilkins et al., 2024). Consequently, we employed this method to examine the sSFR in our sample of sources.

We calculated D_n4000 by taking the ratio of the average of the flux density measurements in the blue spectral range (3525−3625 Å) to the average of the flux density measurements in the red spectral range (4150−4250 Å). This is defined as

$$D_n4000 = \frac{\int_{4150}^{4250} f_\lambda d\lambda \,/\, \int_{4150}^{4250} d\lambda}{\int_{3525}^{3625} f_\lambda d\lambda \,/\, \int_{3525}^{3625} d\lambda} \tag{3.5}$$

The chosen spectral window is slightly different from the one originally defined by Bruzual A. (1983), however, captures the break cleanly and does not cover the metal absorption lines (see also Wilkins et al. 2024 for the use of alternate wavelength windows). This wavelength window covers both the Balmer limit of 3645 Å which is sensitive to young galaxies and

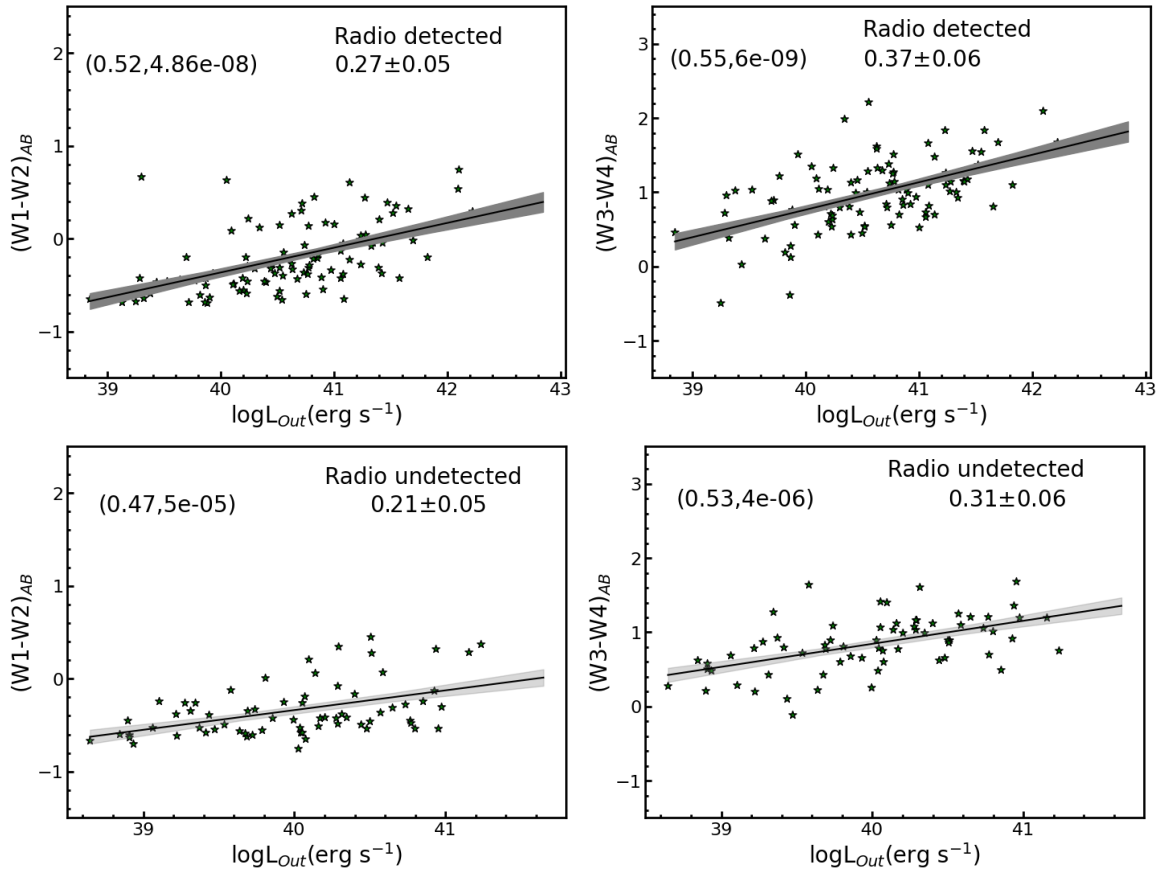

Fig. 3.7 Variation of infrared colours with outflow luminosity for radio-detected sample (upper panel) and for radio-undetected sample (lower panel). The correlation coefficient and p-value from the KS test are displayed in the upper-left corner of each plot, while the slope is indicated in the upper-right corner.

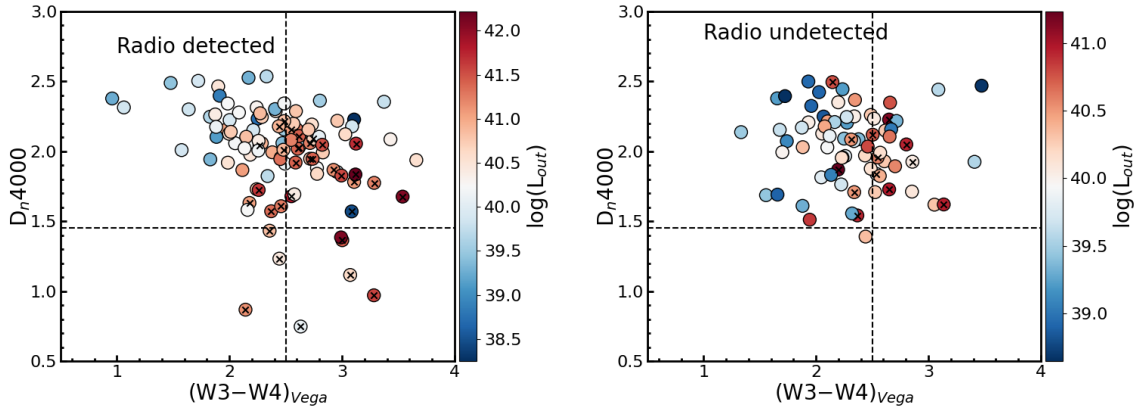

Fig. 3.8 Position of the sources with outflows in W3−W4 vs D_n4000 plane for radio-detected (left panel) and radio-undetected (right panel) samples. The colour denotes the total luminosity of outflows. The black crosses are sources with two outflowing components. The vertical dashed line is $(W3-W4)_{Vega} = 2.5$, the separation line between pure star-forming sources and AGN. The horizontal line is for $D_n4000 = 1.45$.

the 4000 Å break. The lower bound of the blue region for the break is determined by taking into account the instrument's shortest wavelength coverage that corresponds to the redshifted wavelengths of all observed sources.

The value of D_n4000 parameter for our sample of radio-detected and radio-undetected sources ranges from 0.8 to 2.8. D_n4000 is close to unity for the galaxies dominated by O and B-type stars (Wilkins et al., 2024), whereas D_n4000 higher than 1.51 is for an old stellar population with age more than 1.1 Gyr (Paulino-Afonso et al., 2020).

A recent study by Bluck et al. (2020) on MaNGA sources found that regions of galaxies with D_n4000 larger than 1.45 are quenched with very low star formation, though the exact values of sSFR are not known but are less than $10^{-11.5} yr^{-1}$. About 94% of the sources in the radio-detected sample and 99% of sources in the radio-undetected sample have D_n4000 larger than 1.45, which suggests substantially low or no star formation in this central region in our sample of sources. This may possibly be due to the negative feedback effect from AGN activity.

3.3.6 Origin of outflows: AGN v/s star formation

In Sections 3.3.4, we observed that infrared diagnostics alone are insufficient to distinguish whether strong outflows originate from AGN activity or purely from star formation. However, in Section 3.3.5, using optical diagnostics such as the Balmer break, we found that in sources with outflows, the star formation is very low or negligible. By combining these two diagnostic methods and analyzing the position of the sources with outflows in the D_n4000 v/s W3−W4

plane, it would be possible to identify if the detected outflows are due to star formation and/or AGN activity. We show in Fig. 3.8 the infrared colour versus the Balmer break plot. From this figure, it is evident that most of our sources are situated in the AGN-dominated region. This new diagnostic diagram clearly indicates that the outflows found in sources with and without radio emission are due to processes related to AGN. About 5% of the radio-detected sources with outflows lie in the region occupied by star formation with redder colours. In all these sources, both blueshifted (approaching component of outflows) and red-shifted (receding component of outflows) were detected. The redshifted component of the outflow, being located below the plane of the galaxy, is likely to be obscured by dust, and the observations of such sources to be redder in colour is not unexpected (Belli et al., 2024). Irrespective of that, the contribution from both AGN and star formation to the observed outflows in these minority of sources could not be ruled out. Also, a large fraction of sources with $D_n4000 > 1.45$ (thus negligible star formation) have redder colours, and this is likely due to the interaction of the outflowing gas with dust (Järvelä et al., 2022).

3.3.7 Cause of radio emission

From Section 3.3.6, it is clear that the observed outflows are due to AGN in both the samples of radio-detected and radio-undetected sources. Therefore, the observed radio emission in our radio-detected sample is unlikely to be due to star formation activities in their host galaxies, however, attributed to processes related to AGN such as the presence of low power radio jets, accretion disk corona as well as shocks due to outflows (Panessa et al., 2019; Liao et al., 2024). In this section, we aim to understand the origin of radio emission in our radio-detected sample making use of diagnostic plots available in the literature. We show in Fig. 3.9 the location of sources with outflows in the radio-detected sample in the F_{W3} v/s $F_{1.4}$ GHz plane. For this plot, the radio flux density values were taken from the FIRST survey, while the flux density corresponding to the W3 band of WISE was taken from the WISE catalogue. Also shown in the same plot is the $F_{W3} = F_{1.4}$ line. According to Kozieł-Wierzbowska et al. (2021) sources below the line are radio AGN, while those above the line are star burst dominated AGN. We also checked the q22 parameter defined as

$$q22 = log\,(F_{22}/F_{1.4}) \tag{3.6}$$

Here, F_{22} and $F_{1.4}$ are the flux densities in the W4 band of the WISE and 1.4 GHz from FIRST respectively. The histogram of the q22 parameter is shown in Fig. 3.10. Here, too, about 40% of the sources have q22 greater than unity, favouring star formation processes to be the cause of radio emission in them. In summary, although the q22 parameter and the F_{W3} v/s F1.4

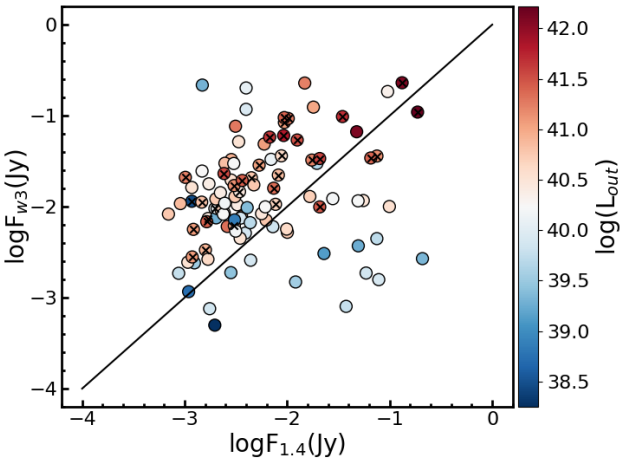

Fig. 3.9 Location of the sources with outflows in the radio-detected sample in the F(W3) v/s F(1.4GHz) plane. The solid black solid line is the $F_{W3} = F_{1.4}$ line. The black crosses are sources with two components of outflows. The colour denotes the luminosity of outflows.

diagnostics indicate that in a large fraction of the sources, the observed radio emission is likely to be associated with star formation activity, the plot of D_n4000 against q22 (Fig. 3.10) shows that all sources barring six sources, lie in the AGN dominated region. This reddening could be due to dust scattering of AGN radiation. This reinforces that the observed radio emission in our radio-detected sample is indeed AGN dominated. High resolution radio observations are the only direct way to identify which among the processes related to AGN are the cause of the observed radio emission in our sample. Though the detection of core jet structure is an unambiguous evidence of jet that produces the observed radio emission, the resolution of FIRST images used in this work is insufficient. In the absence of this, in all further discussion, we assume that the observed radio emission is due to jet emission.

3.3.8 Correlation of outflow properties with physical properties of AGN

From various diagnostics, it is clear that the detected outflows are due to AGN. In this scenario, the driving force of outflows could be either from the radiation energy or the radio jets from AGN. To explore this, we analyzed the outflow properties alongside AGN properties such as the M_{BH}, bolometric luminosity (L_{Bol})and Eddington ratio (λ_{Edd}) for both the radio-detected and radio-undetected samples as well as the radio jet power (P_{Jet}) for the radio-detected sample. We determined M_{BH} adopting the dynamical method, using the $M_{BH} - \sigma_\star$ relation, where $\sigma_\star$ represents the stellar velocity dispersion. The $\sigma_\star$ values were obtained from the *Pipe3d* catalogue (Sánchez et al., 2022), derived through stellar synthesis population modelling within

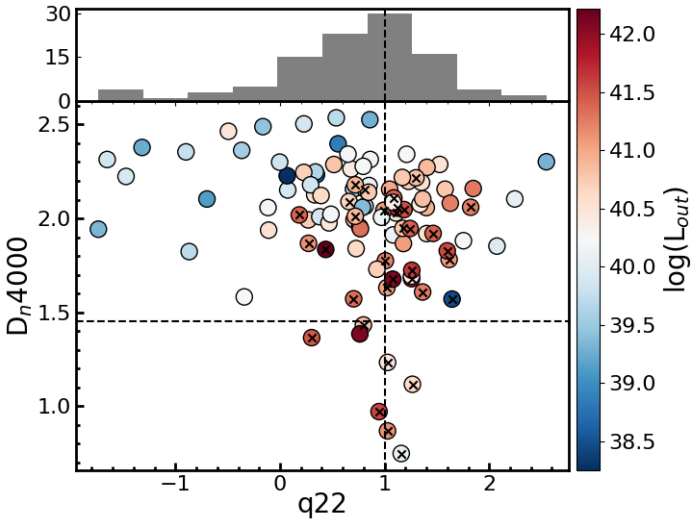

Fig. 3.10 Position of outflow detected sources in the radio-detected sample in q22 vs D_n4000 plane. The vertical line is $q22 = 1.0$, and the horizontal dashed line is $D_n4000 = 1.45$.

one effective radius. Following the relation provided in Baron & Ménard (2019), which has been validated for both Type 1 and Type 2 AGN, by Baron & Ménard (2019), we calculated M_{BH} for all the sources in our sample as

$$\log(M_{BH}/M_{\odot}) = (3.94 \pm 0.12)\log(\sigma_{\star}/200\,\mathrm{km\ s^{-1}}) + (8.13 \pm 0.07) \tag{3.7}$$

We calculated L_{Bol} as (Greene & Ho, 2007; Greene & Ho, 2005)

$$L_{Bol} = 2.34 \times 10^{44} (L_{H\alpha}/10^{42})^{0.86} erg\,s^{-1} \tag{3.8}$$

Here, the luminosity of the Hα line was determined from the Hα flux taken from DAP and corrected for extinction effects as described in Section 5.2.

We calculated λ_{Edd}, from Eddington luminosity L_{Edd}, the maximum luminosity emitted if the source is in hydrodynamical equilibrium and L_{Bol}, as the ratio of L_{Bol} to L_{Edd}. The L_{Edd} defined as

$$L_{Edd} = 1.26 \times 10^{38} \left(\frac{M_{BH}}{M_{\odot}}\right) erg\,s^{-1} \tag{3.9}$$

For the sample of radio-detected sources, we estimated P_{Jet} considering that the radio emission in these sources is jet emission. For this, we used the 1.4 GHz luminosity ($L_{1.4}$) calculated using the integrated flux densities from FIRST survey and corrected for redshift effect assuming a spectral index ($S_{\nu} \propto \nu^{-\alpha}$) of 0.7 (Condon et al., 2002). The distribution of

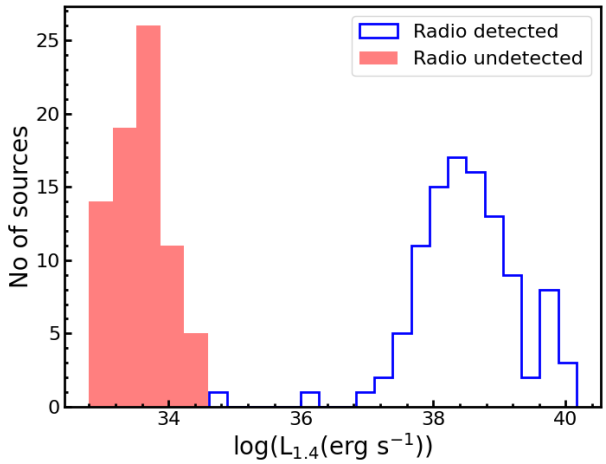

Fig. 3.11 Distribution of $L_{1.4}$ for the radio detetected sample (blue color). The shaded red region shows the upper limit of $L_{1.4}$ for the radio-undetected by considering the detection limit of the FIRST survey, which is 0.5 mJy.

$L_{1.4}$ for our sample of radio-detected and radio-undetected sources is shown in Fig. 3.11. For radio-undetected sources, the $L_{1.4}$ values are the upper limits that were calculated using the detection limit of the FIRST survey, which is 0.5 mJy.

We calculated P_{Jet} as Cavagnolo et al. (2010)

$$P_{Jet} = 5.8 \times 10^{43} \left(\frac{L_{1.4}}{10^{40} ergs^{-1}} \right)^{0.7} erg\, s^{-1} \tag{3.10}$$

After calculating these physical parameters of AGN, we compared them with outflow properties to explore potential correlations. In cases where two outflowing components were detected, for the total outflow rate or the total kinetic power of outflows, we used the sum of the quantities deduced from both components. We performed a statistical linear correlation test, the Pearson test, to identify significant correlations in terms of correlation coefficients and p-values. For parameters exhibiting significant correlations, we employed the Bayesian linear regression method using the *LINMIX_ERR* (**?**) to fit a power-law relationship between the variables in log-log space. This method takes account of errors in both axes. If the AGN parameter is X_{AGN} and outflow parameter is Y_{out} then the fitted function has the form

$$Y_{out} = A(X_{AGN})^{\alpha} \tag{3.11}$$

or

$$log(Y_{out}) = logA + \alpha log(X_{AGN}) \tag{3.12}$$

Parameter	Radio-detected		Radio-undetected	
Y_{out} v/s X_{AGN}	(R,p)	α	(R,p)	α
KP_{out} v/s L_{Bol}	$(0.72, 7\times10^{-18})$	1.18 ± 0.14	$(0.52, 2\times10^{-6})$	0.81 ± 0.20
$\dot{M}_{out}$ v/s L_{Bol}	$(0.74, 3\times10^{-19})$	1.07 ± 0.12	$(0.60, 9\times10^{-9})$	0.97 ± 0.17
KP_{out} v/s P_{Jet}	$(0.36, 2\times10^{-4})$	0.56 ± 0.14	–	–
$\dot{M}_{out}$ v/s P_{Jet}	(0.28, 0.004)	0.43 ± 0.12	–	–
KP_{out} v/s P_{Jet} [$\log(\frac{L_{Bol}}{P_{Jet}})> 0.4$]	$(0.64, 1\times10^{-11})$	0.99 ± 0.14	–	–
$\dot{M}_{out}$ v/s P_{Jet} [$\log(\frac{L_{Bol}}{P_{Jet}})> 0.4$]	$(0.58, 5\times10^{-9})$	0.79 ± 0.12	–	–

Table 3.5 Results of the fits to the observed data. Here, R and p are the correlation coefficient and probability for no correlation, respectively for the Pearson correlation test. The quoted values of α, the power law exponent are the mean and the 1σ standard deviation.

where A is the multiplication constant and α is the power-law exponent. The best-fit values for α and the correlation coefficients for different parameters are summarized in Table 3.5.

From Table 3.5, it is evident that both $\dot{M}_{out}$ and KP_{out} are significantly correlated with L_{Bol} for both radio-detected and radio-undetected sources. This finding aligns with previous studies in the literature (Fiore et al., 2017; Bischetti et al., 2019; Musiimenta et al., 2023). While our results confirm the correlation between $\dot{M}_{out}$ and L_{Bol} noted in earlier works, we also emphasize the differences in the correlations between the two samples. Notably, the higher correlation coefficient and lower p-values for radio-detected sources suggest that this correlation is stronger in radio-detected sources than in their radio-undetected counterparts.

Examining the relationship of these outflow parameters with AGN luminosity, we find that for the radio-detected sample, we observe $\dot{M}_{out} \propto L_{Bol}^{1.07\pm0.12}$. In contrast, for the radio-undetected sample, $\dot{M}_{out} \propto L_{Bol}^{0.97\pm0.17}$. Though the slopes are consistent within 1σ, KP_{out} demonstrates a more pronounced difference: we find $KP_{out} \propto L_{Bol}^{1.18\pm0.14}$ for radio-detected sources, while for the radio-undetected sample, we found $KP_{out} \propto L_{Bol}^{0.81\pm0.20}$. This indicates a steeper slope by 1σ for the radio-detected sources compared to their undetected counterparts. This trend is illustrated in Fig. 3.12, where we plot L_{Bol} against KP_{out} and $\dot{M}_{out}$, color-coded by λ_{Edd}. In the radio-detected category of sources, those with larger λ_{Edd} preferentially occupy the region with larger KP_{out}. This suggests a relationship between outflow power and λ_{Edd} for these sources. Conversely, this trend is not as clear for radio-undetected sources, as depicted on the right side of Fig. 3.12.

The correlations observed in Fig. 3.12, suggest multiple mechanisms are at play in driving outflows for radio-detected sources. While radiation from AGN is likely the primary driver of outflows in both radio-detected and radio-undetected sources, radio jets may serve as an

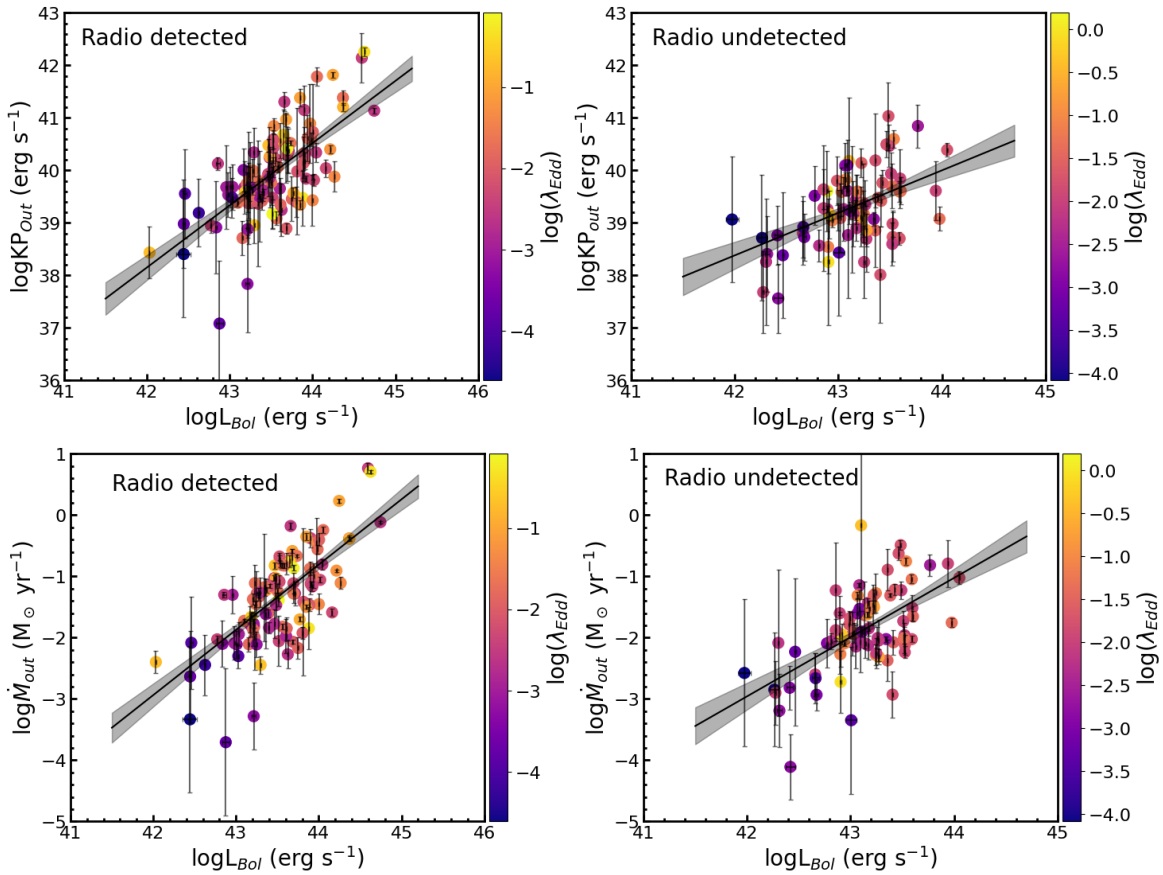

Fig. 3.12 Upper panel: Variation of total kinetic power of warm ionized outflow with L_{Bol} for radio−detected (left panel) and radio−undetected sources (right panel). Lower panel: Variation of total outflow rate with L_{Bol} for the radio-detected sources (left panel) and radio-undetected sources (right panel). In each plot, the scatter points represent our data with 1σ error bars, while the solid line and shaded region indicate the fitted line with a 1σ confidence band. The color in each plot corresponds to λ_{Edd}.

additional mechanism that enhances outflow kinematics in radio-detected sources. This could explain the steeper correlation between KP_{out} and L_{Bol} in the radio-detected sample and the stronger correlation of KP_{out} with λ_{Edd}. Although there is a general upward trend of outflow properties with L_{Bol}, the scatter in the plots (see Fig. 3.12) may be attributed to the complex interplay between outflows and the quantity or geometry of dense gas in the nuclear regions of these sources (Ramos Almeida et al., 2022). Moreover, the colour coding in Fig. 3.12 indicates that sources with high λ_{Edd} tend to have elevated values of L_{Bol}, $\dot{M}_{out}$, and KP_{out}. This interpretation highlights the nuanced role of AGN radiation and radio jets in influencing outflow characteristics, suggesting a more complex feedback mechanism that merits further investigation.

For the radio-detected sample of sources, we found a flat relation between the outflow properties and jet power. We obtained the best fit scaling relation of $\mathrm{KP}_{out} \propto P_{Jet}^{0.56\pm0.14}$ and $\dot{M}_{out} \propto P_{Jet}^{0.43\pm0.12}$. The results of the fits are given in Table 3.5. We also found the ratio of $\log(\frac{L_{Bol}}{P_{Jet}})$ to have a bimodal behaviour with a dividing limit at 0.4. We noticed beyond this limit, P_{Jet} is very strongly correlated with L_{Bol} with a slope of 0.96 ± 0.06 which can be seen in the upper panel of Fig. 3.13. In the lower panel of Fig. 3.13, we show the correlation between KP_{out} and P_{Jet}. Here, the sources are colour coded with $\log(\frac{L_{Bol}}{P_{Jet}})$. We found that beyond the limit of $\log(\frac{L_{Bol}}{P_{Jet}})$=0.4 i.e. for $\log(\frac{L_{Bol}}{P_{Jet}})>$ 0.4 the correlation between KP_{out} and P_{Jet} is significantly strong and steep with $\mathrm{KP}_{out} \propto P_{Jet}^{0.99\pm0.14}$. Below this limit, i.e. for higher P_{Jet} with similar L_{Bol}, KP_{out} is lower. This may be due to high power jet encountering lower interaction with the cloud where [OIII]λ5007 originates, reducing the outflow luminosity and leading to low outflow characteristics such as KP_{out} and $\dot{M}_{out}$. Alternatively, a high-power jet can ionize the gas to its higher ionization state, leading to low luminous outflow. Thus at any jet power, significant dominance of the jet power over bolometric luminosity can lead to weaker outflows.

3.4 Summary

In this study, we conducted a comparative analysis of outflow properties in radio-detected and radio-undetected sources in their central region of 500×500 square pc. Our total sample consists of 538 AGN with detected [OIII]λ5007 line, mainly Seyfert and LINER type, of which 197 are radio-detected and 341 are radio-undetected. The objective was to identify outflows, study their properties, and constrain the role of AGN radiation and/or jets in driving outflows. For this, we used spatially resolved optical spectroscopic data from MaNGA and radio observations from FIRST surveys. We studied the properties of outflows and then compared them with AGN properties. Additionally, we explored the relationship between radio properties

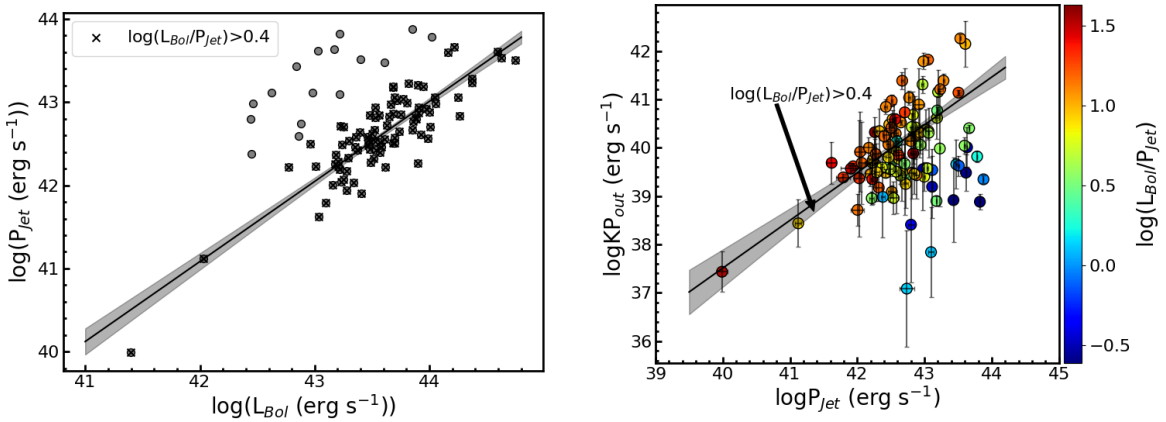

Fig. 3.13 Left panel: Jet power vs bolometric luminosity. The sources with $\log(\frac{L_{Bol}}{P_{Jet}})> 0.4$ are shown with crosses. The fitted line is for the sources with $\log(\frac{L_{Bol}}{P_{Jet}})> 0.4$. Right panel: The variation of kinetic power of outflow with jet power. The solid line with the shaded region is the fitted line with 1σ uncertainty for the given condition. The color in each plot corresponds to $\frac{L_{Bol}}{P_{Jet}}$ in log scale.

and outflow characteristics within the radio-detected sources. We summarize our main findings below.

1. To detect outflows, we carried out multiple Gaussian fits to the observed [OIII]λ5007 line. In the radio-detected sample, 56$\pm$7% of sources showed evidence of outflows. However, in the radio-undetected sample, 25$\pm$3% of sources showed outflows. Thus, in our sample, the outflow detection rate is higher in radio-detected sources compared to radio-undetected sources

2. On separating our sample of sources into Seyferts and LINERs, outflows are detected more in Seyferts (66$\pm$7%) relative to LINERs (15$\pm$2%). This is true for both the radio-detected and radio-undetected samples. The mass outflow rate and outflow power are higher for Seyferts than LINERs, but the velocity structures are higher for LINERs compared to Seyferts.

3. In both the radio-detected and radio-undetected sample, for a majority of sources ($\sim$ 80%), we found the [OIII]λ5007 line to have a blue asymmetry in addition to the narrow component. Also, in a minority of sources, in addition to the blueshifted component, we also observed the redshifted component. The blueshifted component could be the approaching side of the outflow located above the plane of the galaxy, and the redshifted

component could be the receding side of the outflow, located below the plane of the galaxy.

4. We observed distinct differences in the kinematics of the outflowing gas between the radio-detected and radio-undetected samples. The radio-detected sources exhibit higher velocity, larger velocity dispersion, greater asymmetry, larger outflow mass, and stronger kinematic power compared to the radio-undetected sources.

5. We found that in the infrared bands, more luminous outflows appear redder in colour compared to weaker outflows. Infrared colours show a positive correlation with outflow luminosity, with this dependence becoming more pronounced in the mid-infrared band. This trend is primarily attributed to the presence of larger amounts of polar dust in the more powerful outflows.

6. We found a strong correlation between the outflow characteristics, such as the $\dot{M}_{Out}$ and KP_{Out} of the outflow with the L_{Bol}. Such a correlation points to radiation from AGN being the primary driver for outflows in both radio-detected and radio-undetected samples. However, this correlation between the outflow characteristics with the bolometric luminosity is mildly steeper for the radio-detected sample compared to the radio-undetected sample. This suggests that in the radio-detected sample, radio jets could play an additional modest secondary role over and above the dominant role played by radiation in enhancing outflow kinematics.

7. Outflow characteristics are also found to show a correlation with λ_{Edd}. Sources with higher λ_{Edd} appear to have higher L_{Bol}, M_{out} and KP_{out}. This is true for both the radio-detected and radio-undetected samples.

8. For the radio-detected sample, we observed a bi-modality in the distribution of log $(\frac{L_{Bol}}{P_{Jet}})$, with the dividing line at $\log(\frac{L_{Bol}}{P_{Jet}}) = 0.4$. From, the correlation between the kinetic power of outflows and jet power, we found that at any jet power, significant dominance of the jet power over the bolometric luminosity can lead to weaker outflows.

9. We found the value of the D_n4000 parameter for our sample of radio-detected and radio-undetected sources to range between 0.8 and 2.8. About 94% of the sources in the radio-detected sample and 99% of sources in the radio-undetected sample have D_n4000 larger than 1.45, pointing to sSFR lesser than $10^{-11.5}$ yr^{-1}, which may possibly be due to negative AGN feedback.

Our findings suggest that ionized gas outflows, driven by the interaction between AGN radiation/winds and the ISM, are common across all AGN. However, the presence of radio

jets appears to affect gas kinematics further, leading to a higher rate of outflow detection in radio-detected sources, as evidenced by our study.

4

How do AGN affect the star formation of their host galaxies ?

There is observational evidence of a close correlation between supermassive black holes that power AGN and their host galaxies (Gebhardt et al., 2000), which indicates that AGN and star formation are closely linked. This connection is believed to be via AGN feedback, which plays an important role in the star formation characteristics of their hosts from nuclear scales to larger galactic scales (Harrison 2017 and references therein). One possibility for studying the impact of AGN on the star formation characteristics of their hosts is to map the star-forming regions in galaxies hosting AGN and look for correlations, if any, between the deduced star formation and AGN properties. It is natural to expect that the influence of the central AGN on their hosts could decrease from the centre to the outskirts of the galaxy (Tsai & Hwang, 2015). While simulations (Bollati et al., 2023) and observations (Lammers et al., 2023) favour feedback processes to operate in the central kpc scale region, its effect on the kpc galaxy scale is uncertain (Fiore et al., 2017). In the nearby Universe, Seyferts are ideal targets to investigate

This Chapter is based on Nandi et al. (2024)

this connection as the resolution offered by ground-based imaging observations will enable one to probe star formation on scales of a few hundred pc to a few tens of kpc.

Until now, most studies of star formation in Seyfert galaxies have been conducted in the optical, IR, or radio wavelengths using ground-based and space-based observatories. While there have been a few studies in the UV band using the *GALEX* (Martin et al., 2005), the resolution provided by *GALEX* is often insufficient to resolve star formation on pc scales. A limited number of studies have used the HST, which offers the capability to resolve pc scale structures, but it has a restricted FoV, making it observationally expensive to study a large number of sources comprehensively. To address this gap, we carried out a systematic investigation of the star formation properties of Seyfert galaxies using *UVIT*.

4.1 Our Sample

Our sample of sources was selected primarily from the catalogue of Véron-Cetty & Véron (2006). Our initial criteria involved the identification of objects classified as Seyferts in the Véron-Cetty & Véron (2006) catalogue with redshift $z < 0.02$. This redshift cut was imposed so that at the resolution of the *UVIT*, the minimum spatial scale that could be probed is about a few tens of pc. We manually inspected our sample of Seyferts in the *GALEX* database to assess their UV emission. Additionally, we imposed a size constraint, requiring that the selected objects have an angular size exceeding $2'$ but less than $12'$. We also considered some nearby LINERs for which *UVIT* observations are already available and satisfy the above criteria. This resulted in the identification of 30 objects. In this Chapter, we report results from eight sources in our sample. The details of the sources are given in Table 4.1.

4.2 Observations and data analysis

The observations of our sample of sources were made using *UVIT*. The details of the observations are given in Table 4.2. The data acquisition and the reduction processes are described in Chapter 2. The RGB images of these eight sources were made using the final FUV and NUV images from *UVIT*, along with archival optical images, which are shown in Fig. 4.1.

4.3 Analysis

The motivation of this work is to understand the star formation characteristics of the host galaxies of AGN. This involves the detection of star-forming regions in the galaxies. For this,

Name	RA J2000	DEC J2000	z	scale (pc/″)	Morphology	AGN type	M_* ($M_\odot$)	R_{25} (arcmin)	A(V) (mag)
NGC 1365	03:33:36.37	−36:08:25.45	0.005	124.4	SB(s)b	Sy 1.8	10.71 ± 0.10^a	5.61′, 3.08′, 32°	0.056
NGC 4051	12:03:09.61	44:31:52.80	0.002	41.5	SAB(rs)bc	NLSy1	10.13 ± 0.25^b	2.62′, 1.94′,135°	0.036
NGC 4151	12:10:32.58	39:24:20.63	0.003	62.3	(R′SAB(rs)ab	Sy 1.5	10.40 ± 0.25^b	3.15′,2.13′,50°	0.074
NGC 4321	12:22:54.83	15:49:19.54	0.005	103.7	SAB(s)bc	LINER	10.83 ± 0.28^c	3.71′,3.15′,30°	0.072
NGC 4388	12:25:46.75	12:39:43.51	0.008	165.8	SA(s)b	Sy 1.9	10.42^d	2.81′,0.64′,92°	0.091
NGC 5033	13:13:27.47	36:35:38.17	0.003	62.3	SA(s)c	Sy 1.9	11.01 ± 0.2^e	5.36′,2.51′,170°	0.032
NGC 6814	19:42:40.64	−10:19:24.57	0.005	103.7	SAB(rs)bc	Sy 1.5	10.34 ± 0.29^b	1.51′,1.41′	0.509
NGC 7469	23:03:15.62	08:52:26.39	0.016	331.0	(R’)SAB-(rs)a	Sy 1.2	10.88 ± 0.23^b	0.74′,0.54′,125°	0.188

Table 4.1 Details of the sources analysed in this work. Here, RA, DEC, redshift (z), morphology, AGN type and the extinction in V-band A(V) are from the NASA Extragalactic Database (NED). Here, ^{a} is from Parkash et al. (2018), ^{b} is from Bentz & Manne-Nicholas (2018), ^{c} is from Georgiev et al. (2016), ^{d} is from Andreani et al. (2018), ^{e} is from Sweet et al. (2018), M_* is the stellar mass and R_{25} is the radius of the galaxy to an optical surface brightness limit of 25 mag/arcsec^2 taken from NED.

Name	Observation ID (OBSID)	PI	Date	Filter		Exposure time(sec)	
				FUV	NUV	FUV	NUV
NGC 1365	A02_006T01_9000000776	Dewangan	08/11/2016	F169M	N279N	24905	37833
	A02_006T01_9000000802	Dewangan	17/11/2016				
	A02_006T01_9000000934	Dewangan	28/12/2016				
NGC 4051	G05_248T01_9000000486	Stalin	11/02/2018	F172M	N219M	26444	35336
	G08_071T01_9000001888	Singh	11/02/2018				
NGC 4151	G06_117T01_9000001012	Singh	08/02/2017	F154W	N219M	67547	73548
	G06_117T01_9000001046	Singh	22/02/2017				
	G06_117T01_9000001086	Singh	17/03/2017				
	G08_064T01_9000001814	Singh	04/01/2018				
	G08_064T01_9000002070	Singh	02/05/2018				
NGC 4321	A08_003T05_9000003426	Hutchings	11/01/2020	F154W	–	6296	–
NGC 4388	A02_024T01_9000001044	Mallick	21/02/2017	F154W	N245M	13520	13621
NGC 5033	G06_087T04_9000001028	Stalin	14/02/2017	F148W	N279N	2930	2948
NGC 6814	A05_037T01_9000003140	Pranoti	02/09/2019	F154W	–	46782	–
NGC 7469	G08_071T02_9000001620	Singh	18/10/2017	F172M	N245M	34493	50032

Table 4.2 Summary of observations

we used the `SExtractor` module (Bertin & Arnouts, 1996) in Python. To identify star-forming regions within each galaxy, we adopted the following criteria: DETECT_THRESH = 5σ, DETECT_MINAREA = 11 and DEBLEND_THRESHOLD = 32, where σ is the background noise. These identified star-forming regions might be contaminated by foreground objects. To remove such foreground objects, we cross-matched the identified regions with the *Gaia-DR3* (Gaia Collaboration et al., 2022) catalogue setting a cutoff in the proper motion of the regions at 10 mas yr^{-1}. If a detected star-forming region had a counterpart within $2''$ in the *Gaia* catalogue with a proper motion exceeding 10 mas yr$''$, we excluded that star-forming region from our analysis. Thus, in total we identified 418 regions in NGC 1365, 131 regions in NGC 4051, 161 regions in NGC 4151, 340 regions in NGC 4321, 20 regions in NGC 4388, 557 regions in NGC 5033, 89 regions in NGC 6814 and 26 regions in NGC 7469. These identified regions for all the galaxies are marked and are shown in Fig. 4.2.

The sizes of the identified star-forming regions varied, ranging from the point spread function (PSF) of the instrument to approximately $4-5$ times its size. We then corrected for their respective instrumental resolutions by assuming elliptical light distribution within the apertures. These corrected apertures were subsequently utilized for further analysis. The distribution of the area of the identified star-forming regions in each of the galaxies are shown in Fig. 4.3. We determined the flux of each of the star-forming regions via aperture photometry, using `photutils` package (Bradley et al., 2020). We corrected these flux measurements for extinction. For the Milky Way extinction correction, we relied on the prescription from Cardelli et al. (1989) and to correct for internal extinction, we used the UV slope (β) method (Calzetti et al., 2000). For measurements in two UV filters, one in FUV and the other in NUV, β was

calculated as

$$\beta = \frac{m_{FUV} - m_{NUV}}{-2.5log(\lambda_{FUV}/\lambda_{NUV})} - 2.0 \tag{4.1}$$

Here, m_{FUV} and m_{NUV} are the magnitudes in FUV and NUV filters with wavelengths λ_{FUV} and λ_{NUV} respectively. The values of β give an idea of the dust obscuration in the star-forming regions. Using the calculated β, we estimated the colour excess, E(B−V) using the following relation

$$E(B-V) = (\beta + 2.616)/4.684 \tag{4.2}$$

The distribution of the E(B−V) values for the identified star-forming regions are given in Fig. 4.4. We estimated the internal extinction at any particular wavelength, λ, as

$$A_\lambda = 0.44 \times E(B-V) \times k'(\lambda) \tag{4.3}$$

where, $k'(\lambda)$ is from Calzetti et al. (2000).

In cases where NUV data from *UVIT* were unavailable, we calculated the UV slope using two FUV filters. For regions where neither FUV and NUV filters nor two FUV filters were available from *UVIT*, we utilized the *GALEX* FUV and NUV images. In such instances, we convolved the instrument-corrected aperture with the *GALEX* PSF and employed those apertures to determine the extinction correction. The spatial and radial variations of internal extinction for our sample of galaxies are shown in Fig. 4.5.

After getting the extinction value for each star-forming region, we calculated the intrinsic luminosities of the star-forming regions and used them to estimate the SFR in FUV and NUV wavelengths as follows (Salim et al., 2007).

$$log(SFR_{FUV}(M_\odot yr^{-1})) = log[L_{FUV}(WHz^{-1})] - 21.16 \tag{4.4a}$$

$$log(SFR_{NUV}(M_\odot yr^{-1})) = log[L_{NUV}(WHz^{-1})] - 21.14 \tag{4.4b}$$

We calculated the surface density of the SFR (Σ_{SFR}) by taking the ratio of the SFR to the area of the star-forming regions. The spatial and radial variations of Σ_{SFR} values for our sample of sources are shown in Fig. 4.6.

4.4 Notes on Individual sources

The details of the star-forming regions of individual sources are given in Nandi et al. (2024).

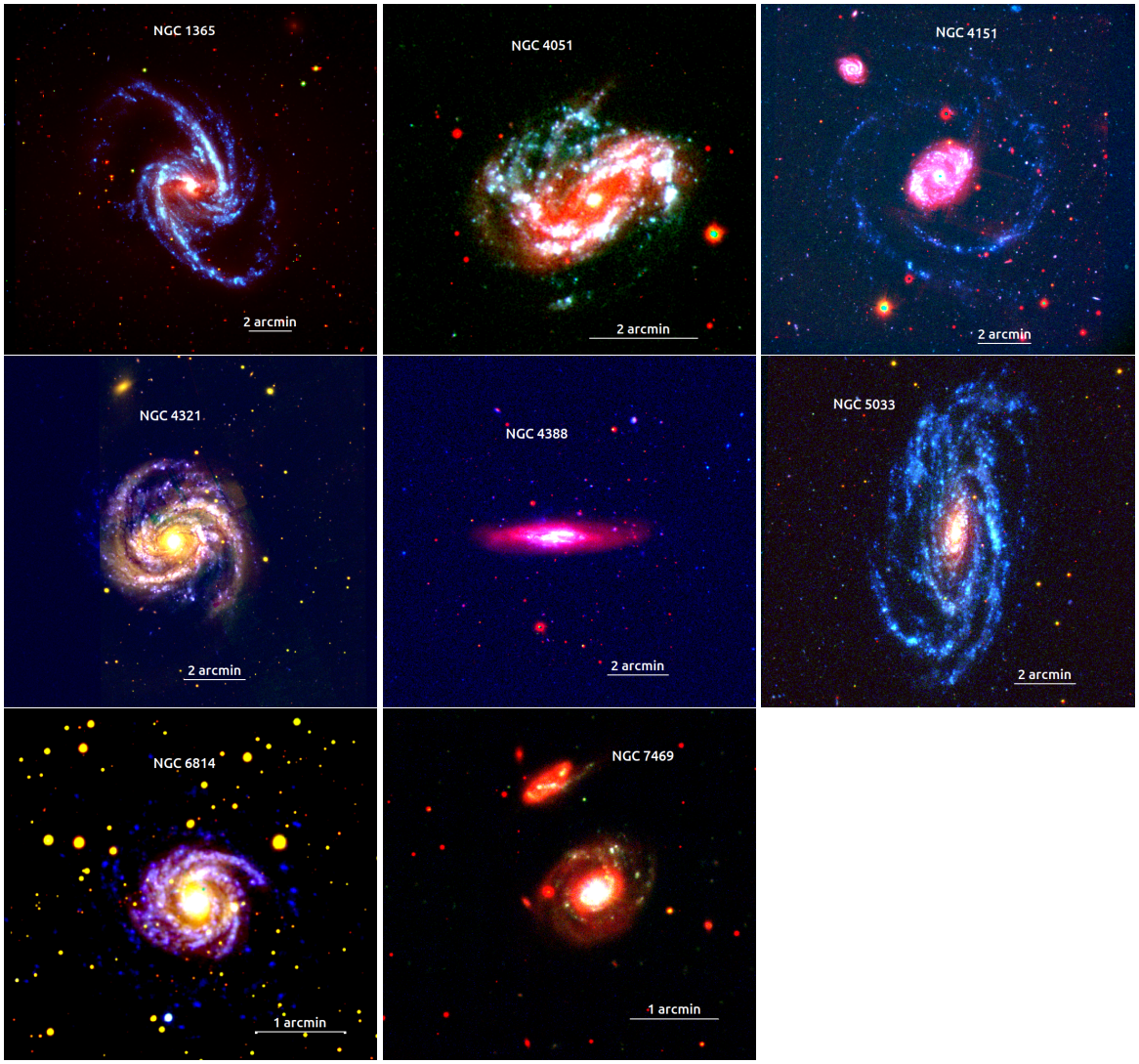

Fig. 4.1 RGB images of the sources. Here, red is the *Pan-STARRS* r band (except for NGC 1365, where it is from the *Decadal legacy survey*), green is *UVIT* NUV (except for NGC 4321 and NGC 6814, where it is *Pan-STARRS* g-band) and blue is *UVIT* FUV.

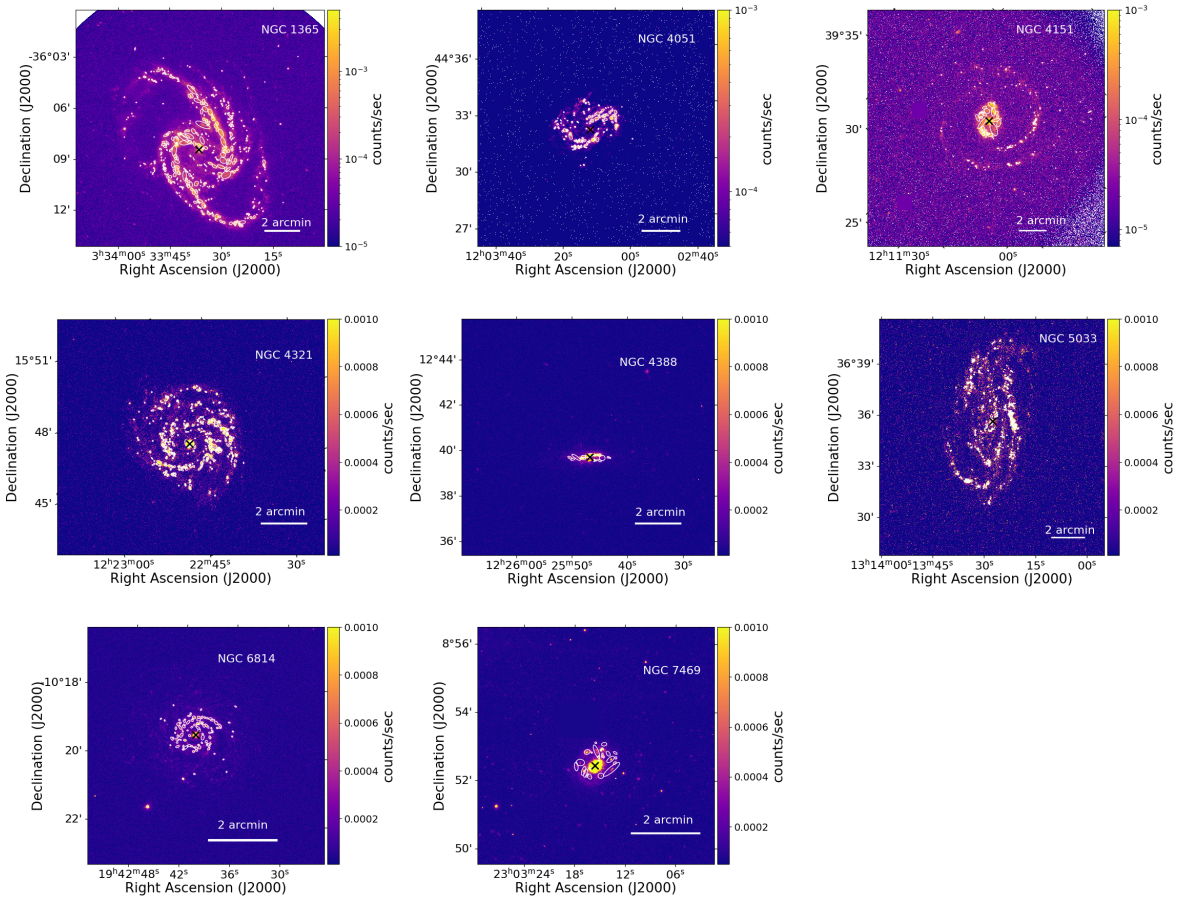

Fig. 4.2 FUV images of the objects with the identified star-forming regions marked with white ellipses. The central AGN is marked as a black cross.

4.4.1 NGC 1365

NGC 1365 at a redshift z=0.005 (de Vaucouleurs et al., 1991), is a face-on barred spiral galaxy of SB(s)b type (de Vaucouleurs et al., 1991) and harbouring a Seyfert 1.8 type AGN (Maiolino & Rieke, 1995) with a black hole of mass $M_{BH} \sim 10^{6.5}$ $M_\odot$ (Risaliti et al., 2009). NGC 1365 with an X-ray luminosity of $L_{2-10\ keV} = 10^{42}$ erg s^{-1} (Risaliti et al., 2005) is variable in X-rays, exhibiting variability on timescales of hours to years (Brenneman et al., 2013). Notably, NGC 1365 is host to a rich population of star clusters and is a prominent galaxy within a 30 Mpc distance (Whitmore et al., 2023). At radio frequencies, detection of a ring-like structure in the circumnuclear region with multiple knots of emission was reported by Saikia et al. (1994). This was followed by a more detailed study, which showed the knots of emission to have a non-thermal spectrum and a suggestion of a possible jet-like structure along a PA$\sim$ 125° (Sandqvist et al., 1995). Stevens et al. (1999) confirm the non-thermal nature of the knots and suggest that these are mostly due to multiple supernova remnants. They also suggest that the jet-like structure could be due to a nuclear bar that extends to the ring.

We identified 418 star-forming regions, with the faintest region of 23.56 mag in FUV, while the brightest region, has a brightness of 13.70 mag in the same FUV band. In the NUV, the faintest and the brightest star-forming regions have a brightness of 23.81 mag and 12.79 mag respectively. These star-forming regions span a broad range of sizes. Their sizes range from $0.042 - 11.93$ kpc^2, with average and median values of 0.713 kpc^2 and 0.215 kpc^2 respectively.

We found the colour excess, E(B−V), to vary from 0.019 mag to 0.783 mag, with an average of 0.212 mag and a median of 0.195 mag. In the FUV band, the extinction ranged from 0.08 mag to 3.428 mag, with an average of 0.93 mag and a median of 0.86 mag. Meanwhile, in the NUV band, the extinction values range from 0.06 mag to 2.51 mag, with a median of 0.63 mag and an average of 0.68 mag. We found high extinction in the inner regions compared to the outer regions (see Fig. 4.5). The Σ_{SFR} for the star-forming regions in NGC 1365 varied between $1.268 \times 10^{-3} - 22.96 \times 10^{-2}$ $M_\odot$ yr^{-2} kpc^{-2} in the FUV band, with an averageΣ_{SFR} of 8.91×10^{-3} $M_\odot$ yr^{-1} kpc^{-2}. Similarly, in the NUV band, we found the Σ_{SFR} values to vary between 9.72×10^{-4} and 55.62×10^{-2} $M_\odot$ yr^{-1} kpc^{-2}, with an average of 11.19×10^{-3} $M_\odot$ yr^{-1} kpc^{-2}. We found the distribution of the Σ_{SFR} values in both FUV and NUV to be similar. We found the extinction and Σ_{SFR} to decrease radially outwards, as can be seen in Fig. 4.5 and Fig. 4.6 respectively.

4.4.2 NGC 4051

NGC 4051, an intermediate barred spiral galaxy with a morphological type of SAB(rs)bc (de Vaucouleurs et al., 1991; Evans et al., 1996), is at a redshift of z = 0.002 (Véron-Cetty & Véron,

2006). It is a narrow line Seyfert 1 galaxy (Khachikian & Weedman, 1974b) and powered by a black hole of mass 6×10^5 $M_\odot$ (Seifina et al., 2018). It is luminous in X-rays wth $L_{2-10\ kev}$ = 2.7×10^{41} erg s^{-1} (Pounds et al., 2004), and is known to be variable across wavelengths and timescales (Peterson et al., 2000; McHardy et al., 2004; Jones et al., 2011a; Kumari et al., 2023). High-resolution observations at radio frequencies, such as with the *VLA* A-array at 8.4 GHz, show a core and two distinct components on opposite sides, while lower-resolution observations do not resolve well the inner triple but exhibit more diffuse extended emission (e.g. Jones et al., 2011b). Unlike at X-ray wavelengths, they do not find evidence of significant variability of the core at radio frequencies. From continuum-subtracted Hα images, Evans et al. (1996) identified numerous HII knots within its spiral arms.

We detected 131 star-forming regions having FUV brightness between 23.97 mag (the faintest) and 16.55 mag (the brightest). Similarly, in the NUV band, the star-forming regions varied in brightness between 24.40 mag at the faintest end and 16.69 mag at the brightest end. The areas of these star-forming regions have a wide range, varying from 0.046 kpc^2 to 2.144 kpc^2, with the average and median value of 0.341 kpc^2 and 0.207 kpc^2 respectively.

We found the E(B−V) values to span a wide range from −0.357 mag to 0.418 mag, with an average value of −0.046 mag and a median value of −0.038 mag. Extinction in the FUV band is found to vary between −1.51 mag and 1.77 mag, while, in the NUV band, we found the extinction values to vary between −1.32 mag and 1.55 mag, with mean and median values of −0.17 mag and −0.14 mag, respectively.

We found the Σ_{SFR} of the star-forming regions to have a wide range between 1.09×10^{-4} and 42.79×10^{-4} $M_\odot$ yr^{-1} kpc^{-2} in the case of FUV and between 8.1×10^{-5} and 41.22×10^{-4} $M_\odot$ yr^{-1} kpc^{-2} in the case of NUV. The average Σ_{SFR} in the FUV and NUV bands are 7.72×10^{-4} $M_\odot$ yr^{-1} kpc^{-2} and 6.98×10^{-4} $M_\odot$ yr^{-1} kpc^{-2} respectively. We found the Σ_{SFR} values to be similar in both FUV and NUV bands.

4.4.3 NGC 4151

NGC 4151 with a well-defined spiral pattern and a central bulge (de Vaucouleurs et al., 1991; Mundell et al., 1999) is an intermediate face-on spiral galaxy with a morphology of (R')SAB(rs)ab. It hosts a Seyfert 1.5 AGN (Véron-Cetty & Véron, 2006), situated at a redshift of z=0.0033 (Wolfinger et al., 2013) and powered by a black hole of mass 4.57×10^7 $M_\odot$ (Bentz et al., 2006). Its X-ray luminosity ranges between $(1.3-2.1) \times 10^{42}$ erg s^{-1} (Wang et al., 2010) and has been studied for variability over a wide range of wavelengths. It has a two-sided radio jet, and the gas-rich spiral arms, along with the bar, are prominently visible in HI images (Bosma et al., 1977). The outer spiral arms are clearly visible in both FUV and NUV images, as can be seen in Fig. 4.1 and Fig. 4.2. These two distinct spiral arms are not prominent in

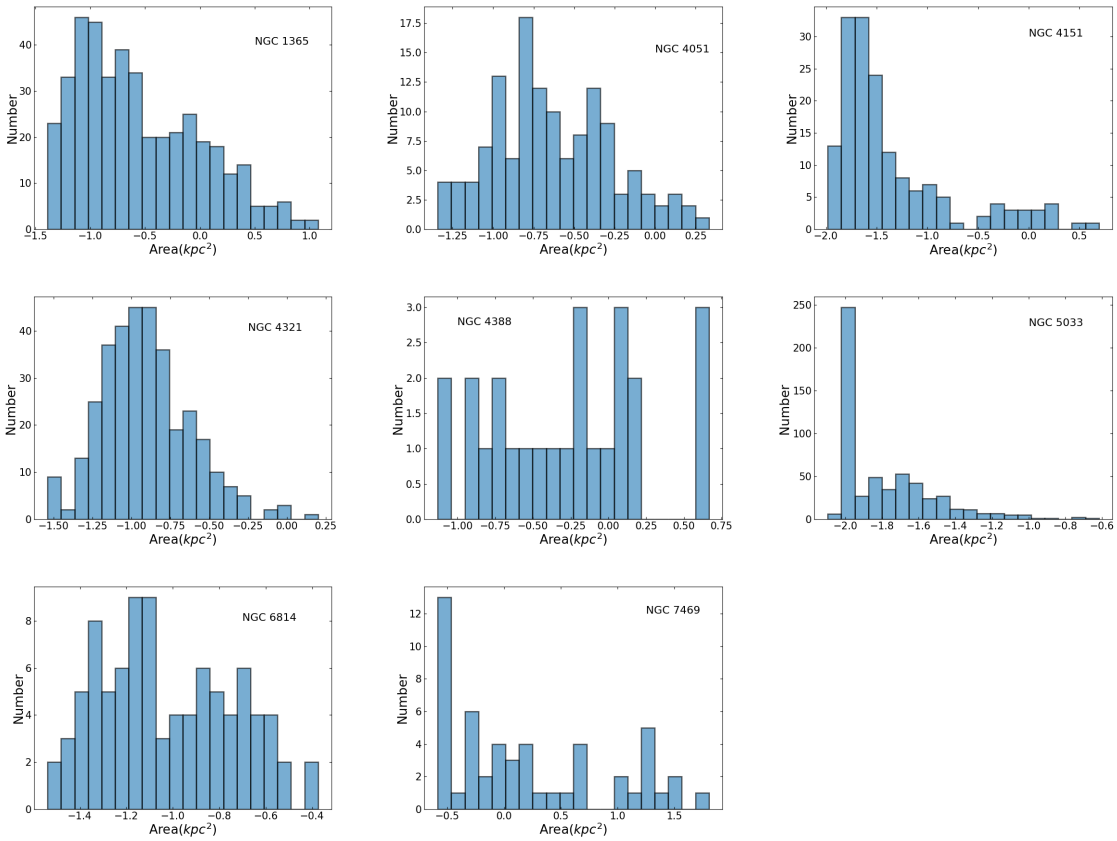

Fig. 4.3 Distributions of the area (log scale) of the identified star-forming regions in the sources studied in this work. The names of the sources are given in their respective panels.

the optical band, which are nicely traced by HI observation (Pedlar et al., 1992). The radio structure of NGC 4151 has been studied for decades. It exhibits a two-sided jet with multiple components along a PA$\sim 77^{\circ}$, with one of the components (C4) coincident with the optical nucleus of the galaxy. C4, which is presumably associated with the supermassive black hole at its centre, was found to vary at radio frequencies, but no significant motion was detected between C4 and the nearby C3 component over a 22-year period (Williams et al., 2017).

We detected 161 star-forming regions. The faintest and the brightest star-forming regions identified by us in the FUV image of NGC 4151 have a magnitude of 23.76 mag and 16.36 mag, respectively. Similarly, in the NUV band, the faintest and the brightest star-forming regions detected have a brightness value of 23.91 mag and 16.25 mag respectively. These star-forming regions have a wide range of area between 0.010 kpc^2 to 4.921 kpc^2, with an average and median area of 0.188 kpc^2 and 0.027 kpc^2 respectively. We found the colour excess, E(B$-$V), to vary between 0.032 mag and 2.446 mag, with an average value of 0.252 mag and a median value of 0.227 mag. Extinction in the FUV band varied between 0.15 mag to 3.21 mag, with an average of 1.13 mag and a median of 1.02 mag, while in the NUV band, extinction varied from 0.12 mag to 2.66 mag, with a median of 0.94 mag and an average of 0.843 mag.

The estimated Σ_{SFR} of these star-forming regions exhibited a wide range, with Σ_{SFR} values in the FUV band varying from 8.55×10^{-4} to 0.05 $M_{\odot}$ yr^{-1} kpc^{-2}. The average Σ_{SFR} in the FUV band is 48.40×10^{-4} $M_{\odot}$ yr^{-1} kpc^{-2}. In the NUV band, Σ_{SFR} values ranged between 7.72×10^{-4} and 0.07 $M_{\odot}$ yr^{-1} kpc^{-2} with an average Σ_{SFR} of 57.11×10^{-4} $M_{\odot}$ yr^{-1} kpc^{-2}.

4.4.4 NGC 4321

NGC 4321, classified as a late-type, nearly face-on grand design spiral galaxy with a SAB(s)bc morphology (de Vaucouleurs et al., 1991), is at a redshift of $z = 0.00524$ (Allison et al., 2014) and is powered by a black hole of mass $(2.5\pm0.2)\times10^7$ $M_{\odot}$ (Sarzi et al., 2002). It has two bars and a circumnuclear ring (Garcia-Burillo et al., 1998). It is categorized as HII/LINER and exhibits a relatively high X-ray luminosity, exceeding 1.9×10^{40} erg s^{-1} (González-Martín et al., 2009). In the radio, the image made with the *Effelsberg* telescope with an angular resolution of $\sim$71 arcsec shows a bright central region and an extended disk (Urbanik et al., 1986). Higher-resolution observations with the *VLA* with an angular resolution of 2 arcsec showed the central region to have a roughly circular structure with an angular extent of $\sim$20 arcsec. Radio emission appears to peak at the optical nucleus and also at an enhanced region $\sim$7 arcsec to the east near an optical condensation, besides emission from SN1979c (Weiler et al., 1981). Moreover, strong activity has been observed across optical and radio wavelengths, leading to the classification of NGC 4321 as a transition galaxy, bridging the gap between normal and AGN galaxies (Immler et al., 1998).

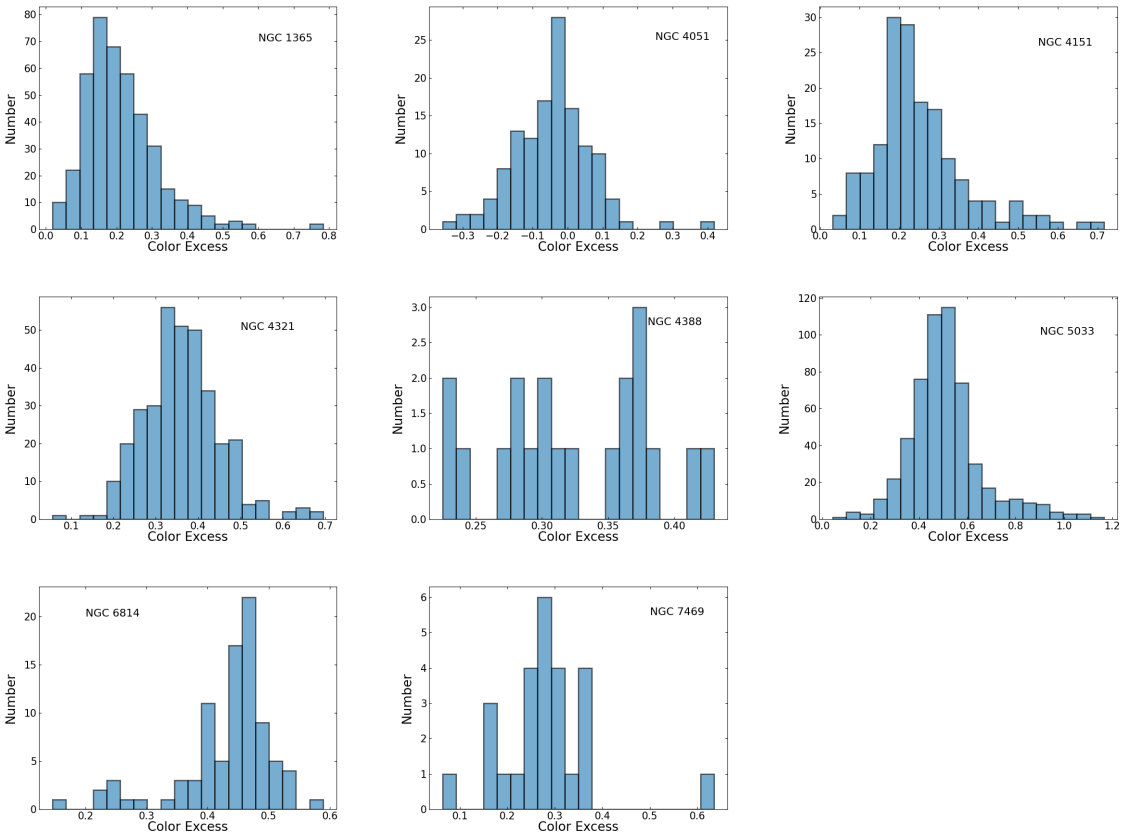

Fig. 4.4 Distributions of E(B−V) of the identified star-forming regions in the sources studied in this work. The names of the sources are given in their respective panels.

NGC 4321 has giant molecular associations in various regions, including the bar, spiral arms, and circumnuclear ring (Pan & Kuno, 2017). It has been observed that star formation is most active within the circumnuclear ring, with lower activity occurring in the inter-arm regions (Pan & Kuno, 2017). Star formation in the circumnuclear region or nuclear rings is attributed to bursts triggered by the Inner Lindblad resonance (Arsenault 1989). Additionally, Hα emission is prominent on the leading side of the bar and spiral arms, contributing to the understanding of star-forming regions in the galaxy (Pan & Kuno, 2017). Further studies, such as those by Ferreras et al. (2012), have investigated young star-forming regions in the NUV and optical ranges. While these studies confirmed the association of Hα emission with the nuclear region, they did not find a significant correlation between the distance from these regions and the age or dust content.

We identified 340 star-forming regions in NGC 4321. These regions have a wide range in brightness, with values ranging between 22.19 mag and 13.92 mag in the FUV band. They have a range of sizes from 0.029 kpc^2 to 1.587 kpc^2, with an average area of 0.159 kpc^2 and a median of 0.116 kpc^2. The E(B$-$V) values within these regions range between 0.056 mag and 0.695 mag, with average and median values of 0.361 mag and 0.356 mag, respectively. We found the extinction in the FUV band to cover a wide range from 0.25 mag to 3.11 mag, with an average and median of 1.62 mag and 1.59 mag, respectively.

The Σ_{SFR} within these star formation regions in the FUV band have a wide range from 5.82×10^{-3} to 55.17×10^{-2} M$_\odot$ yr^{-1} kpc^{-2}, with an average Σ_{SFR} of 3.43×10^{-2} M$_\odot$ yr^{-1} kpc^{-2}. Both extinction and Σ_{SFR} were found to show a gradual decline from the centre towards the outer regions of the galaxy as can be seen in Fig. 4.5 and Fig. 4.6.

4.4.5 NGC 4388

NGC 4388 is a nearly edge-on spiral galaxy, classified as type SA(s)b with a major axis PA of 91° (Paturel et al., 2003; de Vaucouleurs et al., 1991). Located at a distance of approximately 37.55 Mpc, corresponding to a redshift of z=0.00842 (Lu et al., 1993), this galaxy exhibits a short bar whose strength depends on the eccentricity of stellar or gas orbits (Veilleux et al., 1999). At its centre, NGC 4388 hosts a type 2 Seyfert AGN with a supermassive black hole of mass $(8.4\pm0.2)\times10^6$ M$_\odot$ (Tueller et al., 2008; Kuo et al., 2011). It is a strong X-ray source, with an X-ray luminosity of $L_{2-10\ kev} = 1 \times 10^{42}$ erg s^{-1} (Forster et al., 1999). *VLA* observations have revealed an elongated blob with an extent of ∼13 arcsec to the north of the galaxy and a collimated structure of ∼2.8 towards the south, the observed asymmetry possibly being due to an asymmetric distribution of ISM (Hummel & Saikia, 1991). More recently, Sargent et al. (2024) have made a detailed study with the *VLA* in both total intensity

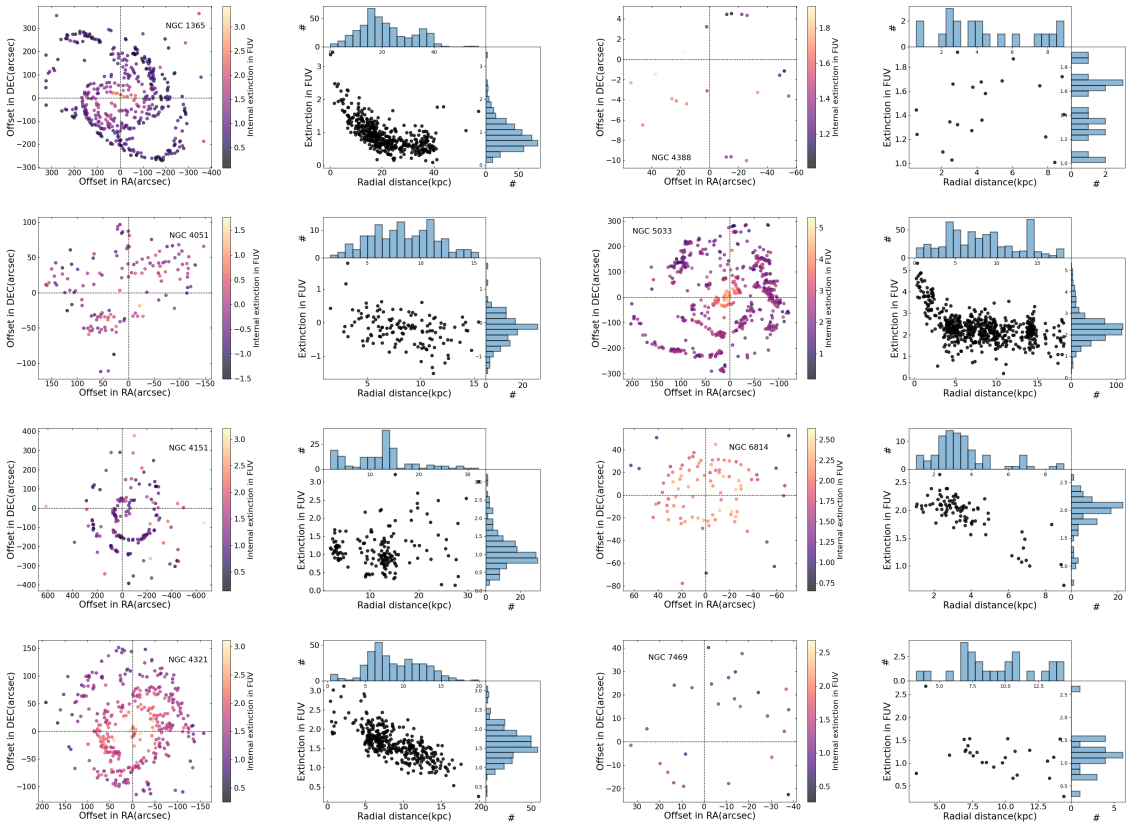

Fig. 4.5 Spatial (left panel) and radial (right panel) variation of internal extinction for each source.

and linear polarization and have suggested that the radio continuum emission is due to AGN winds interacting with the local ISM.

NGC 4388 also exhibits significant dust obscuration, with dust bands extending to approximately 1.5 kpc from the centre of the disk (Falcke et al., 1998). Studies have shown that the galaxy possesses a truncated HI disc and gas components outside the plane, suggesting a possible interaction with the intergalactic medium (Singh et al., 2019). This interaction is believed to have involved ram pressure stripping, resulting in the loss of approximately 85% of the HI gas component in NGC 4388, subsequently disrupting star formation in the galaxy (Cayatte et al., 1990). Recent investigations have indicated star-forming regions not coplanar with the disk, contributing to the extended outflows and suggesting recent starburst events in the spiral arms and circumnuclear region of the galaxy (Damas-Segovia et al., 2016).

We detected 20 star-forming regions in NGC 4388. These regions have FUV brightness between 22.06 mag and 15.79 mag, while in the NUV, the brightness of the star-forming regions varied between 22.07 mag and 15.72 mag. The areas of these regions were found to show considerable variation, spanning from 0.074 kpc^2 to 4.636 kpc^2, with an average area of 1.268 kpc^2 and a median of 0.754 kpc^2. The E(B−V) values span a range from 0.23 mag to 0.43 mag, with an average of 0.33 mag and a median of 0.32 mag. Extinction values in the FUV band were found to have a wide range from 1.01 mag to 1.92 mag, with a mean and median of 1.46 mag and 1.43 mag, respectively, while in the NUV band, extinction varied between 0.78 mag and 1.49 mag, with a median of 1.11 mag and an average of 1.13 mag. The Σ_{SFR} within these regions in the FUV were found to vary between 5.74×10^{-3} and 103.79×10^{-3} $M_\odot$ yr^{-1} kpc^{-2}. with an average Σ_{SFR} of 27.23×10^{-3} $M_\odot$ yr^{-1} kpc^{-2}. Similarly, in the NUV band, we found Σ_{SFR} to range between 7.16×10^{-3} to 108.92×10^{-3} $M_\odot$ yr^{-1} kpc^{-2}. We found the average Σ_{SFR} in the NUV band of 31.38×10^{-3} $M_\odot$ yr^{-1} kpc^{-2}.

4.4.6 NGC 5033

NGC 5033 is an SA(s)c-type non-barred spiral galaxy at a redshift of z=0.00291. It has a central bulge with a mass of approximately 2×10^{10} $M_\odot$. It is a Seyfert 1.9 galaxy and hosts a supermassive black hole at its centre, with a mass ranging from $5-12 \times10^6$ $M_\odot$. It is luminous in X-rays with $L_{2-10\ kev} = 2.3 \times 10^{41}$ erg s^{-1} (Terashima et al., 1999). Although high-resolution radio observations show a core-jet morphology, the radio emission from the inner disk is dominated by a starburst, with the core-jet structure contributing only 7% of the flux density at 1.4 GHz (Pérez-Torres & Alberdi, 2007). They also report evidence of a "radio spur" due to a hot bubble caused by sequential supernova explosions. The galaxy is variable in X-ray wavelengths (Papadakis et al., 2008).

The galaxy's flat disk has a high inclination of 67.5° and shows signs of possible warping, possibly resulting from interactions or mergers. Near-infrared and millimetre observations reveal a small nuclear bar, while the presence of HII regions following a ring-like pattern is evident in Hβ intensity maps. A bright bar of light from the unresolved nucleus has been observed in NUV images. Radio 21cm-line studies show similarities between the HI distribution and optical characteristics, and it has been found that Σ_{SFR} is directly related to the total gas surface density. Comprehensive CO*(1−0)* observations suggest that there is no starburst phenomenon in the nuclear region. Instead, star-forming regions are present in the disk region, supported by observations from the *GALEX* telescope. The radio and FIR luminosities of the inner regions indicate evidence of a recent short starburst in NGC 5033 (Pérez-Torres & Alberdi, 2007).

We identified 557 star-forming regions with a wide range of brightness. The faintest region in the FUV has a brightness of 22.51 mag, while the brightest region has a brightness of 15.43 mag. Similarly, in the NUV band, the faintest and brightest star-forming regions have brightness values of 22.86 mag and 14.14 mag respectively. These star-forming regions have varied sizes, ranging from 0.008 kpc^2 to 0.242 kpc^2, with an average value of 0.020 kpc^2. We found E(B−V) to vary from 0.04 mag to 1.17 mag, with an average value of 0.51 mag and a median of 0.49 mag. Extinction values in the FUV were found to lie between 0.19 mag and 5.34 mag, with an average of 2.33 mag and a median of 1.58 mag. In the NUV band, the extinction is relatively lower, with values between 0.14 mag and 3.73 mag, with a median of 1.58 mag and an average of 1.63 mag.

The Σ_{SFR} of these star-forming regions varied between 3.25×10^{-3} and 53.02×10^{-2} $M_\odot$ yr^{-1} kpc^{-2} in FUV and between 24.81×10^{-4} and 12.78×10^{-2} $M_\odot$ yr^{-1} kpc^{-2} in NUV. We found the Σ_{SFR} to gradually decrease radially from the centre to the outskirts, as can be seen in Fig. 4.6.

4.4.7 NGC 6814

NGC 6814 is a grand design spiral galaxy of the SAB(rs)bc type, with a face-on orientation (de Vaucouleurs et al., 1991). It is characterized by a compact bulge in both near-infrared and optical wavelengths, along with a relatively weak bar extending approximately ten arcseconds in the North-South direction (Sánchez-Portal et al., 2004; Slavcheva-Mihova & Mihov, 2011). Situated at a distance of 23.22 Mpc, this galaxy hosts a type 1.5 Seyfert AGN at its centre (Springob et al., 2005), with a black hole of mass $(1.85 \pm 0.35) \times 10^7$ $M_\odot$ (Bentz et al., 2009). It is variable in the optical, UV, and X-ray wavelengths, with the highest variability observed in X-rays (Gallo et al., 2021; Troyer et al., 2016). It is luminous in X-rays with $L_{2-10\ kev} = 2.04 \times 10^{42}$ erg s^{-1} (Tortosa et al., 2018). At radio frequencies, the central region appears extended

in the north-south direction with a possible component towards the west, and no significant jet emission when observed with the *VLA* A-array, (Ulvestad & Wilson, 1984; Xu et al., 1999).

Extensive work by Knapen et al. (1993) has identified numerous HII regions within the galaxy, with a comprehensive study of the luminosity functions of these regions. Interestingly, the luminosity function exhibits similar characteristics in both the outer and inner arms, offering valuable insights into the galaxy's star formation processes. In addition to HII regions, NGC 6814 displays ring-like distributions of HII, potentially featuring kinematic warping, as suggested by Liszt & Dickey (1995). Moreover, in the UV spectrum, numerous star-forming regions are evident along the spiral arms, with these arms branching into multiple fragments observable in the *GALEX* images (Sandage & Bedke, 1994).

We identified 89 star-forming regions in NGC 6814, with the faintest region at 21.21 mag and the brightest at 16.43 mag in the FUV band. These regions exhibited a range of sizes, with areas ranging from 0.029 kpc^2 to 0.422 kpc^2, with an average area of 0.118 kpc^2 and a median area of 0.082 kpc^2. The E(B−V) values in the regions ranged from 0.15 mag to 0.59 mag, with an average of 0.43 mag. Regarding extinction in the FUV band, it was found to vary between 0.65 mag to 2.64 mag, with an average of 1.94 mag.

The Σ_{SFR} of the star-forming regions identified in NGC 6814, showed variations, with the Σ_{SFR} values in the FUV band ranging from 8.96×10^{-3} to 65.25×10^{-2} $M_\odot$ yr^{-1} kpc^{-2}, with an average of 4.19×10^{-2} $M_\odot$ yr^{-1} kpc^{-2}. We found a gradual radial decrease of extinction and SFR from the centre to the outskirts of the galaxy (see Fig. 4.5 and Fig. 4.6).

4.4.8 NGC 7469

NGC 7469 is classified as an intermediate, nearly face-on spiral galaxy with a morphological type of (R')SAB(rs)a (de Vaucouleurs et al., 1991). This galaxy is located at a redshift of z=0.01627 (Springob et al., 2005). It hosts a Seyfert 1.5 type AGN (Véron-Cetty & Véron, 2006) with a black hole of mass 1.1×10^7 $M_\odot$ (Peterson et al., 2014; Lu et al., 2021). It is known for its strong X-ray emission, with a X-ray luminosity of $L_{2-10\ kev} = 10^{43}$ erg s^{-1} (Asmus et al., 2015).

One of the prominent features of this galaxy is its circumnuclear starburst ring, situated at a distance of about 1 kpc from its centre. This starburst ring has been extensively observed across various wavelengths (Xu & Wang, 2022). High-resolution radio continuum observations show a nucleus, which is the brightest feature, and more extended emission from the circumnuclear starburst with several peaks of emission. The brightest of the compact components is a radio supernova (Colina et al., 2001). Additionally, from observations of molecular line emission at millimetre wavelengths Davies et al. (2004) suggest the presence of either a bar or a pair of spiral arms located between these ring-like structures. Marquez & Moles (1994) suggest that

the star-forming activities in this galaxy exhibit unique characteristics, potentially influenced by its Hα emission, which may be attributed to the nearby companion galaxy IC 5283.

In NGC 7469, we identified 26 star-forming regions. We detected more star-forming regions in the northern spiral arm, which may be due to the effect of interaction with nearby galaxy IC 5283, as mentioned by Marquez & Moles (1994). These regions in FUV have brightness ranging between 24.47 mag and 17.67 mag. In the NUV band, the faintest star-forming region is at 24.63 mag, and the brightest is at 17.65 mag. Also, we found the areas of these star-forming regions to vary significantly, ranging from 0.295 kpc^2 to 63.642 kpc^2. On average, the star-forming regions have an average area of 12.026 kpc^2. The E(B$-$V) in these regions range from 0.06 mag to 0.64 mag. In the FUV band, we found extinction values that range from 0.27 mag to 2.68 mag, with an average of 1.17 mag. Similarly, in the NUV band, we found the extinction to vary from 0.22 mag to 2.21 mag, with a median of 0.97 mag.

The Σ_{SFR} within these star-forming regions exhibits a wide range. In FUV, Σ_{SFR} varies from 8.0×10^{-4} to 49.39×10^{-3} M$_\odot$ yr^{-1} kpc^{-2}, with an average of 5.72×10^{-3} M$_\odot$ yr^{-1} kpc^{-2}. In NUV, we found Σ_{SFR} to vary from 7.2×10^{-4} to 77.26×10^{-3} M$_\odot$ yr^{-1} kpc^{-2}, with an average Σ_{SFR} of 7.08×10^{-3} M$_\odot$ yr^{-1} kpc^{-2}.

4.5 Global picture

For the galaxies examined in this study, we observed a positive correlation between the median surface density of star formation and the extinction in the FUV band, with a Pearson correlation coefficient of 0.95 and a p-value of 0.0003. This relationship is illustrated in the left panel of Fig. 4.7. The best-fitted line to this correlation is given by:

$$\log\left(\frac{\Sigma_{SFR}}{M_\odot \mathrm{yr}^{-1}\mathrm{kpc}^{-2}}\right) = (0.82 \pm 0.11)A(FUV) - (3.17 \pm 0.16) \tag{4.5}$$

We determined the SFR using Equation 4.4 within the circumnuclear region, employing 1 kpc radius aperture, and computed the total SFR using the optical R$_{25}$ aperture. In both cases, we corrected for AGN flux contamination using a 1.4$''$ radius aperture. Here, R$_{25}$ represents the radius at which the surface brightness reaches 25 mag per square arcsec in the optical B band. The results of these calculations are provided in Table 4.4.

We positioned our sources on the stellar mass versus the SFR plane and compared their locations relative to the main sequence (MS) as described by Renzini & Peng (2015). Notably, four of our sources fell within the MS, one above it and three below it. This distribution is illustrated in the right panel of Fig. 4.7. The position of the AGN in M$_*-$SFR below the MS has also been noticed by Salim et al. (2007).

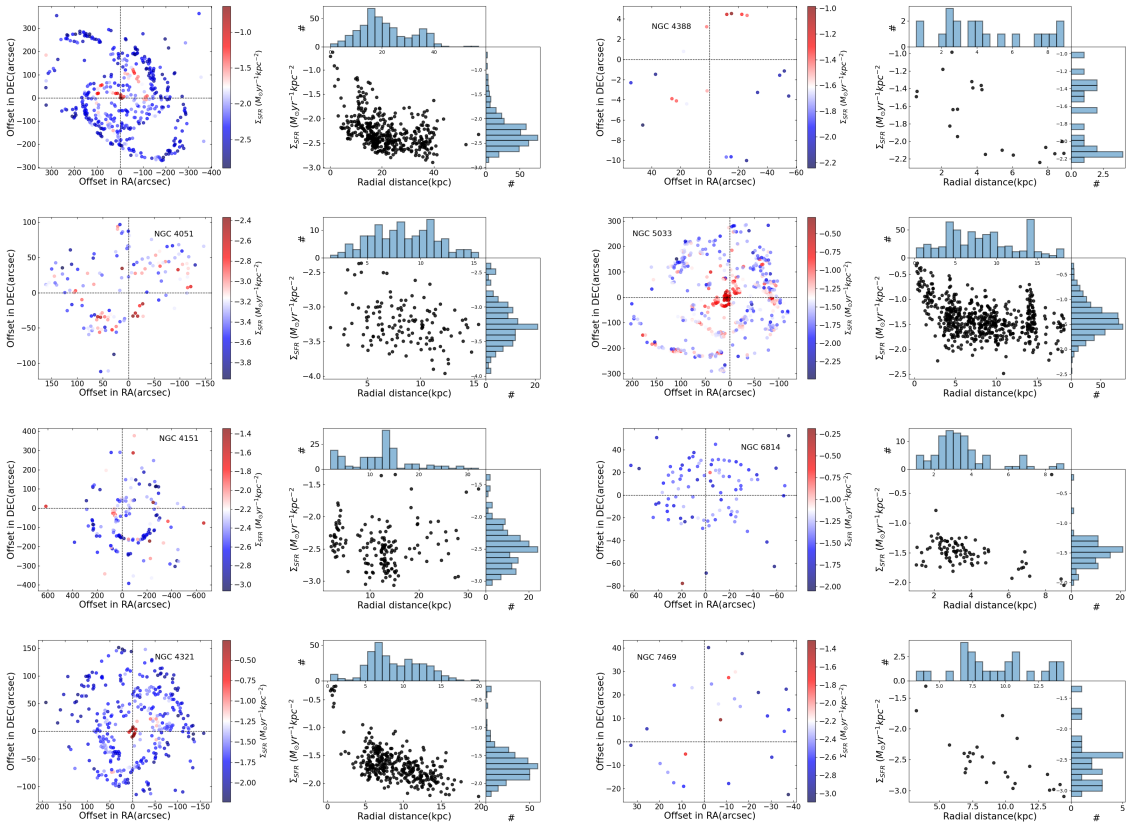

Fig. 4.6 Spatial (left panel) and radial (right panel) variation of Σ_{SFR} in log scale.

Name	N	Mean						Median					
		area (kpc^2)	E(B−V)	A_{FUV} (mag)	A_{NUV} (mag)	Σ_{SFR}^{FUV}	Σ_{SFR}^{NUV}	area (kpc^2)	E(B−V) (mag)	A_{FUV} (mag)	A_{NUV} (mag)	Σ_{SFR}^{FUV}	Σ_{SFR}^{NUV}
NGC 1365	418	0.713	0.212	0.93	0.68	8.90	11.19	0.215	0.195	0.86	0.63	4.65	4.83
NGC 4051	131	0.341	−0.046	−0.19	−0.17	0.77	0.70	0.207	−0.038	−0.16	−0.14	0.54	0.48
NGC 4151	161	0.187	0.252	1.13	0.94	4.84	5.71	0.027	0.227	1.02	0.84	3.32	3.56
NGC 4321	340	0.159	0.356	1.62	−−	34.37	−−	0.116	0.36	1.60	−−	20.02	−−
NGC 4388	20	1.268	0.325	1.46	1.13	27.23	31.38	0.755	0.318	1.43	1.11	19.04	23.05
NGC 5033	557	0.021	0.509	2.33	1.63	57.73	128.34	0.013	0.494	2.26	1.58	37.75	62.33
NGC 6814	89	0.120	0.432	1.94	−−	41.96	−−	0.083	0.452	2.03	−−	32.95	−−
NGC 7469	26	12.026	0.277	1.17	0.96	5.71	7.08	4.973	0.277	1.17	0.97	2.66	2.88

Table 4.3 Summary of the identified star-forming regions for all sources. The values of Σ_{SFR} are in units of $10^{-3} M_\odot\ yr^{-1}\ kpc^{-2}$.

Furthermore, we observed a positive correlation between the SFR and the stellar mass. Utilizing a linear regression analysis, we determined a correlation coefficient of 0.83 and a p-value of 0.02. The equation represents the resulting best-fitted line:

$$\log\left(\frac{SFR_{total}}{M_{\odot}\mathrm{yr}^{-1}}\right) = (1.47 \pm 0.44)\log\left(\frac{M_{\star}}{M_{\odot}}\right) - (15.39 \pm 4.65) \tag{4.6}$$

We identified a modest positive correlation between the ratio of the nuclear SFR ($SFR_{Nuclear}$) to the total SFR (SFR_{Total}) and the Eddington ratio, λ_{Edd}. Here, λ_{Edd} represents the ratio of the bolometric luminosity (L_{Bol}) to the Eddington luminosity (L_{Edd}). To estimate L_{Bol}, we utilized the observed $L_{2-10\ keV}$ and applied the relation $\log(L_{Bol}) = 0.0378 \times \log(L_{2-10\ keV})^2 - 2.00 \times \log(L_{2-10\ keV}) + 60.5$ (Ichikawa et al., 2017), while L_{Edd} was calculated as $L_{Edd} = 1.26 \times 10^{38}\ (M_{BH}/M_{\odot})$ erg s^{-1}. This relationship is depicted in Fig. 4.8. Performing a linear least squares fit to the data points yielded a correlation coefficient of 0.67 and a p-value of 0.06. The best-fitted line is

$$\frac{SFR_{Nuclear}}{SFR_{Total}} = (0.05 \pm 0.02) log(\lambda_{Edd}) + (0.31 \pm 0.05) \tag{4.7}$$

This correlation bears resemblance to the findings of Mountrichas & Buat (2023) regarding the relationship between SFR and λ_{Edd}. However, we noted that this correlation is heavily influenced by two points, NGC 7469 and NGC 4051. Thus, further observations with more sources are required to confirm this correlation robustly. Nevertheless, the observed correlation suggests that AGN activity (jet and/or radiation) positively influences the star formation characteristics near the nuclear region, with minimal impact observed at greater distances from the nuclear region. However, disentangling the contribution of AGN jet and radiation is not possible using only the observations reported here. Our observation aligns with both simulations (Bollati et al., 2023) and observational studies (Lammers et al., 2023), which support the operation of feedback processes primarily within the central kpc region in AGN host galaxies.

4.6 Summary

We carried out an investigation of the star formation characteristics of galaxies hosting AGN using observations carried out in UV. Our sample consists of seven Seyferts and one LINER. Our approach involved the identification of star-forming regions, carrying out aperture photometry of the identified star-forming regions, correcting the derived brightness for both Milky Way and internal extinction, estimation of SFR and the correlation of SFR with various derived parameters. The findings of this work are summarized below.

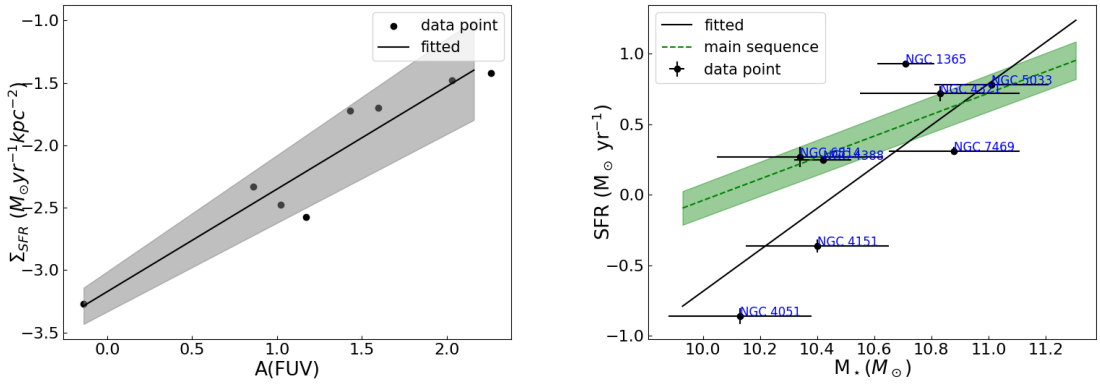

Fig. 4.7 Left panel: Variation of median Σ_{SFR} against median extinction in FUV of star-forming regions for the sources studied in this work. Right panel: Variation of SFR with stellar mass. The dotted line is the MS of star formation from Renzini & Peng (2015), and the solid line is the best-fitted linear regression line.

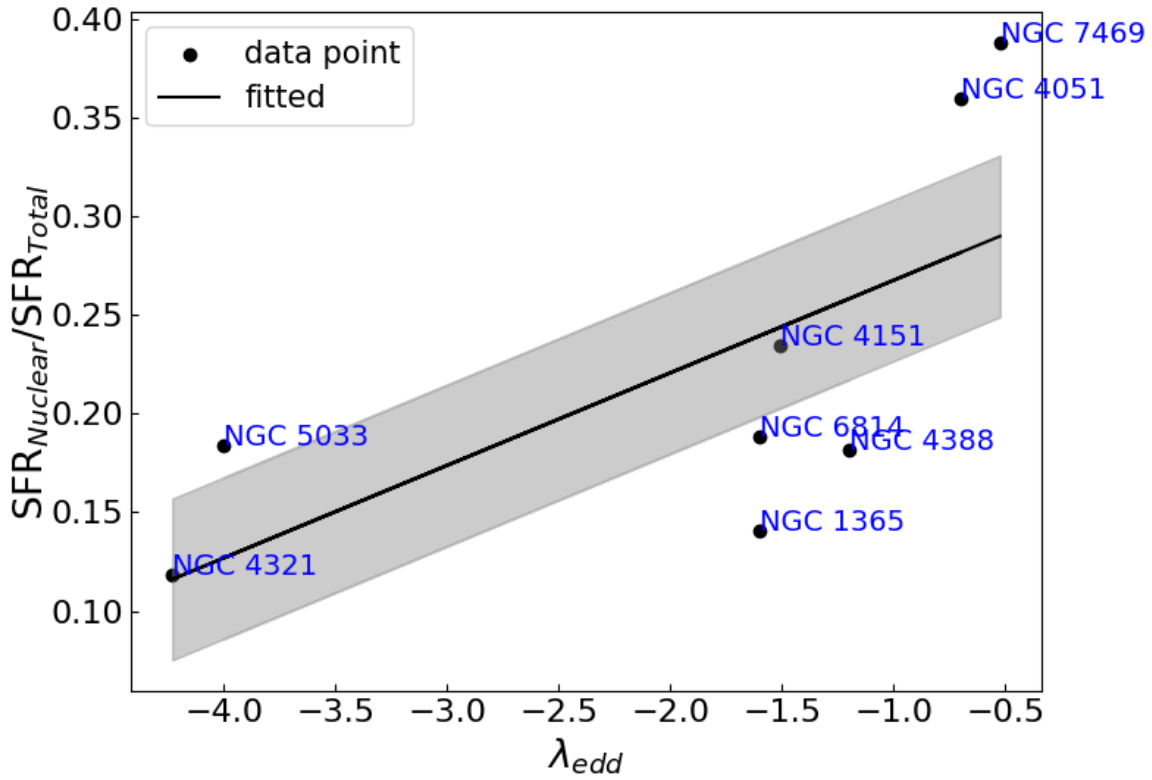

Fig. 4.8 Variation of the ratio of $SFR_{Nuclear}$ to SFR_{Total} with λ_{Edd}.The solid line is the linear least squares fit to the data, and the shaded region is the 95% confidence region.

Name	SFR_{Total}	$SFR_{Nuclear}$	Σ_{SFR}^{Total}	$\Sigma_{SFR}^{Nuclear}$
NGC 1365	8.469±0.128	1.192±0.019	2.83±0.04	94.82±1.62
NGC 4051	0.138±0.008	0.050±0.003	1.40±0.08	15.82±0.9
NGC 4151	0.434±0.019	0.102±0.004	1.48±0.07	8.12±0.41
NGC 4321	5.210±0.281	0.617±0.033	3.72±0.21	48.11±2.60
NGC 4388	0.32±0.005	1.77±0.02	3.22±0.04	25.57±0.4
NGC 5033	6.058±0.0997	1.116±0.024	10.34±0.20	88.78±1.91
NGC 6814	1.859±0.134	0.351±0.025	7.25±0.52	27.90±2.00
NGC 7469	2.042±0.057	0.792±0.030	4.25±0.14	63.00±2.41

Table 4.4 The properties of the galaxies in FUV. The units of SFR are in $M_\odot$ yr^{-1}, while that of Σ_{SFR} are in units of 10^{-3} $M_\odot$ yr^{-1} kpc^{-2}.

1. We identified many star-forming regions for all eight galaxies hosting AGN. For NGC 5033, we detected the maximum number of star-forming regions. Most of the identified star-forming regions have sizes in excess of 30 pc, with areas ranging between 0.010 and 63.642 kpc^2.

2. The extinction corrected SFR of the star-forming regions, considering all the sources studied in this work, is found to range between 1.09×10^{-4} $M_\odot$ yr^{-1} and 22.96×10^{-2} $M_\odot$ yr^{-1} in FUV, while in NUV it varies between 8.15×10^{-5} and 6.634 $M_\odot$ yr^{-1}. We found the Σ_{SFR} in NUV to be larger than that at FUV, though the median values are found to be similar.

3. We detected two outer spiral arms for NGC 4151 in both FUV and NUV bands. These spiral arms are much extended beyond the R25 aperture.

4. For five galaxies, NGC 1365, NGC 4051, NGC 4321, NGC 5033 and NGC 6814, we found both the internal extinction and the Σ_{SFR} to gradually decrease from the centre towards the outer regions, while this was not significant in the other sources.

5. We found a positive correlation between the median Σ_{SFR} and the median extinction in FUV for the star-forming regions.

6. Among the observed sources, four are situated within the MS of star-forming galaxies, while the remaining four are positioned away from the MS.

7. All sources display a positive correlation between SFR and M_*, with a slope that is notably steeper than MS.

8. We found the SFR in the nuclear region to be dominant over the total SFR.

9. The ratio of $SFR_{Nuclear}$ to SFR_{Total} exhibits a weak positive correlation with λ_{Edd}. This correlation points to the influence of AGN on enhancing the star formation characteristics of the hosts and the impact being dominant in the central region with no effect on scales beyond the nuclear region probed in this work.

5

Nature of feedback at different spatial scales in NGC 4395

Star formation characteristics of galaxies hosting AGN have been studied reasonably extensively, but similar studies for dwarf galaxies with $M_* < 10^{10}$ $M_\odot$ are extremely limited. Understanding the nature of star formation in the AGN hosting dwarf galaxies is important as these systems are expected to be powered by small or IMBH (Reines, 2022). Studies of such objects in the nearby Universe may provide valuable insights into understanding how similar objects may have evolved in the early Universe. Earlier, theoretical studies on the regulation of star formation in dwarf galaxies has been attributed to radiation from young stars and supernova (SN) explosions (Benson et al., 2002). However, recent theoretical studies do indicate that AGN could play a significant role in regulating star formation in dwarf galaxies (Koudmani et al., 2022). Observationally, there is evidence of AGN feedback operating in dwarf galaxies covering angular sizes smaller than about an arcmin (Penny et al., 2018). It is important to extend similar studies to a large range of spatial scales. Though AGN feedback effects are observationally known in massive galaxies, such as AGN inhibiting as well as enhancing star

This Chapter is based on Nandi et al. (2023a)

formation, observational evidences for AGN feedback in dwarf galaxies are very limited (Penny et al., 2018; Greene et al., 2020; Baldassare et al., 2020; Schutte & Reines, 2022). Therefore, detailed studies on the star formation characteristics of dwarf galaxies hosting AGN are needed, first, to characterize their star formation properties and second, to find evidence of the feedback processes, if any, in them.

NGC 4395 is a nearby dwarf galaxy situated at a distance of 4.3 Mpc (Thim et al., 2004). It hosts a low luminosity Seyfert type AGN and is powered by a black hole with a mass between $10^4 - 10^5$ $M_\odot$. For example, from reverberation mapping observations in the UV band carried out with the *Space Telescope Imaging Spectrograph* on the *HST*, Peterson et al. (2005) found the mass of the black hole in NGC 4395 as $M_{BH} = (3.6 \pm 1.1) \times 10^5$ $M_\odot$. However, recently, using the response of the Hα emission line to the variations in the V-band continuum, Woo et al. (2019) found a lower value of $M_{BH} = (9.1^{+1.5}_{-1.6} \times 10^3)$ $M_\odot$. NGC 4395 shows other characteristics of a Seyfert 1.8 type AGN (Véron-Cetty & Véron, 2006), such as variable emission in the optical and X-rays (Lira et al., 1999) and a collimated radio structure with components on opposite sides of the galaxy nucleus (Wrobel et al., 2001; Saikia et al., 2018; Yang et al., 2022). However, it has been found to have a low bolometric luminosity between $10^{40} - 10^{41}$ erg s^{-1} (Lira et al., 1999; Filippenko & Ho, 2003; Brum et al., 2019). Adopting a cosmology of $H_0 = 70$ km s^{-1} Mpc^{-1}, $\Omega_M = 0.7$, $\Omega_{vac} = 0.3$ and a distance of 4.3±0.3 Mpc (Thim et al., 2004), $1''$ in NGC 4395 corresponds to 21 pc.

5.1 Observations and data analysis

We used new UV observations from *UVIT*, optical Hα data from *HCT*, and archival optical observations from the *Nordic Optical Telescope (NOT)*. The *UVIT* observations were conducted on 27 February 2018 in photon counting mode with a frame rate of 34 frames per second, using F148W, F172M, N219M, and N263M filters. Optical Hα and broad R-filter observations were obtained on 22 December 2021 with the *HFOSC* instrument on *HCT*. The observation log is provided in Table 5.1. Data reduction and calibration followed the methods described in Chapter 2. The calibrated Hα line image was created by subtracting the calibrated R-band image from the narrow-band Hα image following Waller (1990):

$$f(line) = \frac{[f_\lambda(N) - f_\lambda(B)]W(N)}{[1 - W(N)/W(B)]} \tag{5.1}$$

Here, $f_\lambda(N)$ and $f_\lambda(B)$ are the flux densities in the narrow Hα and broad R-band, while W(N) and W(B) are the widths of the narrow Hα and broad R-band filters, respectively.

Filter name	Central wavelength (Å)	Bandwidth (Å)	Telescope	Date of observation	Exposure time (sec)
F148W	1481	50.0	*UVIT*	27/02/2018	1348
F172M	1717	12.5	*UVIT*	27/02/2018	6348
N219M	2196	27.0	*UVIT*	27/02/2018	6386
N263M	2632	27.5	*UVIT*	27/02/2018	1355
656.3(10)	6563	10	*HCT*	22/12/2021	1800
R	6020	1000	*HCT*	22/12/2021	300

Table 5.1 Log of observations

In addition to Hα and R-band data from *HCT*, we used archival *NOT* data in the broad U, B, V, R, and I filters, calibrated photometrically using differential photometry techniques. We also included data in the J, H, and Ks bands from *2MASS*; W1, W2, W3, and W4 bands from *WISE*; and 24, 70, and 160 μm images from *Spitzer*. In radio, we used 1.4 GHz imaging data from *VLA* and 21 cm HI emission line data from *WSRT*. A composite image of NGC 4395 using the R, NUV, and FUV filters, covering the central $10'' \times 10''$, is shown in Figure 5.1.

5.2 Analysis

For analysis, we explicitly used data from all the *UVIT* filters used during observation. To calculate SFR and age, we used F148W and N263M filters as these have relatively larger effective areas (indicative of the overall sensitivity of the photometric system) compared with other filters. However, for the calculation of colour excess, E(B−V), we used one FUV filter (F172M) and one NUV filter (N219M) that are closely spaced in wavelength.

5.2.1 Identification of star-forming regions

To identify star-forming regions in NGC 4395, we used the final combined image taken in F148W. We used *SExtractor* with the following parameters, namely DETECT_THRESH = 5σ, DETECT_MINAREA = 11 and DEBLEND_THRESHOLD = 32, where σ is the background noise. Using the above criteria, we identified a total of 284 star-forming regions after the removal of some overlapping regions. The identified star-forming regions marked on the F148W filter image are shown in left panel of Fig. 5.2. The same criteria were also used to identify star-forming regions in the narrow-band Hα filter. Out of the 284 regions detected in FUV, we could detect 120 regions that have sufficient signal-to-noise ratio in the Hα continuum subtracted image.

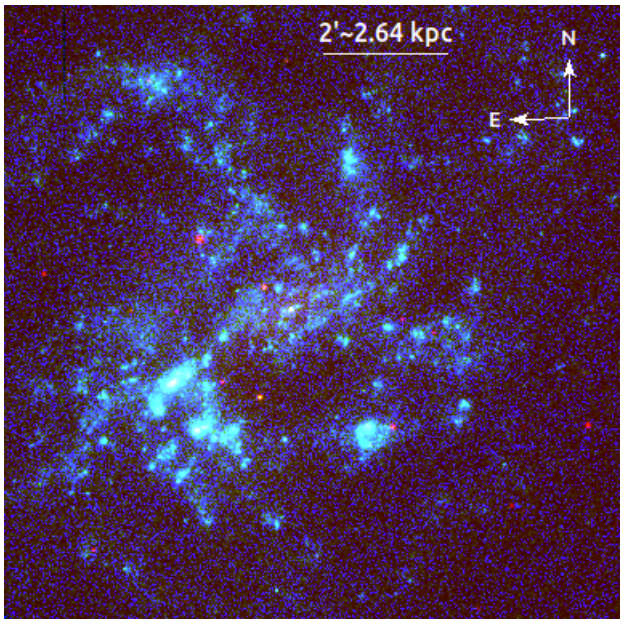

Fig. 5.1 The colour composite image of NGC 4395 covering a region of $10'' \times 10''$. Here, red is the R-band image from *HCT*, green is the NUV image in the N263M filter, and blue is the FUV image in the F148W filter of *UVIT*.

5.2.2 Size of the star-forming regions

After detecting star-forming regions, we checked their sizes. *SExtractor* gives us the semi-major and semi-minor length in pixel coordinate and position angle in degree corresponding to each star-forming region. We converted these to arcsec and then to pc unit. At the redshift z = 0.00106 of NGC 4395, one arcsec corresponds to 22 pc. The measured sizes of the star-forming regions in UV and Hα were corrected for their respective instrumental resolutions by assuming elliptical light distribution within the apertures. We could correct for instrumental resolution for 225 regions out of 284 detected regions in UV and 77 regions out of 120 regions in Hα. For the remaining regions with sizes similar to the instrumental resolution, we considered the apertures given by *SExtractor*. We noticed that the area of the star-forming regions detected in UV varies from 8.6×10^{-4} kpc^2 to 488.1×10^{-4} kpc^2 with a median of 40.2×10^{-4} kpc^2. The distribution of the area of the star-forming regions is shown in the right panel of Fig. 5.2.

5.2.3 Photometry

Once the star-forming regions were identified and the sizes were corrected for instrumental resolution in F148W and Hα using the criteria given in sections 5.2.1 and 5.2.2, we carried out photometry of the regions using the aperture photometry technique in *PhotUtils* (Bradley

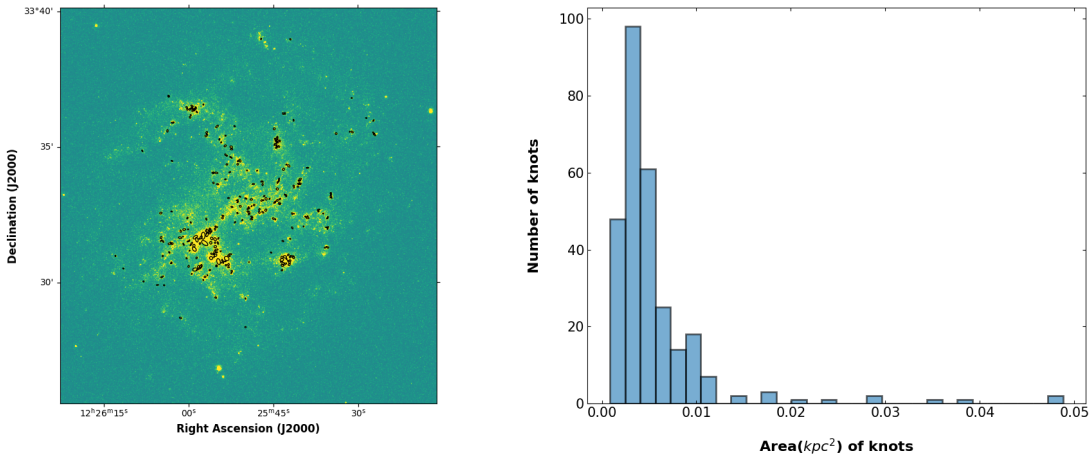

Fig. 5.2 Left panel: The image of NGC 4395 in the UV F148W filter. The regions that have been identified are marked. Right panel: Distribution of the area of the star-forming regions identified in FUV.

et al., 2020). As the images in F148W, F172M, N219M, and N263M were astrometrically aligned, photometry of all 284 regions was also carried out on the images acquired in all four filters. Similarly, photometry was also carried out in the 120 regions identified in the continuum subtracted Hα image. One of the crucial parameters for photometry is the proper subtraction of the background. For the determination of the background, we estimated the median count rate in randomly placed square boxes of sizes 10 $\times$ 10 pixels in 50 source-free regions. The mean of these 50 median values was taken as the background per pixel. This background per pixel was subtracted from each of the pixels in the aperture used for photometry. The background subtracted count rates from each of the identified star-forming regions in F148W, F172M, N219M, and N263M were converted to magnitudes using the calibration given in Tandon et al. (2020). Similarly, for the Hα observations, the derived instrumental magnitudes of the star-forming regions were converted to standard magnitudes using the procedure outlined in Chapter 2. We note that though the aperture used for the photometry of the star-forming regions does not overlap, there could be contamination from adjacent star-forming regions.

5.2.4 Extinction correction

The magnitudes derived for the star-forming regions are affected by both internal and Galactic extinction. To estimate the extinction in UV and Hα for our Galaxy, we used the relation given

below (Cardelli et al., 1989)

$$\langle A(\lambda)/A(V)\rangle = a(x) + b(x)/R_V \tag{5.2}$$

Here, A(V) = 0.047 mag is the Galactic extinction in the V-band taken from NED[1], and x is the wave number. The values of $a(x)$ and $b(x)$ were evaluated following Cardelli et al. (1989). A similar procedure was also followed to correct for Galactic extinction in the Hα image.

Dust present within each of the detected star-forming regions scatters and/or absorbs the UV photons coming from those regions, making it difficult to estimate the absolute flux emitted from those regions. To correct for this in the UV band, we used the method based on the UV spectral slope β that is explained in the Chapter 4.

To correct for internal extinction in Hα, we adopted the following. We calculated β and E(B−V) from F172M and F219M filter images for these 120 regions, following Equations described in Chapter 4. We then evaluated A_λ for Hα with the k'_λ determined as follows (Calzetti et al., 2000)

$$k'(\lambda) = 2.659(-1.857 + 1.040/\lambda) + R'_V \tag{5.3}$$

We obtained a value of $k'(\lambda)$ of 3.329. Using this we derived A_λ for all the 120 star-forming regions in Hα.

5.3 Results

5.3.1 Star formation rate

The SFR provides important information on the assembly of stellar mass. As different populations of stars emit efficiently at different wavelengths, one needs to probe the star-forming regions in different bands. In particular, UV traces the emission from young high-mass stars of O, B type (Davies et al., 2016), thereby providing the best estimates of recent star formation over 100 Myr. Similarly, Hα traces star formation of < 10 Myr (Kennicutt, 1998; Kennicutt & Evans, 2012; Calzetti, 2013a). Nearly half of the star-forming regions identified in UV have also been detected in our observations in Hα. We estimated the SFR in UV using the F148W filter using the following relation (Salim et al., 2007).

$$log(SFR_{FUV}(M_\odot yr^{-1})) = log[L_{FUV}(WHz^{-1})] - 21.16 \tag{5.4}$$

[1] http://ned.ipac.caltech.edu

This relation (Equation 5.4) traces 0.1 $M_\odot$ to 100 $M_\odot$ stellar population having Chabrier initial mass function (IMF). We derived SFR in Hα following the Kennicutt (1998) relation

$$SFR(M_\odot yr^{-1}) = 7.9 \times 10^{-42} L_{H\alpha}(erg.s^{-1}) \tag{5.5}$$

Here, L_{FUV} is the intrinsic luminosity of the star-forming regions in FUV and $L_{H\alpha}$ is the luminosity of the star-forming regions in Hα. The distributions of SFR surface density ($\Sigma_{SFR} = SFR/Area$) and their variation across the galaxy in F148W and Hα are given in Fig. 5.3. The SFR calculated in the FUV filter spans a wide range from 2.0×10^{-5} $M_\odot yr^{-1}$ to 1.5×10^{-2} $M_\odot yr^{-1}$ with a median value of 3.0×10^{-4} $M_\odot yr^{-1}$. In Hα we found the SFR to range from 7.2×10^{-6} $M_\odot yr^{-1}$ to 2.7×10^{-2} $M_\odot yr^{-1}$ with a median value of 1.7×10^{-4} $M_\odot yr^{-1}$. The Σ_{SFR} of the central $100'' \times 100''$ region in F148W filter is shown in Fig. 5.4.

5.3.2 Age of the star-forming regions

We calculated the age of the star-forming regions using both UV colour (F148W − N263M) and Hα equivalent width.

5.3.2.1 UV colour

To determine the age of the star-forming regions, we used the simple stellar evolutionary population model *starburst99* (Leitherer et al., 1999). We generated synthetic stellar spectra using *starburst99*, by adopting Kroupa IMF, total stellar mass of $10^9 M_\odot$, solar metallicity and ages up to 100 Myr. We convolved the generated UV spectra with the effective area of the respective *UVIT* filters to get the fluxes in the corresponding *UVIT* filters as

$$F^{cal}(\lambda) = \frac{\int F(\lambda) EA(\lambda) d\lambda}{\int EA(\lambda) d\lambda} \tag{5.6}$$

Here, EA(λ) is the effective area of the filters. $F^{cal}(\lambda)$ is the simulated fluxes, which were then converted to AB magnitudes using the zero points given in Tandon et al. (2020). These were then used to generate the theoretical colours. The plot of the age against the theoretical colour is given in Fig. 5.5. The observed FUV − NUV colours of the star-forming regions were compared with the theoretical colours to get the ages of the star-forming regions. The distribution of the ages of the star-forming regions obtained from UV colour, as well as its spatial variation in NGC 4395, are shown in the top panel of Fig. 5.6.

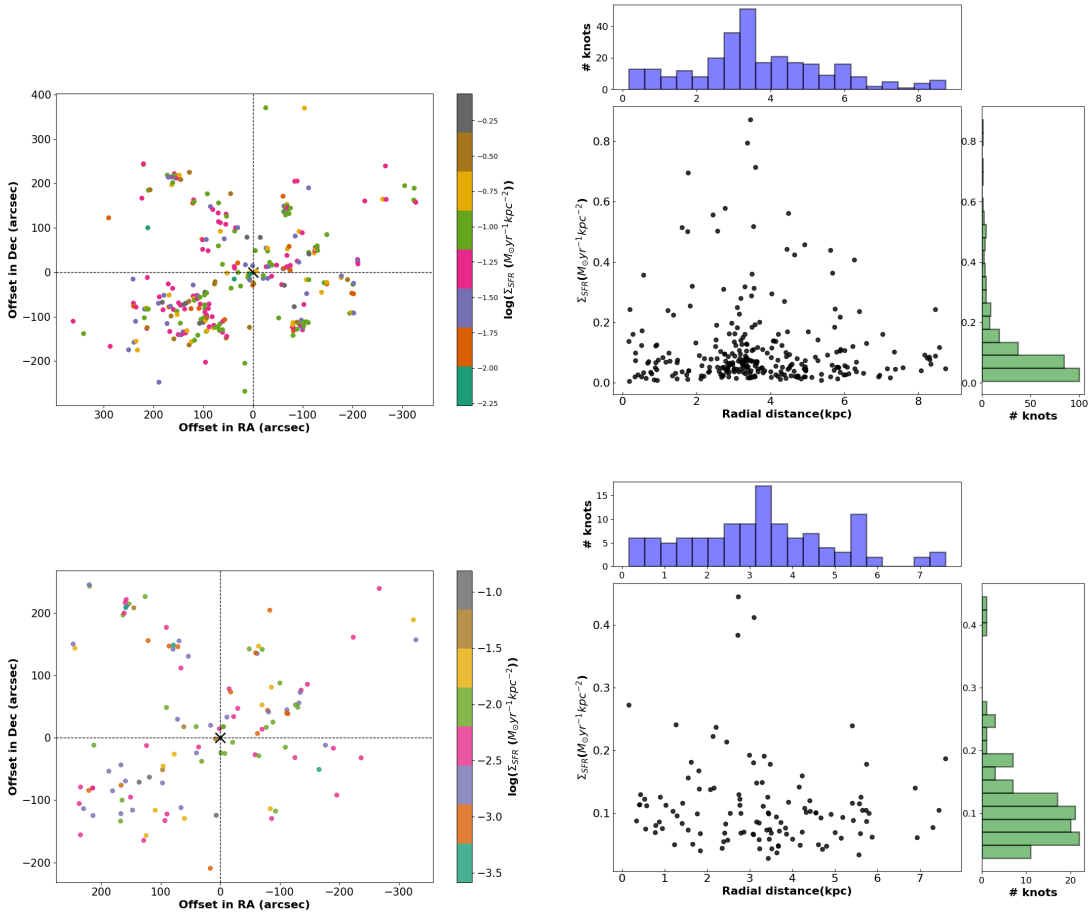

Fig. 5.3 Distribution of Σ_{SFR} and its spatial variation in F148W (top panel) and Hα (bottom panel). Here, the central AGN is marked as a cross in the left panels.

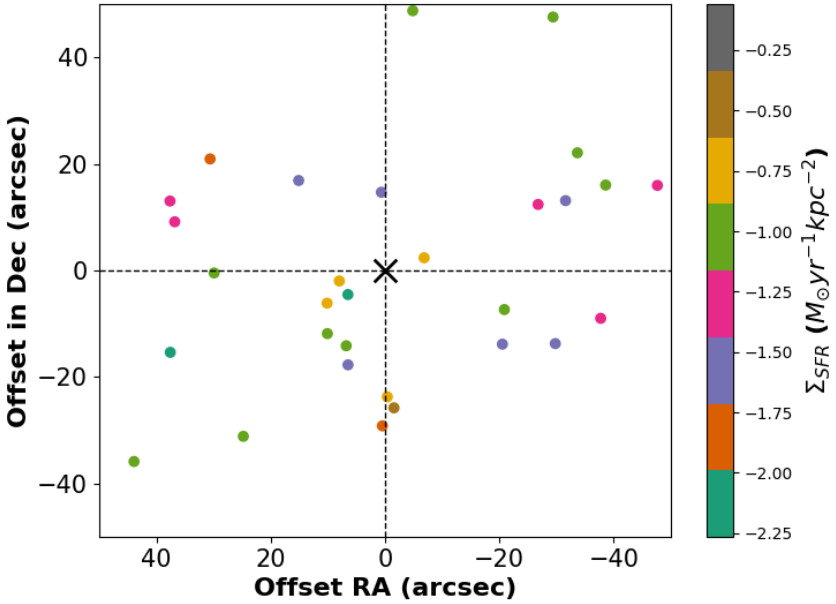

Fig. 5.4 The variation of Σ_{SFR} in the central $100'' \times 100''$ region in UV. The central AGN is marked as a cross in the figure.

5.3.2.2 Hα equivalent width

For the observations carried out in Hα, we determined the age of the star-forming regions using Hα equivalent width. Here, too, we used the *starburst99* model (Leitherer et al., 1999) using the same input parameters as explained in Section 5.3.2.1. *starburst99* generates the expected equivalent width for different stellar populations at different time scales. We calculated the equivalent width from the calibrated Hα narrow-band and nearest broad R-band continuum images using the following relation (Waller, 1990)

$$EW_{line} = \frac{[f_\lambda(N) - f_\lambda(B)]W(N)}{f_\lambda(B) - [f_\lambda(N)W(N)/W(B)]} \tag{5.7}$$

Here, $f_\lambda(N)$ and $f_\lambda(B)$ are the flux densities measured in the narrow-band Hα and broad R-band filters. Similarly, W(N) and W(B) are the bandwidths of narrow-band Hα and broad R-band filters. The distribution of age determined from Hα observations is shown in the bottom panel of Fig. 5.6.

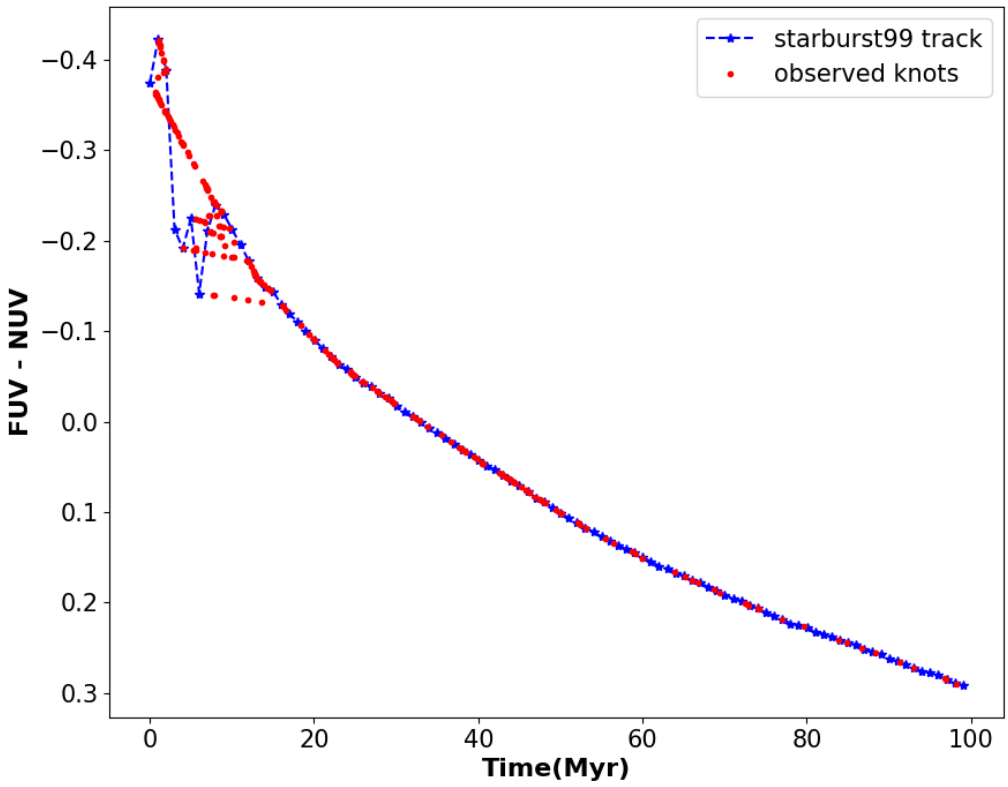

Fig. 5.5 Extinction corrected observed (FUV − NUV) color (red circles) against age. The blue dashed line is the synthetic track derived from *starburst99* model.

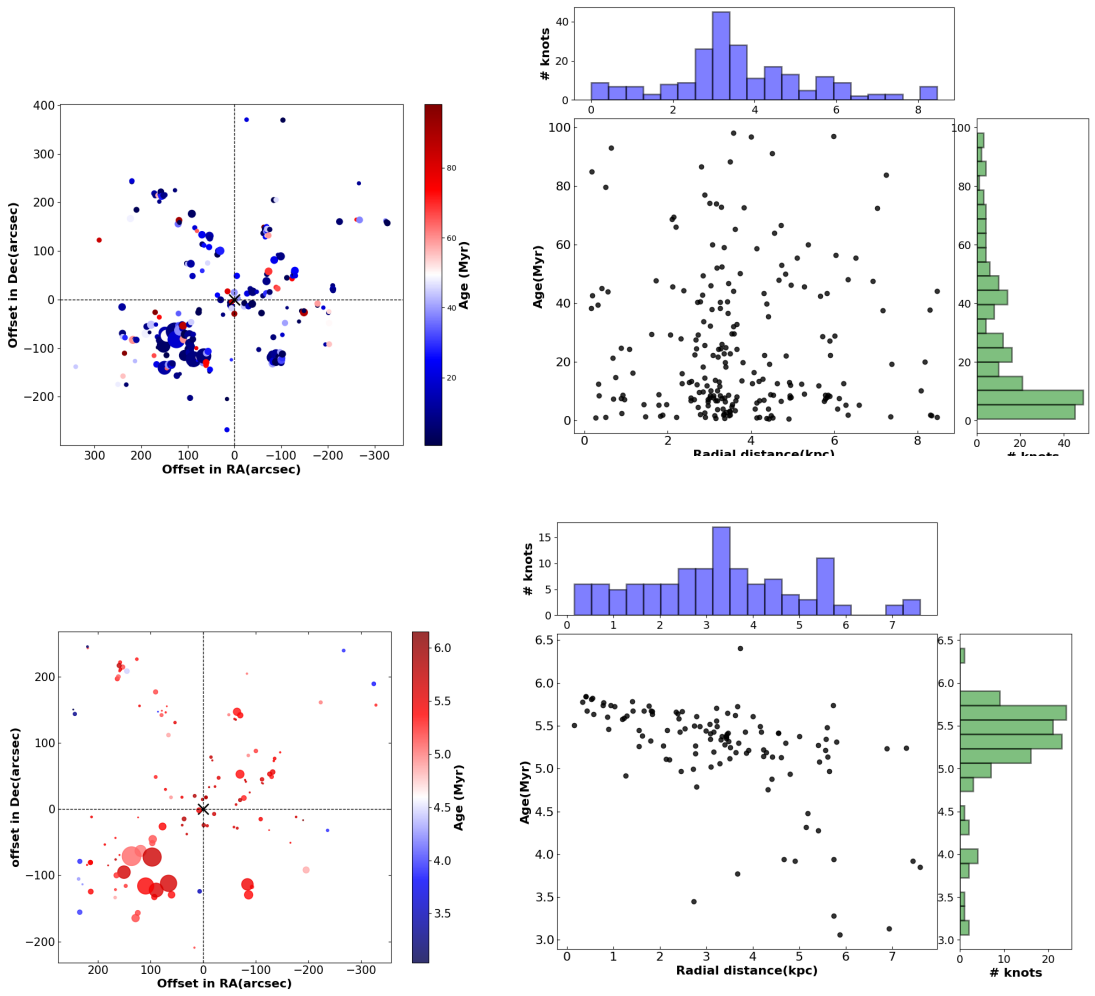

Fig. 5.6 Distribution of age of the star-forming regions and its spatial variation in F148W (top panel) and Hα (bottom panel). In the left panels, different sizes of the points correspond to the size of the star-forming regions, and the cross is the position of the central AGN.

5.3.3 Radial dependence of SFR and age

The spatial distribution of the star-forming regions of varying ages can provide information on the impact of the local environment and the central AGN can have on the star formation characteristics of NGC 4395. To check for any such variation, we calculated the distance (R) and the deprojected distance (R′) of the star-forming regions from the central AGN. The distance R′ is calculated as

$$R' = \frac{R}{\sqrt{(cos^2(\theta) + sin^2(\theta)cos^2(i))}} \tag{5.8}$$

where θ is given as

$$\theta = cos^{-1}\frac{\delta DEC}{\sqrt{\delta RA^2 + \delta DEC^2}} \tag{5.9}$$

here, R is the observed distance from the centre of NGC 4395, i is the inclination of the galaxy and θ is the angle between the major axis of the galaxy and the radial distance to the star-forming regions (Martin, 1995; Gadotti et al., 2007). The variation of the age of the star-forming regions obtained from UV colour, as a function of R' is shown in Fig. 5.6. The distribution is random with no indication of variation of the age of the star-forming regions with distance as shown in the top panel of Fig. 5.6. In the bottom panel of Fig. 5.6 is the variation of the age of the star-forming regions obtained from Hα as a function of galactocentric distance. There is a trend of young star-forming regions occupying regions with increasing distances from the central AGN. However, such a behaviour is not seen in UV. This different trend seen in the age versus radial distance in Hα and UV could be due to the different stellar populations probed by the integrated UV and Hα emission. Any age gradients that might be in place during the short time scales (as probed by Hα) are possibly obliterated on the time scales probed by UV (likely due to radial migration, etc.). The complete catalogue of the star-forming regions identified in UV can be found in Nandi et al. (2023a).

5.3.4 SFR at multiple wavelengths

The SFR of the star-forming regions identified in NGC 4395 were estimated using observations carried out in the UV and Hα bands, taking into account the differences in the instrumental resolutions in UV and Hα. There are different calibration relations available in the literature (Kennicutt, 1998; Salim et al., 2007; Brown et al., 2017) that pertain to observations at different wavelengths. It would be ideal for getting the SFR of the star-forming regions identified in F148W and Hα at other wavelengths so that a comparison of the SFR estimates from different

wavelengths could be made. But, for the regions identified in F148W and Hα it is not possible to get the SFR at other longer wavelengths because of poorer resolution at longer wavelengths.

An approach to compare the SFR estimated at different wavelengths is to identify star-forming regions in images of different wavelengths at similar resolution. To achieve this, we used the image in 24 μm from *Spitzer MIPS* and smoothed the images of NGC 4395 acquired at other wavelengths such as the UV and optical bands to the spatial resolution of 24 μm image. This was done using the task *HGEOM* in the *AIPS* software (Wells, 1985). We then identified star-forming regions in the 24 μm image using the same procedure outlined in Section 5.2.1. We identified a total of 14 star-forming regions. We show in Fig. 5.7 the composite image of NGC 4395 with the identified 14 regions marked by black ellipses on it. For these 14 star-forming regions, we calculated the SFR in FUV, NUV, $H\alpha$, and 24 μm. For UV and Hα, we used the calibration relations given in Equations 5.4 and 5.5, while for 24 μm we used the following calibration relation (Brown et al., 2017).

$$log(SFR_{24\mu m}) = [log[L_{24\mu m}(erg.s^{-1})] - 40.93]/1.3 - 1.26 \tag{5.10}$$

The results obtained from different wavelengths for these 14 star-forming regions are given in Table 5.2. The values of SFR were estimated from the smoothed images so that they have similar resolutions. Therefore, there will not be any effect of resolution on the estimated SFR (given in Table 5.2) for different filters. Out of these 14 detected star-forming regions in IR, six star-forming regions (3rd, 6th, 7th, 8th, 9th, and 10th star-forming regions in Table 5.2) have higher SFR in all wavelengths. In Fig. 5.7, we marked three star-forming complexes (A, B, and C) by white ellipses containing 3, 2, and 1 star-forming regions, respectively detected based on 24 μm band. These three star-forming complexes are known to be associated with SN remnants (Vukotic et al., 2005; Leonidaki et al., 2013). Using an aperture of $45'' \times 45''$ centred around the complexes A, B, and C, we calculated the number density of resolved star-forming regions detected in the high-resolution UV image from *UVIT-AstroSat* and compared it with nearby $45'' \times 45''$ SN -free regions. In regions centred around the complexes A, B, and C, the average number density of star-forming regions is 1.7×10^{-5} pc^{-2} whereas in the regions devoid of any known SN, it is 0.7×10^{-5} pc^{-2}. The enhanced flux density and higher number of resolved star-forming regions in these three complexes (A, B, and C) could be thus attributed to positive feedback effects from SN. As shown in Fig. 5.7, the star-forming regions associated with A, B, and C have strong HI gas components, and also other star-forming regions (13th in Table 5.2) marked as D has strong HI emission based on the images from the *WSRT* (Heald & Oosterloo, 2008).

No	RA	DEC	a	b	PA	SFR(10^{-3} $M_\odot$ yr^{-1})			
	(deg)	(deg)	arcsec	arcsec	(deg)	FUV	NUV	Hα	24 μm
1	186.488535	33.502065	6.06	4.24	57.5	0.152 ± 0.003	0.140 ± 0.002	0.717 ± 0.002	1.446 ± 0.333
2	186.455487	33.512476	4.37	4.09	-14.7	0.070 ± 0.002	0.063 ± 0.001	0.999 ± 0.002	1.677 ± 0.359
3	186.429978	33.515758	5.53	5.16	88.3	0.672 ± 0.014	0.646 ± 0.007	1.894 ± 0.003	1.182 ± 0.301
4	186.517630	33.520106	4.16	3.10	-2.6	0.023 ± 0.001	0.024 ± 0.001	0.070 ± 0.001	0.826 ± 0.252
5	186.515393	33.523667	5.97	3.67	42.76	0.071 ± 0.002	0.070 ± 0.001	0.179 ± 0.001	0.367 ± 0.168
6	186.491412	33.527326	9.88	7.319	52.35	2.9 ± 0.059	2.789 ± 0.031	13.493 ± 0.008	10.695 ± 0.906
7	186.486431	33.529412	4.51	3.76	-89.7	0.359 ± 0.008	0.362 ± 0.004	3.107 ± 0.004	2.532 ± 0.441
8	186.480444	33.533089	15.74	7.71	56.1	0.664 ± 0.014	0.689 ± 0.008	3.373 ± 0.004	3.757 ± 0.537
9	186.470888	33.510386	8.42	5.99	71.9	0.296 ± 0.006	0.303 ± 0.003	1.643 ± 0.003	1.728 ± 0.364
10	186.481081	33.514092	23.10	17.29	-30.1	4.178 ± 0.044	4.178 ± 0.044	12.080 ± 0.007	6.421 ± 0.702
11	186.433656	33.561573	5.94	4.02	-66.94	0.135 ± 0.003	0.128 ± 0.002	1.064 ± 0.002	0.934 ± 0.268
12	186.435697	33.587645	5.15	4.65	-37.0	0.297 ± 0.006	0.270 ± 0.003	1.021 ± 0.002	0.909 ± 0.264
13	186.495866	33.605167	6.37	5.72	64.5	0.206 ± 0.004	0.202 ± 0.002	0.862 ± 0.002	1.047 ± 0.283
14	186.354740	33.614038	3.97	3.53	6.4	0.125 ± 0.002	0.170 ± 0.002	0.006 ± 0.001	1.510 ± 0.340

Table 5.2 The SFR in multiple wavelengths determined for the 14 star-forming regions identified in the *MIPS* 24 μm image. Here, a and b are, respectively, the semi-major and semi-minor axes of the star-forming regions, while PA is the position angle.

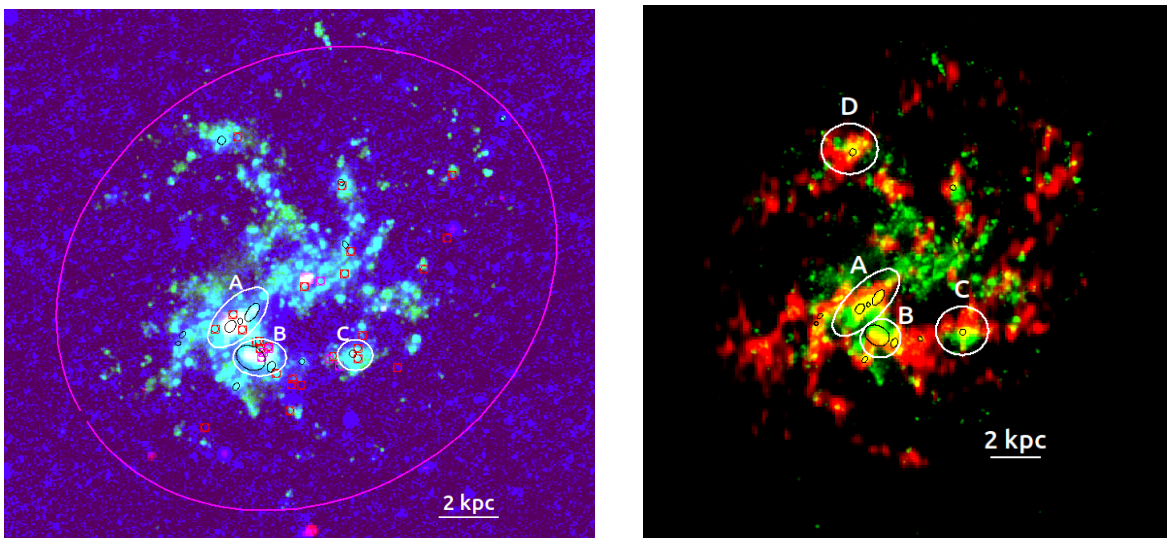

Fig. 5.7 Left panel: Composite image of NGC 4395 in 1.4 GHz continuum (red), *GALEX* FUV (green), and 24 μm *MIPS* (blue). The identified star-forming regions based on the 24 μm image are overlaid on the image by black ellipses. The white ellipses marked by A, B, and C are the detected star-forming regions having counterparts in 1.4 GHz. The big magenta ellipse is the aperture equivalent to the R25 parameter in the optical U-band. The small red boxes are the positions of SN remnants (Leonidaki et al., 2013). Right Panel: Composite image of NGC 4395 in HI line image (Heald & Oosterloo, 2008) (red) and *GALEX* FUV (green). Black ellipses are the identified regions from 24 μm *MIPS* image. The white ellipses marked by A, B, C, and D are the star-forming complexes with strong UV and HI emissions.

5.3.5 Global star formation rate

In the earlier sections, we derived the SFR as well as the ages for many star-forming regions identified in NGC 4395 utilizing scaling relations. Here, we aim to characterise the global star-forming nature of NGC 4395. For this, we decided to use two approaches (a) the existing calibrations, and (b) broad-band spectral energy distribution (SED) modelling. Broad-band SED modelling requires the brightness of the source to be evaluated at multiple wavelengths. For this, we chose an aperture radius in the optical U-band such that the surface brightness drops to 25 mag/arcsec^2. The same aperture was then used to estimate the brightness of NGC 4395 in different wavelengths, such as the *GALEX* FUV, NUV, optical U, B, V, R, I from *NOT*, *2MASS* J, H, and Ks, *WISE* W1, W2, W3, and *MIPS* 24 μm, 70 μm, and 160 μm bands. A colour composite of NGC 4395 in UV, IR, and radio, with the aperture marked on it is given in Fig. 5.7. The observed brightness of NGC 4395 at 16 different wavelengths was used to generate the broad-band SED and then modelled using *CIGALE (Code Investigating GALaxy Emission*; Boquien et al. 2019) to derive different physical properties of NGC 4395.

We used *CIGALE* version 2022.0[2]. This code works on the principle of energy balance and uses the Bayesian analysis method to derive various model parameters. To build the model, we used the delayed star formation history with an optional constant burst/quench module and having the form $SFR(t) \propto t \times exp(-t/\tau)$ for $0 < t < t_0$. Here, t_0 is the age of the onset of star formation and τ is the time at which the SFR peaks. To model the stellar emission, we used the Bruzual & Charlot (2003) single stellar population template with Salpeter IMF. We used the Charlot & Fall (2000) model to take care of dust attenuation. The IR part of the SED because of dust heated by stars was taken into account by the use of Draine et al. (2014, 2007) model and the presence of AGN was considered with the inclusion of SKIRTOR templates (Stalevski et al., 2016). The list of modules and the parameters used to build the SED of NGC 4395 are given in Table 5.3. The observed SED, along with the model fit, is given in Fig. 5.8. Some of the derived parameters from fits to the SED are given in Table 5.4. We also derived the global SFR in FUV, NUV, Hα, 24 μm, and 1.4 GHz using the scaling relations given in Equations 5.4,5.5, 5.10, and 5.11 (Murphy et al., 2011).

$$log(SFR_{1.4GHz}) = log(L_{1.4}(erg.s^{-1}.Hz^{-1})) - 28.20 \tag{5.11}$$

It is found that while the SFR obtained in FUV, NUV, Hα, 1.4 GHz and SED fitting are nearly in agreement with each other as well as reported by Lee et al. (2009), the SFR obtained in 24 μm is lower. A summary of these results is given in Table 5.5. As can be seen in Table 5.5, the SFR of about 0.5 $M_\odot yr^{-1}$ found from few tracers are in agreement with each other. However,

[2]https://cigale.lam.fr

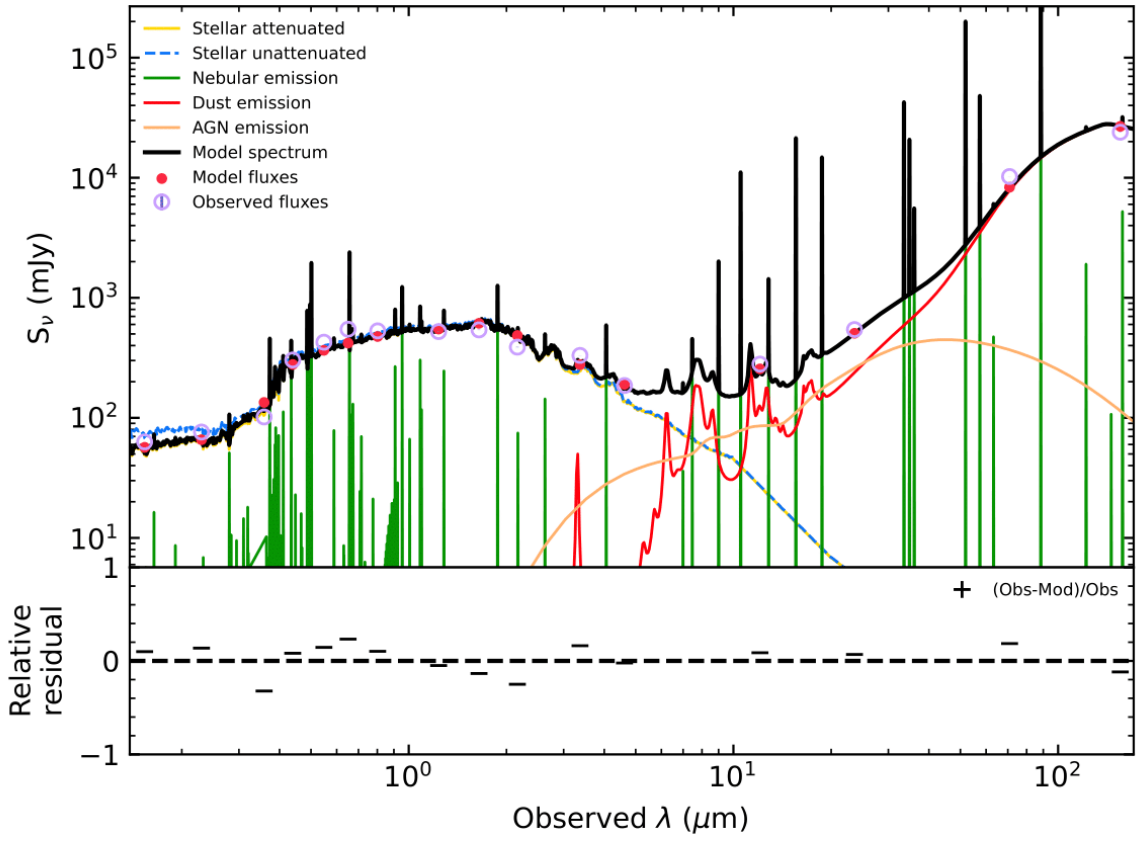

Fig. 5.8 SED fitting using *CIGALE* code for the whole galaxy.

from 24 μm IR emission, we obtained a SFR of 0.05 $M_\odot yr^{-1}$, which is in agreement with the value of the SFR of 0.03 $M_\odot yr^{-1}$ found by Smirnova et al. (2020). This value is lower than that found from other tracers such as FUV, NUV, Hα and 1.4 GHz. The lower SFR at 24 μm is due to lower intrinsic luminosity at 24 μm than the predicted flux (predicted 24 μm luminosity $\sim$ 10 times the observed 24 μm luminosity) from Hα luminosity by Kennicutt et al. (2009) for star-forming galaxies. The SFR calculated from the predicted luminosity at 24 μm is similar to that obtained from other tracers.

5.4 Discussion

Recent theoretical studies point to AGN feedback operating in dwarf galaxies (Koudmani et al., 2022), which is also supported by observations (Penny et al., 2018). We carried out a multi-wavelength investigation on the star formation characteristics of the dwarf AGN NGC 4395 to understand star formation and the effect of AGN on the ISM of the host galaxy. Within 15 arcsecs from the centre of NGC 4395, we noticed three star-forming regions having high SFR

Parameter	Value
Star Formation History (sfhdelayedbq)	
e-folding time of the main stellar population	200.0, 500.0, 700.0, 1000.0, 2000.0, 3000.0, 4000.0, 5000.0 Myr
Age of main stellar population	1500, 2000 Myr
Age of the late burst/quench episode	500 Myr
Ratio of the SFR after/before burst/quench	0.0,0.1,0.2,0.4,0.7,1.0,5.0,10.0,100.0
instance without any burst	1.0
Stellar population synthesis (bc03)	
Initial mass fraction	Salpeter
Metalicity	0.008,0.02, 0.05
Separation between the young and the old stellar population	10 Myr
Nebular emission (nebular)	
Ionisation parameter	-2.0
Electron density	100 cm^{-3}
Dust attenuation (dustatt_modified_CF00)	
V-band attenuation in the interstellar medium	0.05,0.10,0.15,0.2,0.5
AV_ISM / (Av_BC + Av_ISM)	0.50
Power law slope of the attenuation in the ISM	-0.7
Power law slope of the attenuation in the birth clouds	-0.7
Filters for which the attenuation will be computed and added	FUV and NUV
Dust emission (dl2014)	
Mass fraction of PAH	1.12,2.5,3.19,5.26
Minimum radiation field	1.0,10,15,25
Power law slope	1.5, 2.0
Fraction illuminated from Umin to Umax	0.001,0.01,0.1,0.5
AGN module (skirtor2016)	
Average edge-on optical depth at 9.7 micron	3, 7
power law exponent that sets radial gradient with polar angle	1.0
index that sets dust density gradient with polar angle	1.0
inclination, i.e. viewing angle, position of the instrument w.r.t. the AGN axis	30, 70
Disk spectrum	Skirtor spectrum
AGN fraction	0.0, 0.05, 0.1, 0.2, 0.3, 0.4
Wavelength range in microns used to compute the AGN fraction	0/0
Extinction law of the polar dust	SMC
E(B−V) for the extinction in the polar direction in magnitudes	0.0, 0.03, 0.2, 0.4
Temperature of the polar dust	100.0 K
Emissivity index of the polar dust	1.6

Table 5.3 Input parameters for SED fitting with *CIGALE*

Parameter	Value
Stellar mass($M_\odot$)	1.01×10^9
SFR($M_\odot yr^{-1}$)	0.21 ± 0.02
$SFR_{100Myrs}$($M_\odot yr^{-1}$)	0.21 ± 0.02
SFR_{10Myrs}($M_\odot yr^{-1}$)	0.21 ± 0.02
Attenuation(Av_ISM)	0.1
AGN fraction	0.1

Table 5.4 Parameters derived from broad-band SED analysis

Tracer	SFR ($M_\odot yr^{-1}$)
FUV	0.47 ± 0.00
NUV	0.55 ± 0.00
Hα	0.32 ± 0.00
24 μm	0.05
1.4 GHz	0.52
SED	0.21 ± 0.02

Table 5.5 Summary of SFR obtained at different wavelengths. A value of 0.0 in the error of SFR means that the value is lesser than 1×10^{-3}.

in UV. The high star formation in these regions in close proximity to the AGN could be because of positive feedback from AGN. From SED model fits, we obtained an AGN fraction around 0.1 (see Table 5.4), which also points to the contribution of AGN to the observed properties. Alternatively, such enhanced star formation close to the centre of the AGN can happen if gas can be funnelled into the centre of the galaxy by the presence of bar and/or tidal interaction. However, in the case of NGC 4395, we do not have evidence of bar or tidal interaction. Using the stellar mass as returned by our *CIGALE* modelling of the galaxy and SFR obtained from FUV, we calculated the specific SFR (sSFR = SFR per unit mass). We found a value of sSFR = 4.64×10^{-10} yr^{-1}. This is larger than that of M33 (sSFR= 1.13×10^{-10} yr^{-1}; Verley et al. 2009; Corbelli 2003) and LMC (sSFR = 7.41×10^{-11} yr^{-1}; Harris & Zaritsky 2009; van der Marel et al. 2002). These galaxies have stellar masses ($M_*|_{M33} = 4 \times 10^9$ M$_\odot$; Corbelli 2003 and $M_*|_{LMC}= 2.7 \times 10^9$ M$_\odot$; van der Marel et al. 2002) similar to that of NGC 4395. We noticed a gradual decrease in the age of the star-forming regions in Hα from the centre towards the outer regions; however, this is not seen in the star-forming regions identified from UV.

At 1.4 GHz, we identified three star-forming complexes with enhanced radio emission marked as A, B, and C in Fig. 5.7. These star-forming complexes encompass a few resolved star-forming regions seen in IR and UV showing higher SFR. Also, the number density of resolved star-forming regions identified in high-resolution UV is higher in these regions than in the surroundings. Massive stars in these star-forming regions can affect the ISM through stellar winds and SN explosions. SN explosions could have an impact on the ISM which could be either positive feedback via enhancement of star formation (Hensler, 2014) or negative feedback via inhibition of star formation (Gelli et al., 2023), however, the details are highly uncertain.

All the three star-forming complexes namely A, B, and C are known to be associated with SN remnants (Vukotic et al., 2005; Leonidaki et al., 2013). The high SFR and high number density of star-forming regions seen in star-forming complexes A, B, and C could be due to positive feedback effects from SN. Alternatively, one would also expect higher SN rates in areas of high star formation due to stellar feedback processes. However, we found many regions that have a supernova remnant without any associated bright star-forming regions (see Fig. 5.7). It is probable that the high SFR seen in the star-forming complexes A, B and C is due to positive feedback from SN. However, we note here that, just by the spatial coincidence of SN and massive star-forming regions vis-a-vis isolated SN not spatially coinciding with star-forming regions, it is difficult to conclude that SN explosions could have caused the high SFR via positive feedback. This is because stars are known to migrate from their birthplaces, which is also supported theoretically (Minchev et al., 2018). Therefore, one needs to account for the effects of radial migration before any conclusive claims on SN-induced positive feedback

effects can be made. However, the star-forming regions in Complex A (regions 6,7 and 8 in Table 5.2), complex B (regions 9,10 in Table 5.2), and complex C (region 3 in Table 5.2) have higher SFR in Hα and 24 μm (see Table 5.2) compared to other star-forming regions, which could be due to the compression of ISM during SN explosions, arguing for SN induced star formation, as in the case of NGC 2770 (Michałowski et al., 2020).

We found that cold neutral gas (HI) is extended throughout the spiral arms of the galaxy. However, there is no one-to-one correspondence between the star-forming regions traced by UV and HI, although the peaks of HI emission (Heald & Oosterloo, 2008) are associated with regions of high star formation and strong UV flux. To have a more detailed understanding of the relationship between UV and HI emission, HI observations with spatial resolution comparable to UV are needed. Systematic investigation of the star formation characteristics of a large sample of dwarf galaxies is needed to enhance our understanding of the complex feedback processes (supernova and/or AGN) operating in dwarf galaxies.

5.5 Summary

In this work, we carried out UV and Hα observations to study the spatially resolved star-forming regions of the host of the dwarf AGN, NGC 4395. In addition to the new observations in UV and Hα, we also used archival data in UV, IR, and radio wavelengths. We also studied the global star formation properties of NGC 4395 using UV, optical, IR, and radio data. The results of this work are summarized below.

1. Using UV data acquired from *UVIT* onboard *AstroSat*, we identified a total of 284 star-forming regions from the F148W image, extending up to a distance of 9 kpc.

2. Of the 284 star-forming regions identified in UV, 120 star-forming regions were also identified in the Hα continuum subtracted image. The detection of fewer star-forming regions in Hα is attributed to the lower spatial resolution as well as the shallowness of the Hα image relative to the UV one.

3. We found the SFR in F148W to lie between 2.0 $\times 10^{-5}$ $M_{\odot} yr^{-1}$ and 1.5 $\times 10^{-2}$ $M_{\odot} yr^{-1}$ with a median value of 3.0 $\times 10^{-4}$ $M_{\odot} yr^{-1}$. Using UV observations, we found the age of star-forming regions to vary between 1 Myr and 98 Myr, with a median value of 14 Myr.

4. In Hα we found a median SFR of 1.7$\times 10^{-4}$ $M_{\odot} yr^{-1}$ with values between 7.2$\times 10^{-6}$ $M_{\odot} yr^{-1}$ and 2.7 $\times 10^{-2}$ $M_{\odot} yr^{-1}$. For the star-forming regions in Hα, we found a median age of 5 Myr with values ranging from 3 Myr to 6 Myr.

5. We did not find any noticeable gradual variation in the ages or Σ_{SFR} of the star-forming regions from the centre to the outer regions of the galaxy in UV.

6. For the ages of the star-forming regions determined from Hα equivalent width, we found an indication of a gradual decrease in their age from the centre of the source outwards. This might be attributed to the intense star-forming regions seen in Hα in the spiral arms of NGC 4395.

7. On inspection of the spatial distribution of Σ_{SFR} in UV (see Fig. 5.4), we found three star-forming regions near the AGN having high Σ_{SFR}. One out of the three star-forming regions in UV is also found to have high Σ_{SFR} in Hα (lower left of Fig. 5.3) and a younger age (lower left of Fig. 5.6). This could possibly hint at positive feedback from AGN. However, we need to make further observations to confirm this.

8. We identified 14 common star-forming regions in UV to IR bands. Out of these 14, 7 star-forming knots have associated HI emission.

9. We found the global SFR of about 0.5 $M_{\odot}yr^{-1}$ in UV. This is consistent with the SFR determined from other tracers such as the Hα and the 1.4 GHz radio continuum. We also calculated the sSFR of 4.64 $\times$ 10^{-10} yr^{-1} in NGC 4395, which is larger than the sSFR of other dwarf galaxies such as M33 and LMC that have stellar masses similar to NGC 4395.

10. At 1.4 GHz, we found a few complexes having enhanced radio emission. These complexes contain a larger number of star-forming regions, with the majority of them having higher SFR. These complexes are known to host supernova remnants. The star-forming regions in these complexes have higher SFR in Hα and 24 μm compared to other star-forming regions, arguing for supernova-induced star formation.

6

Direct evidence of Jet−ISM interaction

AGN can impact the ISM of their hosts via energetic outflows. These outflows, driven by radiation pressure, jets, or winds from AGN, can occur from accretion disk to galaxy scales (Mukherjee et al., 2018; Morganti et al., 2021). Available observations of AGN have usually identified the impact of jets on the ISM on kpc or larger scales. To have a clear understanding of the effect of jets on the ISM, one needs to study their impact from sub-pc to kpc and larger scales. There is hardly any observational evidence of jet−ISM interaction and its impact on the host galaxies of AGN on pc scales. Towards this, in this work, we investigated the effect of jet−ISM interaction in the nearby dwarf AGN, NGC 4395.

NGC 4395 hosts a radio-quiet AGN (Filippenko & Sargent, 1989). It appeared unresolved in the *VLA* A-configuration image at 1.4 GHz with a flux density of 1.68 mJy (Ho & Ulvestad, 2001). Adopting a cosmology of $H_0 = 70$ km s^{-1} Mpc^{-1}, $\Omega_M = 0.7$, $\Omega_{vac} = 0.3$ and a distance of 4.3±0.3 Mpc (Thim et al., 2004), $1''$ in NGC 4395 corresponds to 21 pc.

This Chapter is based on Nandi et al. (2023b)

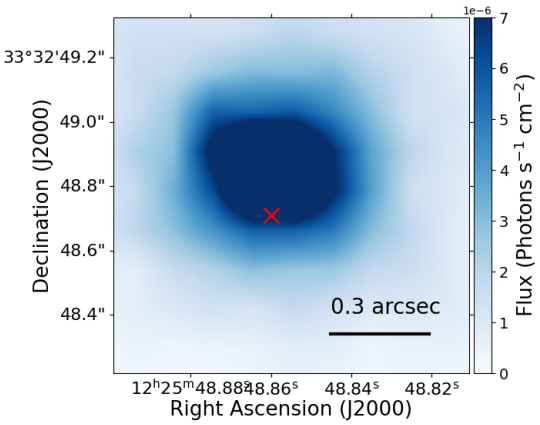

Fig. 6.1 X-ray Image of NGC 4395 in the 0.5−7 keV energy range from *Chandra*. The red cross is the optical *Gaia* position.

Telescope	Filter/Wavelength/Energy	FoV	Resolution/Synthesised Beam size	Exposure time
Chandra	0.5−7.0 keV	$\sim 8'$	$\sim 1''$	79ks
HST	F507N (λ_{eff}=5009.7 Å, $\Delta\lambda$=66.8 Å)	$\sim 2.7'$	$\sim 0.1''$	1521s
	F547M (λ_{eff}=5435.8 Å, $\Delta\lambda$=717.0 Å)	$\sim 2.7'$	$\sim 0.1''$	746s
MaNGA	3600 Å−10000 Å	$\sim 30''\times 30''$	$\sim 1.5''$	5400s
GMOS	4500 Å−7300 Å	$\sim 5.0''\times 3.5''$	$\sim 0.5''$	2880s
NIFS	2.2 μm	$\sim 3.4''\times 3.4''$	$\sim 0.2''$	5400s
VLA	5 GHz	$\sim 8'$	$1.75''\times 1.19''$, 89 deg	1090s
	15 GHz	$\sim 3'$	$0.129''\times 0.124''$, −18 deg	239s
ALMA	237 GHz, CO(2−1)	$\sim 19''$	$1.94''\times 1.25''$, 3 deg	2037s
	237 GHz, CO(2−1)	$\sim 19''$	$0.81''\times 0.47''$, 356 deg	423s

Table 6.1 Details of the data used in this work.

6.1 Observation and data analysis

To characterise the jet−ISM interaction on the scale of pc, we utilised data from both ground and space-based telescopes from low-energy radio waves to high-energy X-rays. The details of the data sets used are given in Table 6.1.

6.1.1 X-ray

In X-ray, we used four epochs of observations with OBSID: 402, 882, 5301, 5302, carried out by the *Chandra* X-ray observatory with *ACIS* for exposures ranging from ∼1 ks to ∼31 ks. The details of the reduction are described in Chapter 2, and the X-ray image in the 0.5−7 keV is shown in Fig. 6.1.

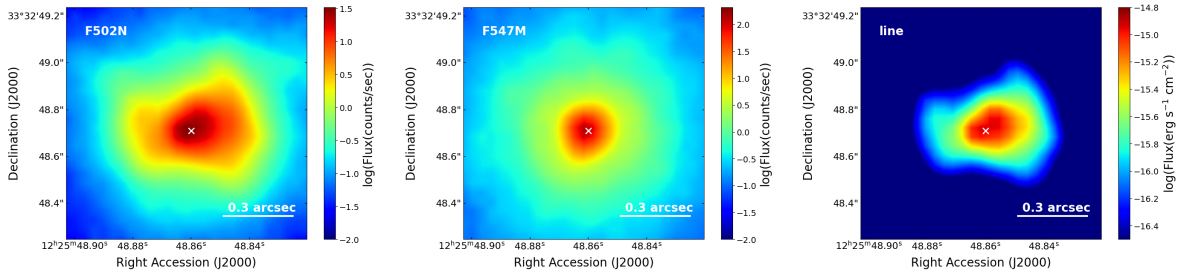

Fig. 6.2 Left panel: The narrow-band image from *HST* in the F502N filter that contains the emission from both the ionised [O III]λ5007 gas and the continuum. Middle panel: The continuum image from *HST* in the F547M filter. Right panel: Difference image after subtraction of the scaled continuum F547M filter image from the narrow-band F502N filter image. This difference image reveals an asymmetric biconical [O III]λ5007 outflow. The white cross in all the figures is the optical core (*Gaia* position).

6.1.2 Optical Imaging

In optical, we used observations from *HST WFC3-UVIS2* F502N and F547M filter (Proposal ID: 12212, PI: D. Michael Crenshaw). Our aim is to get a 5007 Å line image, so we adopted the following procedure to get the line image. Under the assumption that the continuum emission around [O III]λ5007 line has a zero slope (which is in agreement with spectra in this case), we selected six source-free regions having sizes of $10'' \times 10''$ in the F547M and F502N observations, determined the scale factors and applied the mean scale factor (c) and subtracted one filter observation from the other as given below

$$f(line) = cf(N) - f(M) \tag{6.1}$$

Here, f(N) and f(M) are the brightness in counts/sec in the narrow F502N filter (that contains the [O III]λ5007 emission line) and medium-band filter F547M (that contains the continuum emission). The parameter c is the scaling factor, which is the mean of the ratio of the fluxes in the narrow-band filter, F502N and the medium-band filter, F547M was determined from six source-free regions. Then, we converted the observed [O III]λ5007 (continuum subtracted) images to flux scale using the KEYWORD `PHOTFLAM` given in the image headers. The observed medium-band F547M image, the narrow-band F502N image and the continuum-subtracted image are shown in Fig. 6.2. These images have an FWHM angular resolution of $\sim 0.1''$.

6.1.3 Optical/infrared integral field spectroscopy

We used archival near-infrared and optical IFU observations from Gemini, obtained under program IDs GN-2015A-DD-6 (PI: Mason Rachel) and GN-2010A-Q-38 (PI: Anil Seth), respectively. Additional optical IFU data from the *MaNGA* survey were also incorporated. Data reduction procedures are detailed in Chapter 2. The objective is to fit the emission lines to extract their fluxes and velocity information.

For fitting the emission lines, we followed a non-parametric approach which involves the removal of the underlying continuum and fitting multiple Gaussian components to the emission lines. In the case of *GMOS* data, we identified line-free regions on either side of our region of interest, namely the [O III]λ5007 region ($\lambda\lambda$ = 4990−5040 Å). We fitted a first-order polynomial to the line-free regions and then subtracted the function from the observations. After continuum subtraction, we fitted the [O III]λ5007 emission line with two Gaussian components to extract the flux and other properties of the line using the non-linear least square minimization algorithm within `Curvefit` module of `Scipy` (Virtanen et al., 2020). An example of the fit is shown in Fig. 6.3. For the broad Hβ line, we fitted three Gaussian components: one for the narrow AGN component, the second for the broad AGN component and the third for the broad outflowing component. While fitting the broad and narrow AGN components, we fixed the peak velocity to be the same; however, the line widths were treated as free parameters and were allowed to vary. For the broad outflowing component, no restriction was imposed, either for the peak of the component or the width of the component.

From our fits to the Hβ line, we obtained a σ of 385 kms^{-1} for the broad Hβ component, which is similar to the value of σ = 334 kms^{-1} obtained by Brum et al. (2019). The procedure adopted in this work to fit the emission lines is thus appropriate. We fitted the lines [N II]$\lambda\lambda$6548,6584 and Hα lines together. For the Hα line, we used three Gaussian components similar to that used for the Hβ line. In addition, we used two Gaussians for the two [N II]$\lambda\lambda$6548,6584 lines. Here, we tied the widths of the [N II]$\lambda\lambda$6548,6584 lines to the width of the narrow component of Hα. For the narrow lines such as [N II]λ5755, [S II]$\lambda\lambda$6716,6732 and the H2λ2.4085 line from *NIFS*, we followed the same methodology used for the [O III]λ5007 line.

From the Gaussian fits to the [O III]λ5007 line emission in the observed spectra (not corrected for instrumental resolution), we estimated non-parametric values (Zakamska & Greene, 2014) such as the velocity ($v50$, the velocity where the cumulative flux of the line becomes half of the total flux), velocity dispersion ($W90 = v95 - v5$, where $v95$ and $v5$ are the velocities at which the flux becomes 95% and 5% of total flux) and the asymmetry $\left(R = \frac{(v95-v50)-(v50-v5)}{v95-v5}\right)$ of the line.

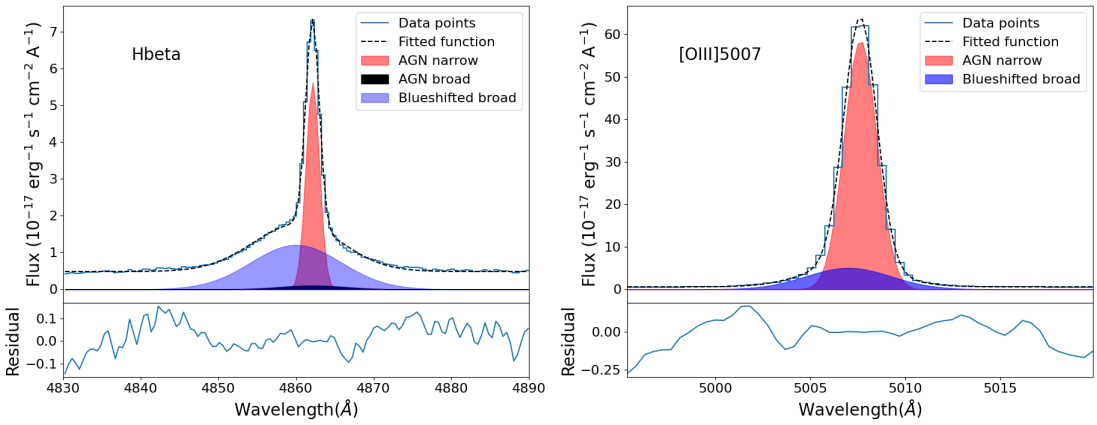

Fig. 6.3 Gaussian fit to the observed Hβ (left) and [O III]λ5007 (right) emission lines along with the residuals (lower panel of each spectrum). Here, shaded blue is the Gaussian fit to the outflowing component, red and black are the Gaussian fits to the narrow and broad components, and the dotted black line is the best-fit spectrum. The observed spectra are shown as a solid blue line.

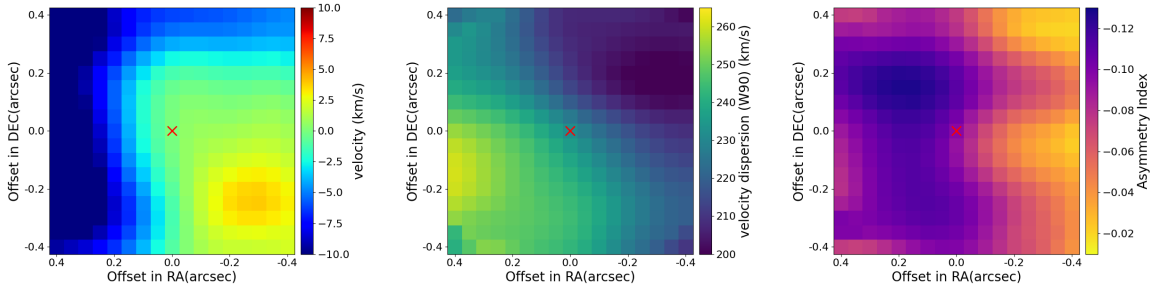

Fig. 6.4 Kinematics map of [O III]λ5007 line emission. Left panel: Velocity map. Middle panel: The map of the W90 parameter, which is equivalent to velocity dispersion. Right panel: The map of asymmetry index. The red cross represents the core (optical *Gaia* position).

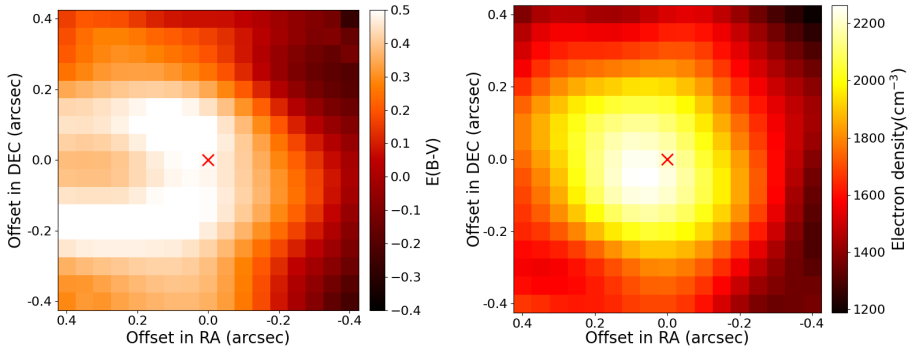

Fig. 6.5 Left panel: The map of E(B$-$V). Right panel: The map of electron density calculated from [S II]$\lambda\lambda$6717,6731 line ratio. The red cross is the core (optical *Gaia* position).

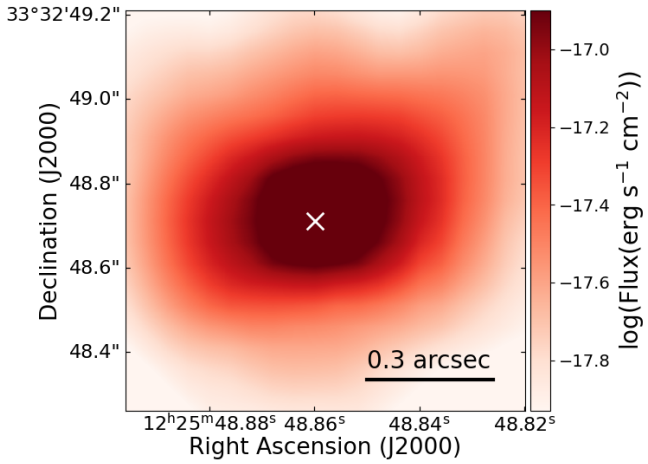

Fig. 6.6 The molecular $H_2\lambda 2.4085$ image of NGC 4395. The core of NGC 4395 taken as the optical *Gaia* position is shown as a white cross.

Also, from fits to the [S II] doublet and using the ratio of the [S II]λ6716 to [S II]λ6731 lines, we estimated the electron density. This line ratio is sensitive to electron densities of the order of $\sim 10^2$ - 10^4 cm^{-3}. To estimate the electron density, we assumed an electron temperature of 10,000 K. We calculated the internal extinction E(B−V) from Hα and Hβ line ratio using the following formula (Miller & Mathews, 1972; Veilleux et al., 1995)

$$E(B-V) = 1.925 \times log \frac{\left(\frac{I_{H\alpha}}{I_{H\beta}}\right)_{obs}}{3.1}. \tag{6.2}$$

The maps for the velocity and velocity dispersion of the [O III]λ5007 line emitting gas and for the asymmetry parameter of the line are given in Fig. 6.4, whereas the E(B-V) map and the electron density map are shown in Fig. 6.5. The molecular $H_2\lambda 2.4085$ image is shown in Fig. 6.6. These figures cover approximately the central $1'' \times 1''$ region of NGC 4395. This is because the radio emission at 15 GHz has an extension of $\sim 0.5''$, and our aim is to investigate the interaction of the radio jet with the ISM.

We used the spectrum of the central brightest pixel from *MaNGA* data reduction pipeline (DRP) data, which covers the central $0.5'' \times 0.5''$ region of NGC 4395, and largely encompasses the $\sim 0.5''$ extent (total) of the radio jet, the region of interest here to investigate the radio jet−ISM interaction. By using the advantage of this wavelength region, we detected shock-sensitive lines [O III]λ4363, He IIλ4886 (which are beyond the limit of *GMOS*), [O III]$\lambda\lambda$4959,5007, Hβ, [N II]λ5755 and [N II]$\lambda\lambda$6548,6584 lines (as shown in Fig 6.7) and estimated the parameters. These parameters are thus a representation of the physical conditions

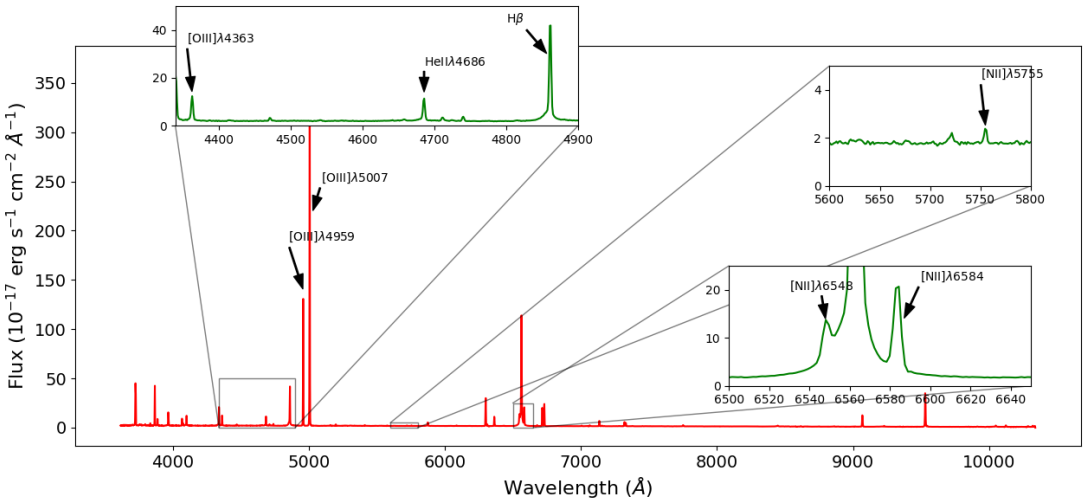

Fig. 6.7 The rest-frame spectrum of NGC 4395 from *MaNGA* covering the central brightest $0.5''\times0.5''$. The lines used to calculate the line intensity ratios are marked.

in the central $0.5''\times0.5''$ region. We fitted the emission lines in the same way as explained in the previous section and estimated the emission line fluxes.

6.1.4 ALMA

We used two archival data sets from *ALMA* (Data-ID: 2017.1.00572.S, PI: Davis, Timothy), which were carried out on March 22, 2018, and January 23, 2019, with *ALMA* band 6 in the frequency range of 227.47−246.43 GHz. The on-source integration time was 2037 s and 423 s, respectively. During the observations, a total of 46 antennas were used, with a minimum baseline of 15.1 m and a maximum baseline of 783.5 m. For the observations on both days, the quasar J1221+2813 was observed as a phase calibrator, and J1229+0203 was observed as a flux density and bandpass calibrator.

We reduced the data using CASA with the standard data reduction pipeline of the *ALMA* observatory. We show in Fig. 6.8 (upper left) the continuum image of NGC 4395 at 237.1227 GHz observed on 22 March 2018, having a synthesized beam size of $0.805''\times0.469''$ along position angle (PA) of 356 deg. From two-dimensional Gaussian fits, we found the peak and integrated flux densities to be 93±20 μJy beam^{-1} and 131±45 μJy, respectively. Also, the continuum image at 237.1227 GHz, observed on 23 January 2019, is shown in Fig. 6.8 (upper right). It has a synthesized beam size of $1.935''\times1.253''$ along PA of 3 deg. From Gaussian fits to the data, we found the peak and integrated flux densities to be 274±21 μJy beam^{-1} and 287±41 μJy respectively. These results from an independent analysis are also in agreement with those of Yang et al. (2022). We used the task `TCLEAN` to generate the spectral data cubes.

The CO line maps are shown in Fig. 6.8 (lower panels). From both the observations, we found the peak of the CO(2−1) emission to be displaced by around 0.9″ (∼ 20 pc) from the nucleus (as determined by *Gaia*) of NGC 4395.

6.1.5 VLA

The source was observed with the *VLA* A-configuration at 15GHz (PI: Payaswini Saikia, Legacy ID: AS1409). We reduced the data using standard procedures that include flagging bad data using *CASA* (see Saikia et al. 2018 for details). The beam size obtained is 0.129″×0.124″ with a PA of −18 deg. The final image at 15 GHz has an rms noise of 11 μJy/beam. The contours of the 15-GHz image shown in the left panel of Fig. 6.9 are at 0.03, 0.05 and 0.10 mJy/beam. The western jet component has a peak flux density of 44.6±1.0 μJy/beam. Though it is fainter related to the core and eastern components, it is detected at about the 4σ level.

The source was also observed at 4.8 GHz (C band) in the *VLA* B-configuration (PI: J.S. Ulvestad, Legacy ID: AU079). We reduced this data using standard procedures in *AIPS* by using 3C286 as the flux density calibrator and 1227+365 as a phase calibrator. We achieved an rms noise of 48 μJy/beam. The beam size in the final reduced image is 1.75″×1.19″ along a PA of 89 deg. The final images at 15 GHz and 4.8 GHz are shown in Fig. 6.9.

6.2 Results and Discussion

6.2.1 Radio morphology

The *VLA* 15 GHz image (Fig. 6.9, left panel) showed the source to be a triple, with E being the eastern component of the triple (Saikia et al., 2018). The weaker central component of the triple is coincident with the optical *Gaia* position, while component E is displaced from it by about 220 mas, corresponding to a projected distance of 4.6 pc. The western component (W) is separated from the central component by 4.2 pc. However, the overall projected extension of the source is ∼ 10 pc. The source is also highly asymmetric in brightness; the ratio of peak brightness of components E to W is 3.8. Component E has a spectral index, α, of -0.64 ± 0.05 (S$\propto \nu^{\alpha}$) and a brightness temperature, T_B of (2.3±0.4)×10^6 K, showing it to be a non-thermal source. For the central feature $\alpha = -0.12\pm0.08$, and non-detection of a sub-pc scale compact component sets $T_B < 5.9\times10^5$ K (Yang et al., 2022). Radio cores being resolved out in low-mass AGN when observed with milliarcsec resolution has been reported earlier (Nyland et al., 2017). Variability or episodic nuclear jet activity could also contribute to the non-detection of a core.

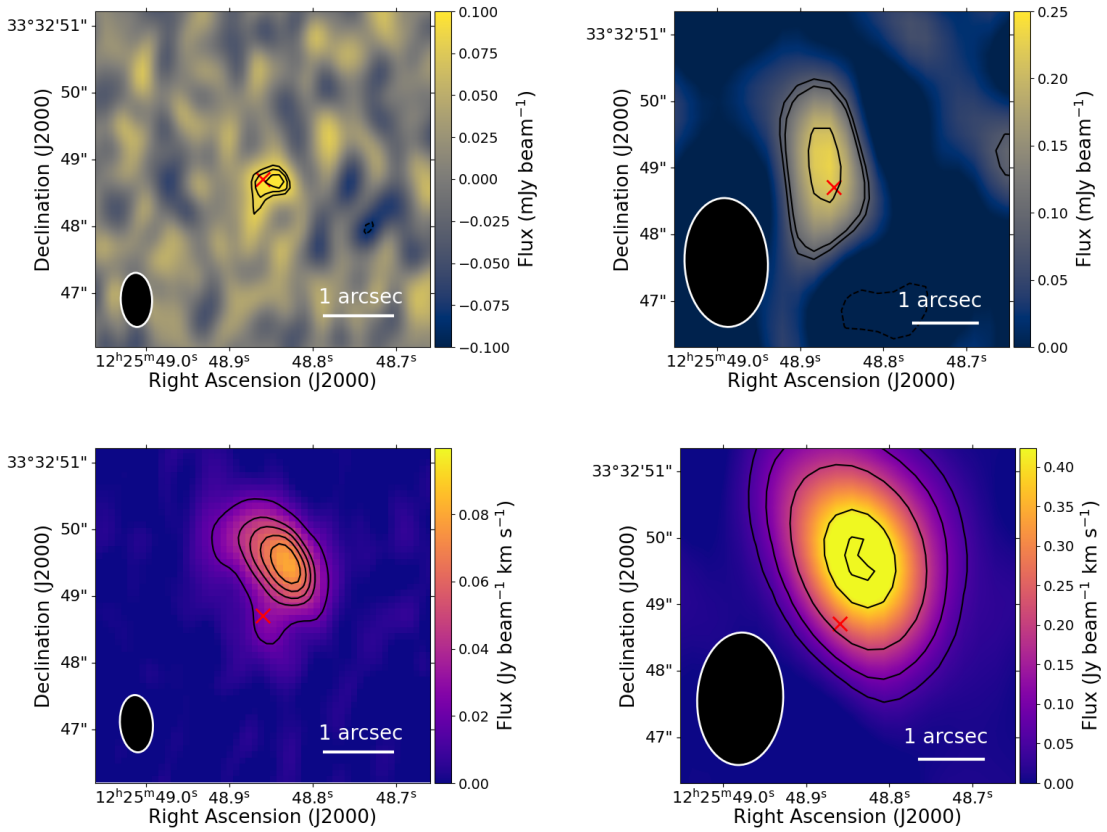

Fig. 6.8 Upper panel: The continuum emission at 237 GHz based on observations with *ALMA* on 22 March 2018 (left) and 23 January 2019 (right). The contours are -0.08, 0.08, 0.09 and 0.1 Jy/beam (left) and -0.08, 0.08, 0.1, and 0.2 Jy/beam (right). Lower panel: The CO(2−1) emission for the observation on 22 March 2018 (left) and 23 January 2019 (right). The contours are 0.02, 0.04, 0.05, 0.06 and 0.07 Jy beam^{-1} km s^{-1} (left) and 0.05, 0.1, 0.2, 0.4 and 0.5 Jy beam^{-1} km s^{-1} (right). The red cross is the optical *Gaia* position. Black ellipses show the synthesized beams.

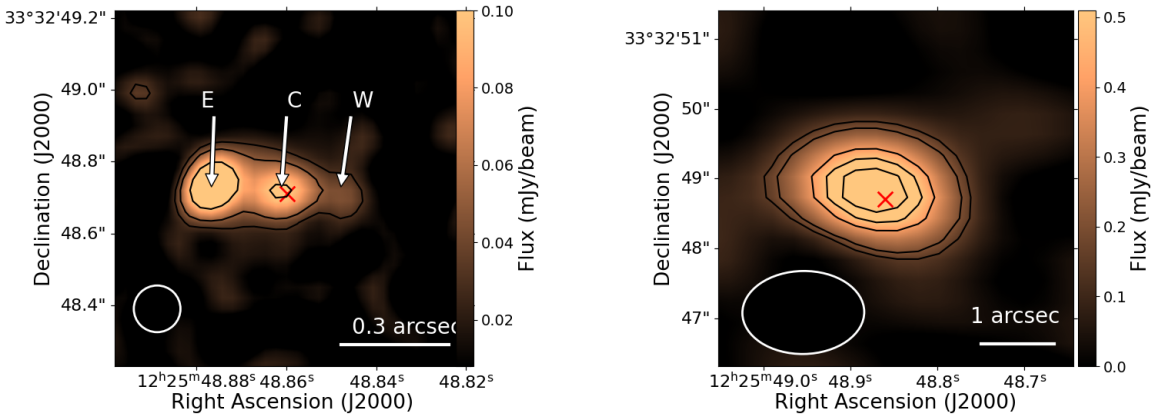

Fig. 6.9 Left: The *VLA* radio images at 15 GHz with a size of $1'' \times 1''$. The contours are at 0.03, 0.05, 0.10 mJy/beam. The rms noise is 11 μJy/beam. Here, C is the radio core, E is the eastern jet component, and W is the western jet component. Right: The 4.8 GHz *VLA* image with a size of $5'' \times 5''$. The contours are at 0.15, 0.20, 0.40, 0.50, 0.60 mJy/beam. The rms noise is 48 μJy/beam. The synthesised beams are shown as white ellipses. These have a size of $0.129'' \times 0.124''$ with PA of -18 deg (left panel) and $1.75'' \times 1.19''$ with PA of 89 deg (right panel). The red cross in both the panels represents the optical *Gaia* position.

The triple structure is strongly reminiscent of bipolar jet ejection in radio-loud AGN, and we suggest that the outer components (W and E) are formed by weak radio jets from the IMBH, and refer to the central component as the radio core. We refer to W and E, the end-points of the radio emission as jets to explore jet−ISM interaction. Low-power radio jets ($P < 10^{42}$ erg s^{-1}) can have a significant effect on the ISM of the host galaxy, interacting with clouds of gas and heating the gas, entraining ambient gas, losing collimation and sometimes forming arc-like fronts (Rampadarath et al., 2018).

6.2.2 Nature of radio emission in the central 10 pc region

The radio emission observed in the central pc-scale region of a dwarf galaxy could be from a variety of physical processes, such as low-power jets, AGN-driven wind, star formation, coronal activity and free-free emission from thermal gas (Panessa et al., 2019). Radio structure, spectral index, polarization characteristics of the radio emission if detectable in future, spatial correlation of radio structure and different gaseous components, spectral line diagnostics of the different components of the ISM could provide valuable clues in identifying the dominant processes. In NGC 4395, the radio morphology of a triple radio source clearly shows signs of interaction on the eastern side, which appears to bend sharply, as seen in the high-resolution image (see Yang et al., 2022), indicating jet−ISM interaction. This was reinforced by a detailed

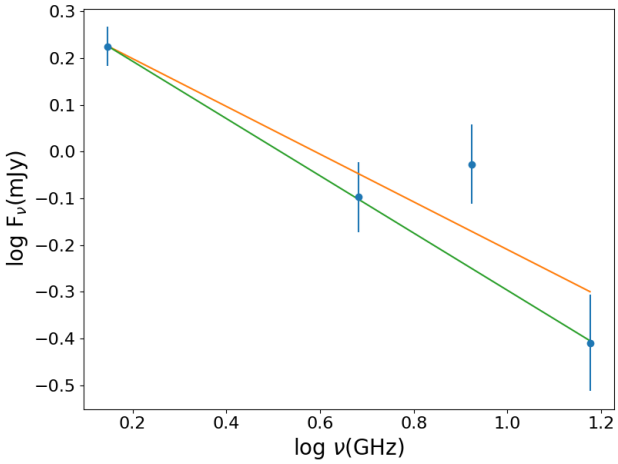

Fig. 6.10 Plot of flux density against frequency. The solid lines are linear least squares fits to the data. The orange line is the fit to all the data points, while the green line is the fit excluding the 8.4 GHz measurement.

study of the line-emitting gas. The [O III]λ5007 emission appears closely associated with the radio source, ionized by shocks as the jets flow outwards. Line-ratio diagnostics, estimation of gas temperatures from line ratios, and comparison of line ratios with theoretical predictions using `MAPPINGS` models all showed shocks to be the dominant process responsible for the ionization. The eastern component, which is more prominent at radio wavelengths, showed stronger signs of interaction with the ISM than the western component.

The spectral index (inclusive of all the three components) derived over the 1.4−15 GHz range (see Fig. 6.10) gives a value of $\alpha = -0.51\pm0.11$ ($S_\nu \propto \nu^\alpha$) and $\alpha = -0.61\pm0.01$ excluding 8.4 GHz point. We note here that the flux density measurements are not simultaneous and could be affected by the variability of the central AGN. However, considering only the eastern jet/component, Yang et al. (2022) obtained a value of $\alpha = -0.64\pm0.05$. This is very close to the theoretical injection spectral index (Kirk et al., 2000). Considering the source to have a spectral index in the range -0.51 to -0.64, the inverse Compton scattering of the CMB photons and radio photons can give rise to a power law X-ray spectrum whose photon index, Γ can be 1.51 to 1.64. This is close to the value of $\Gamma = 1.67$ found by Kammoun et al. (2019) from an analysis of *XMM* data in the 2−10 keV band.

Using the observed luminosity at 1.4 GHz, we calculated the jet power as (Cavagnolo et al., 2010)

$$P_{jet} = 5.8 \times 10^{43} \left(\frac{L_{1.4GHz}}{10^{40} ergs^{-1}} \right)^{0.7} \tag{6.3}$$

Using $L_{1.4GHz} = (6.1\pm0.3)\times10^{34}$ erg s^{-1} (Ho & Ulvestad, 2001) we estimated the jet power to be $P_{jet} = (1.3\pm0.3)\times10^{40}$ erg s^{-1}. It is thus evident that the jet in NGC 4395 is weak compared

to powerful radio galaxies having typical jet powers of $10^{44} - 10^{45}$ erg s^{-1} (Rusinek et al., 2016).

The above considerations all show that the radio emission in the central 10 pc region in NGC 4395 is from a low-power jet launched by an IMBH.

6.2.3 Radio and [O III]λ5007 emission

Fig. 6.11 shows the [O III]λ5007 map of NGC 4395 over a region of $1'' \times 1''$ in the total line emission (left panel), the narrow line component (middle panel) and the broad outflowing line component (right panel). Also, overplotted in these figures are the 15 GHz radio contours in green and the [O III]λ5007 *HST* emission in black. The broad outflowing component of [O III]λ5007 emission is brighter in the eastern side, where the radio emission also tends to be brighter. From these figures, it is evident that the total [O III]λ5007 emission is prevalent over the entire extent of the radio emission, with the peak of the total [O III]λ5007 emission coinciding with the peak of the central 15 GHz emission and the outflowing component of the [O III] line emission is displaced towards the east and overlaps with the eastern radio component. We note here that the peak of the [O III]λ5007 flux from *GMOS* and that from *HST* are comparable, with values of $(1.56\pm0.08)\times10^{-15}$ erg s^{-1} cm^{-2} and $(1.25\pm0.06)\times10^{-15}$ erg s^{-1} cm^{-2} respectively. The pixel scales of the [O III]λ5007 images from *GMOS* and *HST* are $0.05''$ and $0.04''$, respectively. The *HST* [O III]λ5007 emission is asymmetric, has a cone-like structure with a convex shape near the terminal points of the radio jet, resembling bow shocks in FRII radio galaxies (Kaiser & Alexander, 1999). The eastern [O III]λ5007 cone has a narrower opening angle, while the western cone has a wider opening angle.

Also, the western [O III]λ5007 cone has a more pronounced convex-shaped morphology compared with the eastern one. The asymmetry in the [O III]λ5007 emission could be due to the jets passing through an inhomogeneous medium. The eastern jet is brighter in the radio band, travelling in a denser and larger E(B−V) medium (see Fig. 6.5), could have ionized the gas, leading to dimmer [O III]λ5007 emission and brighter synchrotron emission because of shock-induced compression. Similarly, the western jet is travelling in a less dense medium, with smaller E(B−V) values, and enhanced [O III]λ5007 emission. The observed morphology of the source in radio and [O III]λ5007 is unambiguous evidence for the interaction of the radio jets with the ISM of the host of NGC 4395 and is the first structural evidence of jet−ISM interaction operating on scales $\sim$ 10 pc in a triple radio source.

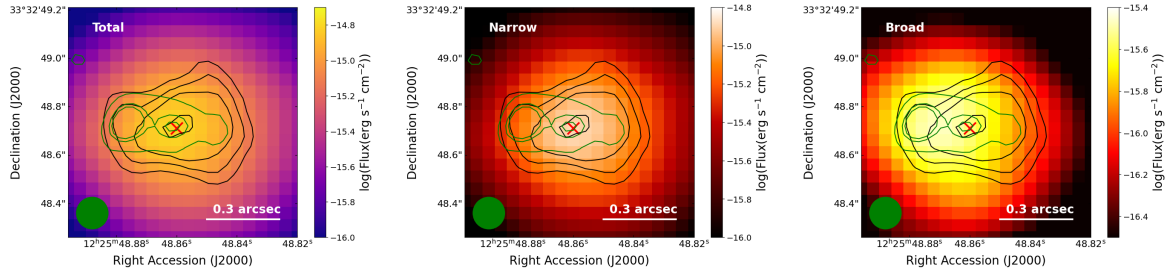

Fig. 6.11 *GMOS* [O III]λ5007 image in colour scale along with the radio emission at 15 GHz (green contours) with contour levels of 0.03, 0.08, 0.1 mJy/beam and *HST* [O III]λ5007 emission (black contours) with contour levels of (0.05, 0.1, 0.2, 1.0)$\times 10^{-15}$ erg s^{-1} cm^{-2}. The left panel shows the *GMOS* total flux in [O III]λ5007, the middle panel shows the *GMOS* flux in the narrow component of [O III]λ5007 and the right-hand panel shows the *GMOS* flux in the broad component of [O III]λ5007. The red cross is the core (optical *Gaia* position). The green circle is the synthesised beam of 15 GHz data with a size of $0.129'' \times 0.124''$ along PA -18 deg.

6.2.4 Multi-wavelength structure of NGC 4395

The 15 GHz image (Fig. 6.9) shows the highly asymmetric triple structure discussed earlier. In luminous radio galaxies, the components seen on the side of the jets that interact with a dense cloud in the ISM are usually nearer and brighter (O'Dea & Saikia, 2021; Saikia et al., 2003), as there is greater dissipation of energy on this side and the dense clouds inhibit the advancement of the jets. In the case of NGC 4395, the brighter component is farther from the nucleus, although its high-resolution radio structure and our optical emission line study suggest the interaction of the jet with the ISM. Therefore, a degree of intrinsic asymmetry in the radio jets cannot be ruled out. The velocities of the jets in these low-luminosity AGN are small so that relativistic beaming effects are not expected to be important, as also seen in the case of Seyfert galaxies (e.g. Roy et al., 2000; Whittle et al., 2004; Lal et al., 2011). Fig. 6.2 shows the [O III]λ5007 image of the $1'' \times 1''$, from *HST*. We found the [O III]λ5007 emission to be prevalent over the central $1'' \times 1''$. The central component of the 15 GHz radio emission and the peak of the [O III]λ5007 image from *HST* coincides with the optical *Gaia* position. The *Gaia* position is thus the AGN core. The right-hand panel of Fig. 6.2 clearly shows that the [O III]λ5007 gas distribution is asymmetric around the optical *Gaia* position (the AGN core). Also, the [O III]λ4007 emission exhibits a convex-shaped morphology at the terminal points on either side of the AGN core, though less conspicuous on the eastern side, but more prominent on the western side where the radio emission is weaker. These features suggest that the structure seen in [O III]λ5007 line emission could be an ionised outflow, which we explore later. A similar conclusion was also arrived at by Woo et al. (2019).

In Fig. 6.6 we show the $1'' \times 1''$ map of the source in molecular H_2 at 2.4085 μm, obtained from *NIFS* on the Gemini telescope. The molecular H2λ2.4085 is also extended in the East-West direction and spatially coincident with the 15 GHz radio emission. The 4.8 GHz emission (Fig. 6.9, right panel) is also spatially coincident with the 15 GHz emission and oriented in the East-West direction. The continuum emission at 237 GHz, too (the top panels in Fig. 6.8) coincides with the central radio source at 15 GHz and the optical *Gaia* position. However, the CO(2−1) line emission is concentrated at a larger distance ($\sim 0.9''$) from the central nuclear emission (see Fig. 6.8). The X-ray image (Fig. 6.1) too shows emission centred around the nuclear region and extended emission along the East-West direction.

6.2.5 BPT analysis

Emission line ratios in the optical are an essential tool to distinguish between star-forming galaxies and AGN. Also, they can be used to disentangle processes that lead to the line emission from star formation, AGN and shocks. To measure the emission line fluxes, we fitted line profiles of Hα and [N II]$\lambda\lambda$ 6548,6584, [S II]$\lambda\lambda$ 6717,6731, [O III]λ5007 and Hβ in the spectra of each spaxel, using two Gaussian components for narrow lines and three Gaussian components for the broad Balmer lines Hα and Hβ (see Sect. 2.3.1). The extra component in all lines is to represent the contribution from outflowing gas, while other components are for the BLR and NLR. During the fitting of the [N II] and Hα lines, the line widths of the narrow components were tied together, and the peak fluxes were left free. For Balmer lines (Hα and Hβ), we used the same velocity shift for the narrow component and one broad component, which are responsible for the NLR and BLR region, respectively. While fitting the [S II] lines, the width of these two lines was tied together. We used the [O III]λ5007/Hβ versus [S II]/Hα as well as [O III]λ5007/Hβ versus [N II]/Hβ diagnostic diagrams to investigate the physical processes causing the emission lines. These diagnostic diagrams are shown in Fig. 6.12. Each point in these diagrams represents one spaxel in the $1'' \times 1''$ region centered around NGC 4395. Here, the red star is the AGN, and the blue and cyan triangles represent the spaxels in the eastern and western jet components. Though all the spaxels lie in the AGN region of the BPT diagram, there is clear segregation between the core, the eastern and the western components.

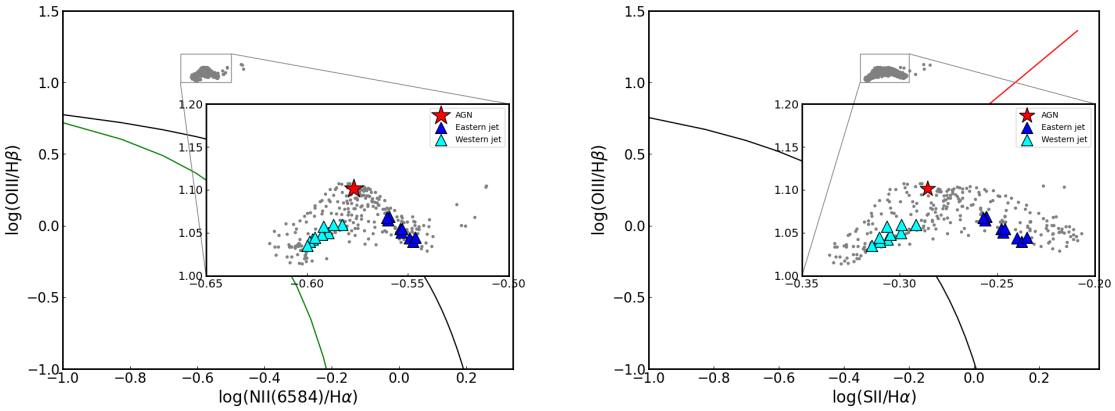

Fig. 6.12 The position of the spaxels belonging to the central $1'' \times 1''$ region of NGC 4395 in the line ratio diagnostic diagrams. The green solid curve is from Kauffmann et al. (2003b), and black and red solid lines are from Kewley et al. (2001). The typical error in these plots is 0.01 dex in both axes.

6.2.6 Diagnostics of the emission lines: Photoionization by AGN and/or shocks

6.2.6.1 Photoionization modelling

To characterise the ionization processes that operate in the central $1''$ region of NGC 4395, we carried out a comparison of emission line measurements from the observed *GMOS* spectra with photoionization and shock models from `MAPPINGS-III` (Sutherland et al., 2013) and implemented in `ITERA` (Groves & Allen, 2013). The emission lines in the spectra of material photoionized by AGN depend on the ionization parameter U, the slope of the ionizing continuum, β ($\phi_\nu \propto \nu^\beta$), the gas density and its metallicity. We generated output spectra for a range of input parameters with β ranging from -2 to -1.2 and log (U) varying from -4.0 to 0.0. We assumed solar metallicity (Cedrés & Cepa, 2002) and a hydrogen density of $n_H = 1000$ cm^{-3}.

Similarly, to generate the emission line spectra from shocked material, we used the `MAPPINGS-III` code again implemented in `ITERA`. We considered shock velocities (v) between 100 and 1000 km s^{-1}. The metallicity was assumed as solar consistent with that available in the literature (Cedrés & Cepa, 2002), and we considered both pure shock and shock plus precursor models. The magnetic parameter B was allowed to vary between 0.01 to 1000 μG. We show in Fig. 6.13, the comparison between model line ratios and observed line ratios in the log([O III]λ5007/Hβ) and log([S II]/Hα) plane for photoionization by AGN (left panel) and photoionization by shocks (right panel). The observed line ratios of the spaxels in the central $1'' \times 1''$ tend to lie in the region predicted by shock models. Thus, the observations

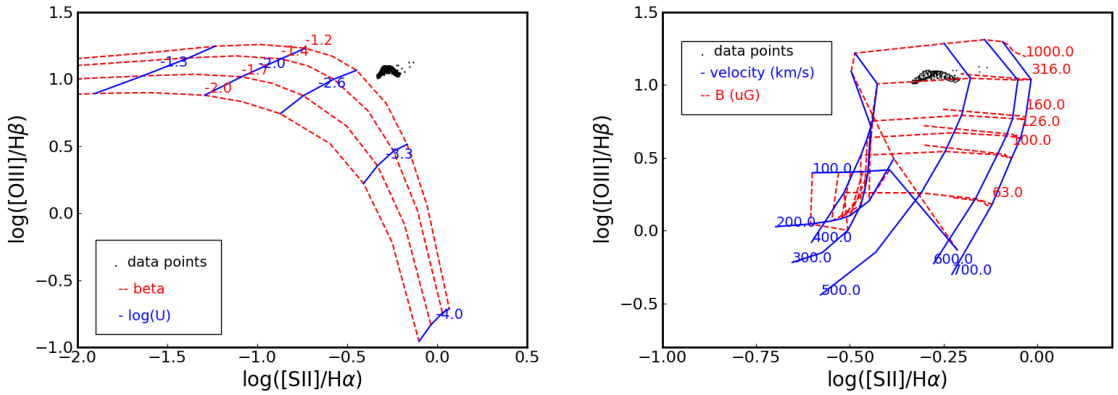

Fig. 6.13 Comparison between predictions of the line ratios due to photoionization by AGN (left panel) and shocks (right panel) and the observed line ratios. The clustered black points are the observed data points in the central $1'' \times 1''$. The model grids are shown for different shock velocities, magnetic fields and ionization parameters. The typical error of the data points in these plots is 0.01 dex in both axes.

analysed in this work show evidence of shocks contributing to the ionization of the gas in the central region of NGC 4395. This is possible with the hypothesis that the expanding radio jet from the central core, on its interaction with the ISM, leads to the shocks in the medium, which dominate the ionization of the gas over other processes, such as photoionization by AGN.

6.2.6.2 Electron temperature distribution

Knowledge of the electron temperature (T_e) in the central regions of AGN can help one to constrain the contribution of AGN to gas ionization. Shocks from AGN outflows could produce higher values of T_e (Riffel et al., 2021). We calculated the integrated T_e using two line intensity ratios namely R_{O3} = ([O III]$\lambda\lambda$ 4959,5007)/λ4363 and R_{N2} = ([N II]$\lambda\lambda$6548,6584)/λ5755 from *MaNGA* spectra and adopting the following relations (Riffel et al. 2021; Dors et al. 2020; Hägele et al. 2008).

$$\frac{T_{e[OIII]}}{10^4 K} = 0.8254 - 0.0002415 R_{O3} + \frac{47.77}{R_{O3}} \tag{6.4}$$

$$\frac{T_{e[NII]}}{10^4 K} = 0.537 + 0.000253 \times R_{N2} + \frac{42.13}{R_{N2}} \tag{6.5}$$

We found $T_{e[NII]} = (16.4 \pm 1.3) \times 10^3$ K and $T_{e[OIII]} = (16.8 \pm 1.0) \times 10^3$ K, which are comparable within the errors. These values are too large to be produced solely by AGN photoionization (cf. Fig. 6.15).

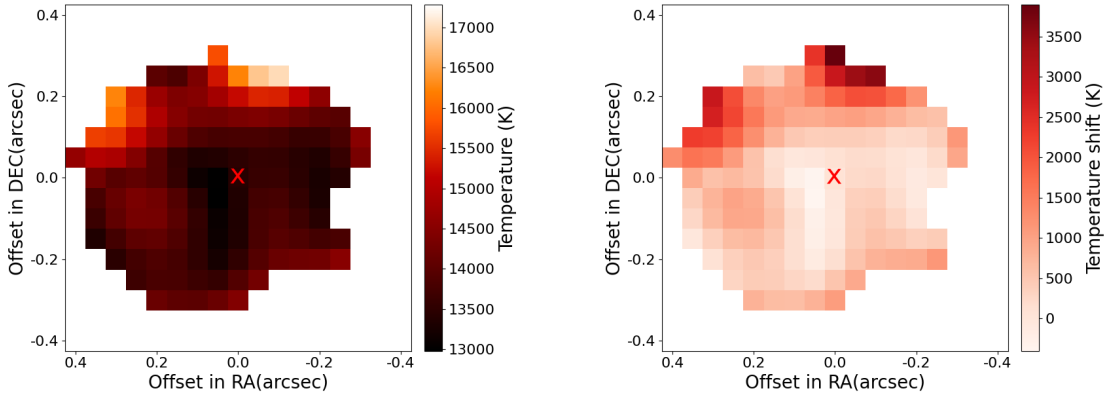

Fig. 6.14 Left panel: Temperature map from [N II] line ratio. Right panel: Temperature difference map with respect to the central spaxel. The red cross is the optical *Gaia* position.

To better characterise the spatial nature of T_e, we used [N II] lines from *GMOS* spectra to generate a spatially resolved map of T_e. Since [O III]λ4363 is not covered by the *GMOS* spectra, we used the line ratio R_{N2} to generate the T_e map. For this, we considered only those spaxels where the S/N ratio (ratio of the peak of the [N II]λ5755 line to the standard deviation of the pixels in the adjacent continuum) is greater than 30. The T_e map is shown in Fig. 6.14. We found T_e to have a range of values, with the value increasing from the centre of NGC 4395 outwards, both towards the eastern and western terminal points of the radio jet. This increase in temperature towards the eastern and western sides is evident in the temperature difference map shown in the right panel of Fig 6.14. This temperature difference map is generated by subtracting each temperature value from the temperature calculated over the central $0.05'' \times 0.05''$ region. This difference in temperature is significant, as the error in the temperature estimated using Equations 6.4 and 6.5 is typically around $6\% - 8\%$. The increase of temperature from the centre of NGC 4395 towards the edges (the difference in temperature is larger than the error in the estimated temperature), coinciding with the radio jet, points to the gas being mostly ionised by shocks. Shocks could be produced by the interaction of the radio jet with the ISM, and this increase of T_e from the centre towards the edges is a direct evidence of shock ionisation (Riffel et al., 2021).

6.2.7 Warm ionized gas and shock

The availability of gas reservoirs in the few tens of pc in the central regions of AGN is an important ingredient in the feeding and feedback processes in them. In particular, the presence of ionized gas in the central regions of AGN is believed to be a consequence of star formation as well as AGN activity. Such ionised emission could also be produced by shock excitation.

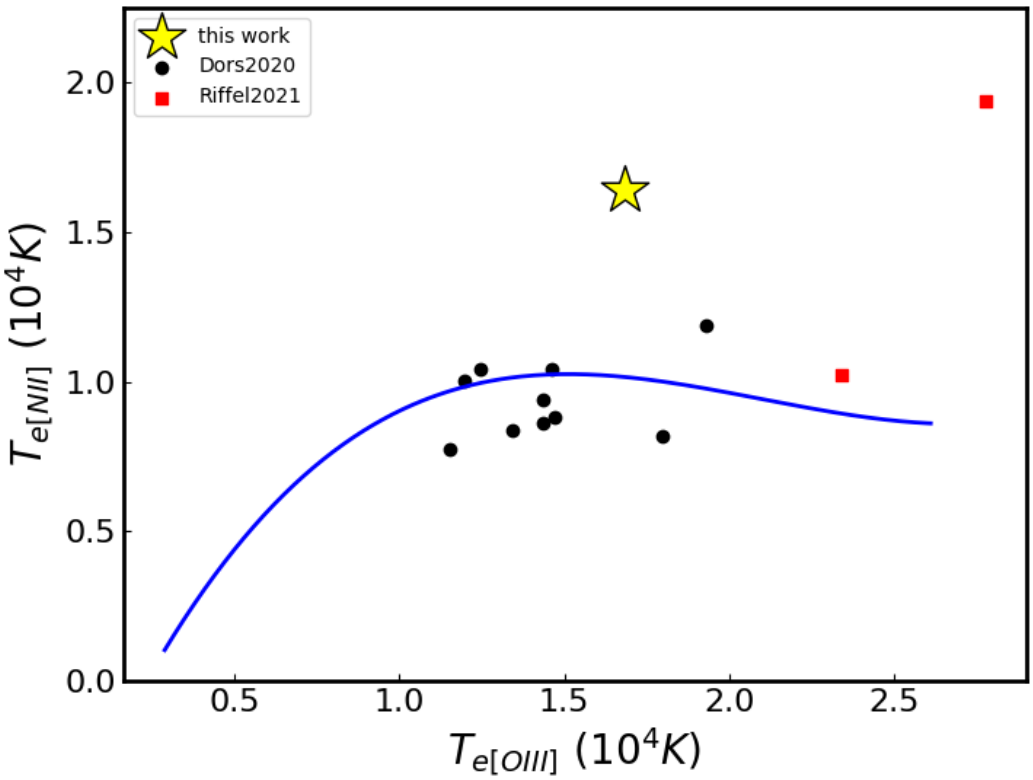

Fig. 6.15 Temperature plot. Here, the yellow point refers to NGC 4395. The blue curve is the AGN photoionization grid. The black and red points are from Dors et al. (2020) and Riffel et al. (2021) respectively.

The presence of such ionised gas is easily traced in the optical through emission lines and could trace the effect of AGN and the presence of outflows. From recent IFU observations in the optical and infrared of the central $1''\times1''$ region of NGC 4395, Brum et al. (2019) suggest that these may be ionized by the AGN based on the location of these spatially resolved measurements in the BPT diagram (Baldwin et al., 1981) (in the case of optical) and IR line ratio diagram (in the case of infrared). However, in the zoomed-in version of the BPT diagram, the eastern component, the core and the western component nicely get segregated (see Fig. 6.12). It is thus likely (similar to that seen in a nearby AGN NGC 1068 by D'Agostino et al. 2019b), the emission in the spaxels within the central $1''\times1''$ region of NGC 4395 could have a contribution from AGN, besides shock ionisation as discussed earlier.

Outflows can have multiple constituents, such as the hot ionized gas produced at the shock front, as well as neutral and molecular gas entrained in the flow. Shocks produced by AGN-driven outflows and/or radio jet−ISM interaction could also provide the possibility of energetic feedback altering the star formation characteristics of the ISM. We consider here the possibility of the shocks leading to the observed morphology of the ionized [O III]λ5007

We calculated the mass of the outflowing ionised hydrogen from the measured luminosity of the Hα emission using the following relation (Cresci et al., 2017).

$$M_{ion}^{out} = 3.2\times10^{5}\left(\frac{L_{broad}(H\alpha)}{10^{40}ergs^{-1}}\right)\left(\frac{n_e}{100cm^{-3}}\right)^{-1} \tag{6.6}$$

By considering $F_{broad}(H\alpha)$ = 7.40×10^{-14} erg cm^{-2} s^{-1} (integrated flux density over a circular aperture of radius 0.4$''$ on the extinction corrected outflowing component of Hα line image from *GMOS*), and mean electron density, n_e = 1700 cm^{-3}, we obtained M$_{ion}{}^{out}\sim$ 652M$_\odot$. Using a σ of 123 km s^{-1} (median σ of outflowing component of [O III]λ5007 line), we calculated the kinetic energy of this ionised mass as $E_{KE} = M_{ion}^{out}(\sigma^2)$ = 1.97×10^{50} erg. Taking a velocity of 9 km/s (median of velocity shift of outflowing component of [O III]λ5007 line) and the projected distance of the tip of the eastern jet as 0.3$''$ (6.3 pc), the time required to reach the terminal point is 2.16×10^{13} s. The power of the outflow is thus $P_{out} = E_{KE}/t$ = 9.14×10^{36} erg s^{-1}.

We calculated the mass and radius of the NLR using the following relations (Peterson, 1997).

$$M_{NLR} = 7\times10^{5}\left(\frac{L(H\beta)}{10^{41}ergs^{-1}}\right)\left(\frac{10^{3}cm^{-3}}{n_e}\right)M_\odot \tag{6.7}$$

$$R_{NLR} = 19\left(\frac{L(H\beta)}{\varepsilon10^{41}ergs^{-1}}\right)^{1/3}\left(\frac{10^{3}cm^{-3}}{n_e}\right)^{2/3}pc \tag{6.8}$$

By considering n_e of 1700 cm^{-3} (obtained from *GMOS* observations, see Fig. 6.5) and assuming a filling factor (ε) of 10^{-2} (typical upper limit; Peterson 1997) we obtained mass and radius of the NLR of NGC 4395 as 282 $M_\odot$ and 5.35 pc respectively over a circular region of 0.4″ radius.

We calculated the bolometric luminosity (L_{Bol}) using the observed brightness in soft X-ray, hard X-ray and Hα. In the hard X-ray band (14−195 keV), using the logarithm of the observed luminosity of 40.797 (Liu et al., 2014), we obtained L_{Bol} = 4.97×10^{41} erg s^{-1} using the following relation (Ichikawa et al., 2017):

$$log(L_{Bol}) = 0.0378 \times (log(L_X))^2 - 2.03 \times log(L_X) + 61.6. \tag{6.9}$$

In the soft X-ray band (2−10 keV), using the logarithm of the observed luminosity of 40.3 (Nardini & Risaliti, 2011), we obtained a L_{Bol} of 1.95×10^{41} erg s^{-1} using the relation given below:

$$log(L_{Bol}) = 0.0378 \times log(L_{2-10})^2 - 2.00 \times log(L_{2-10}) + 60.5. \tag{6.10}$$

Similarly, from Hα *GMOS* observations (considering a circular aperture of 0.4″) using a Hα luminosity of $5.43 \times 10^{38} ergs^{-1}$, we obtained L_{Bol} = 3.64×10^{41} erg s^{-1} using the equation given below (Greene & Ho, 2007).

$$L_{Bol} = 2.34 \times 10^{44} \times (L_{H\alpha}/10^{42} ergs^{-1})^{0.86} \tag{6.11}$$

Thus, from optical and X-ray observations, we found the source to have a bolometric luminosity in the range of (1.95−4.97)×10^{41} erg s^{-1}.

The disk accretion rate is generally represented by the Eddington ratio (λ_{Edd}) and is defined as

$$\lambda_{Edd} = L_{Bol}/L_{Edd} \tag{6.12}$$

Here, L_{Edd} is the Eddington luminosity defined as

$$L_{Edd} = 1.26 \times 10^{38} \left(\frac{M_{BH}}{M_\odot}\right) ergs^{-1} \tag{6.13}$$

Using L_{Bol} of (1.95−4.97)×10^{41} erg s^{-1} and M_{BH} values of (9.1×10^3 - 3.6×10^5) $M_\odot$ (Woo et al., 2019; Peterson et al., 2005) we obtained λ_{Edd} values of 0.004 to 0.044.

Given the jet power and the bolometric luminosity to be larger than the power of the outflowing ionized emission, the outflow seen in this source on the scale of the NLR of the source could be because of either jet-mode or radiative mode process. The optical spectrum

from *MaNGA* for the central region encompassing the complete core−jet structure having an angular size of 0.5″, shows the presence of the [O III]λ4363 and He IIλ4686 lines (see Fig. 6.7). The logarithm of the ratio between [O III]λ4363 and [O III]λ5007 lines is −1.6; He IIλ4686 and Hβ ratio is −0.72 and [O III]λ5007 and Hβ ratio is 0.86. These line ratios point to the presence of shocks (Comerford et al. 2017; Moy & Rocca-Volmerange 2002).

A comparison of the emission line ratios obtained from photoionization and shock modelling and observed line ratios also indicates the gas in the central regions of NGC 4395 to be ionised by shocks (see Fig. 6.13). Assuming a spectral index (α) of −0.64 (Yang et al., 2022) for the eastern jet component we derived the Mach number $\left(M_s = \sqrt{\frac{2\alpha-3}{2\alpha+1}}\right)$ (Al Yazeedi et al., 2021) of the shock as M_s=3.91. In the line ratios diagnostic diagrams, such as the [O III]λ5007/Hβ versus [S II]λ6717,6731/Hα and [O III]λ5007/Hβ versus [N II]λ6584/Hα diagrams, though all the spaxels lie in the region occupied by AGN, the structure is clearly delineated (see Fig. 6.12). Also, in the asymmetry of the line versus the velocity dispersion diagram (see Fig. 6.16; left panel), the spaxels in the eastern jet occupy a region of higher line asymmetry and higher velocity dispersion, while the western jet occupies a region of lower asymmetry index and lower velocity dispersion. High-velocity dispersion and high asymmetry of the lines are attributed to shock excitation (D'Agostino et al., 2019a). The eastern jet thus seems to occupy a region that is dominated by shock excitation, while the western jet seems to occupy a region of weaker shocks. Spaxels in the central 1″×1″ region show a tight correlation between the velocity dispersion and the shock-sensitive line ratio [N II]/Hα (see Fig. 6.16; right panel) (Ho et al. 2014). Shock models predict an increase in [N II]/Hα with an increase in shock velocity (Annibali et al., 2010). We show in Fig. 6.15 the position of NGC 4395 in the $T_{e[NII]}$ versus $T_{e[OIII]}$ diagram estimated from *MaNGA* spectrum. In the same diagram, there are measurements for a few AGN along with predictions from AGN photoionization from `MAPPINGS-III`. AGN NGC 4395 lies in a distinct position in this Figure, significantly deviant (inclusive of errors in the temperature measurement) from the position occupied by sources photoionized by AGN, pointing to such high temperatures being produced by shocks.

Photoionization and shock modelling from `MAPPINGS-III` (Sutherland et al., 2013), the electron temperature distribution and disturbed kinematics point to the gas in the central region of NGC 4935, excited by shocks. From a multitude of arguments, we conclude that shocks are the dominant process contributing to the excitation of the gas, and such shocks could be due to the interaction of the jet with the ISM in the central 10 pc region of NGC 4395.

6.2.8 A radio Jet−ISM interaction on 10 pc scale in NGC 4395

From an analysis of data in the optical, infrared, radio and millimetre bands, we have found evidence of a low-luminosity jet interacting with its host on the scale of about 10 pc. The eastern

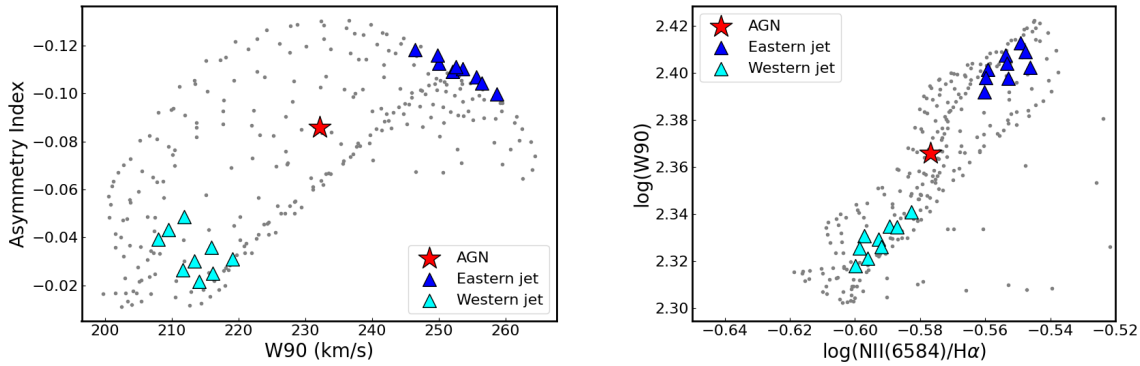

Fig. 6.16 Left Panel: Distribution of spaxels belonging to the $1''\times1''$ region of NGC 4395 in the asymmetry index versus the velocity dispersion plane. Right Panel: Distribution of spaxels belongings to the $1''\times1''$ region in the W90 ([O III]λ5007 line) versus intensity ratio of [N II]λ6584 and Hα lines.

jet component, which is brighter in the radio band, is resolved in the high-resolution High Sensitive Array (HSA) image into two components oriented approximately in the North-South direction, which is nearly orthogonal to the source axis (Wrobel & Ho, 2006). This indicates the interaction of the jet plasma with the ISM, with the plasma following the path of least resistance. On the eastern side, the [O III]λ5007 line-emitting gas has higher velocity, higher velocity dispersion and higher asymmetry (see Fig. 6.16, left panel), possibly due to the shocks associated with the interaction of the radio plasma with the [O III]λ5007 gas. The weakness of the [O III]λ5007 emission can either be due to the gas being more ionized or larger extinction, E(B−V) (see Fig. 6.5) or a combination of both. The weaker jet on the western side has a smaller effect on the [O III]λ5007 gas with a lower velocity dispersion and asymmetry. This suggests that there may be an intrinsic asymmetry in the oppositely directed jets. The radio emission is found to exist co-spatially with the emission at other wavelengths such as the hot ionised [O III]λ5007 emission in the optical band, the warm molecular $H_2\lambda$2.4085 in the infrared band and the 237 GHz emission in the millimetre band. However, the cold CO(2−1) emission is displaced by $\approx1''$ from the core. The presence of cold molecular gas is conducive for star formation. The displacement of the CO(2−1) gas and the paucity of cold gas along the source axis, possibly due to interactions by the jet, has led to the conditions less favourable for star formation on 10 pc scale. A schematic of our proposed coherent picture of the central region of NGC 4395 is shown in Fig. 6.17.

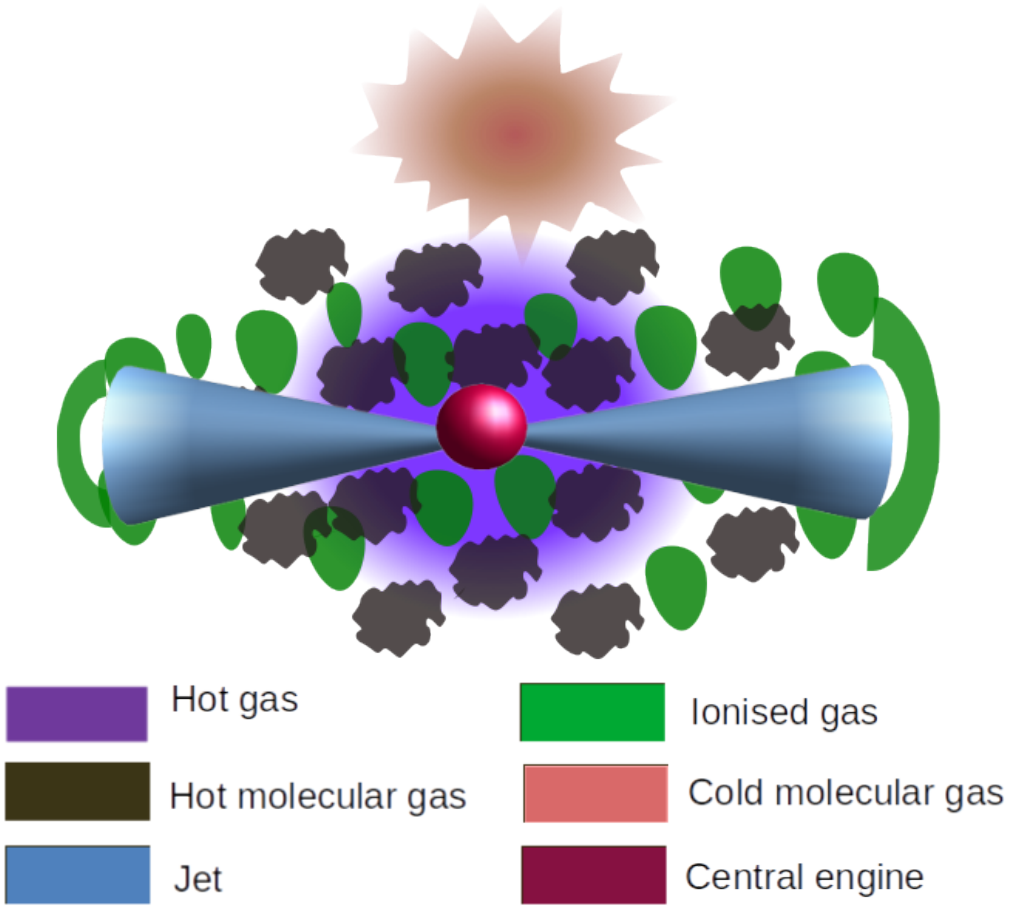

Fig. 6.17 Schematic diagram of our proposed scenario in the inner region of NGC 4395. The jet on its travel outwards from the central radio core, interacts with the medium and ionizes the gas via shock excitation. The radio core coincides with the optical *Gaia* position, the peak of the [O III]λ5007 emission and the peak of the 237 GHz emission. Ionised [O III]λ5007 has a cone-like structure, with the radio jet along the axis and causing the outflows. The CO(2$-$1) gas is located northwards by $\sim 1''$ from the radio core. While ionised [O III]λ5007, warm molecular H2λ2.4085 emissions are along the jet, there is a lack of cold CO in the vicinity, which is possibly due to interactions with the radio jet. As cold gas is needed for the star formation process, the lack of cold gas naturally leads to conditions less favourable for star formation at scales of $\sim$ 10 pc close to the centre of NGC 4395.

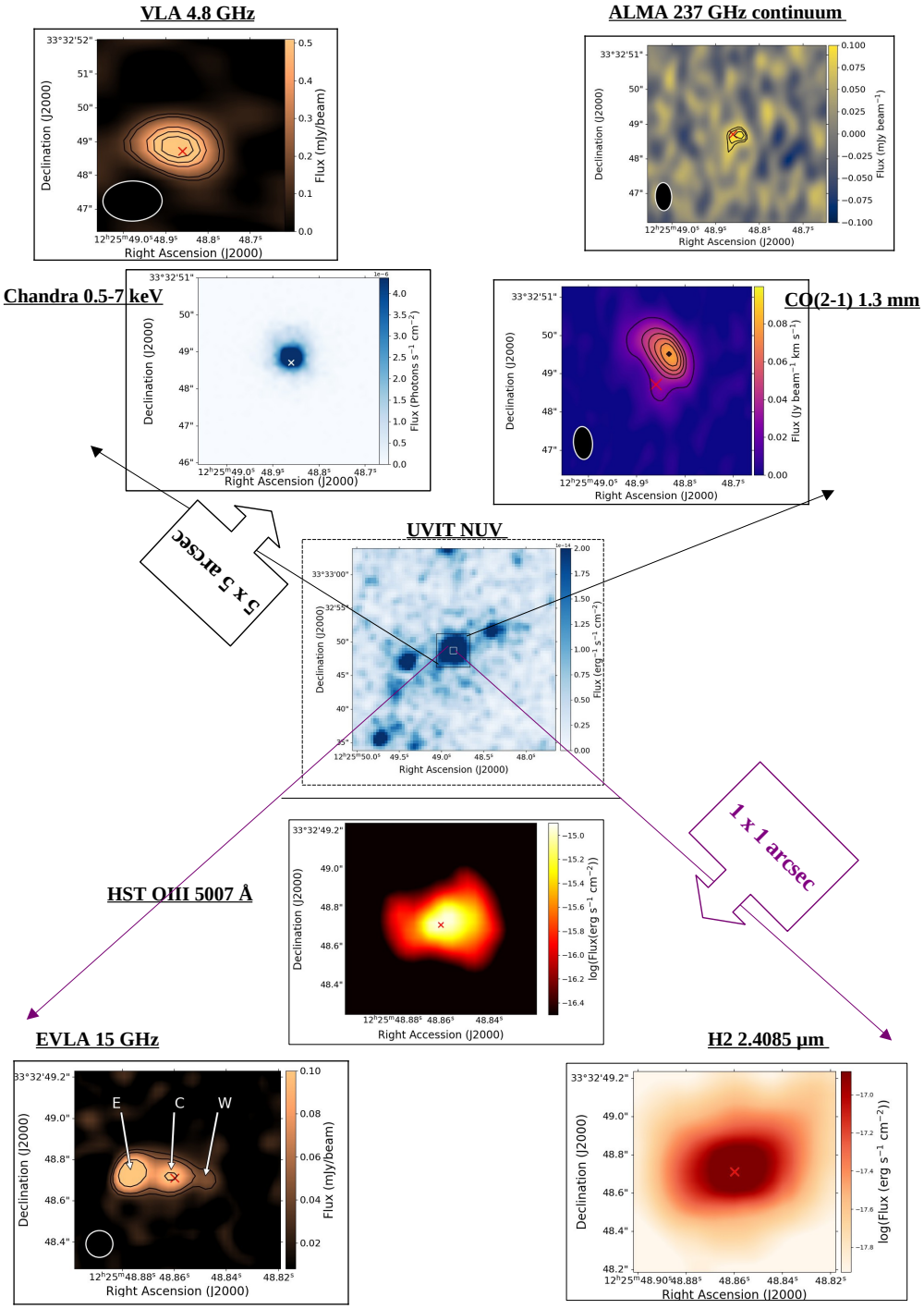

Fig. 6.18 The comprehensive picture of the jet−ISM interaction in the central $\sim$ 10 pc region of NGC 4395. In the centre is the image of NGC 4395 in the NUV filter observed with UVIT. This image has a size of $30'' \times 30''$. Also, shown in the same image are two square boxes, one of size $5'' \times 5''$ (black colour) and the other of $1'' \times 1''$ (white colour). On the top panels are the 4.8 GHz image from the *VLA*, 237 GHz image from *ALMA*, the CO(2-1) image from *ALMA* and the X-ray image in the 0.5−7 keV from *Chandra*. These images have a size of $5'' \times 5''$. The bottom panels show the 15 GHz image from the *VLA*, molecular H2λ2.4085 image from Gemini and [O III]λ5007 image from *HST* over a $1'' \times 1''$ region. In each of these images, the core of NGC 4395, taken as the *Gaia* position, is shown as a cross.

6.3 Summary

In this work, we carried out a systematic investigation of the central region of NGC 4395 using imaging and spatially resolved spectroscopic observations. We summarize our main findings below:

1. From *VLA* images at 15 GHz, NGC 4395 is found to show a triple radio structure having a projected size of $\sim$ 10 pc. The central component of the triple structure is found to coincide with the optical *Gaia* position, which we call as the radio core. The source is also highly asymmetric in brightness, with the eastern component brighter than the western one.

2. The triple radio structure in NGC 4395 is reminiscent of bipolar jet ejection in radio-loud AGN and the eastern and western components of this triple structure are formed by the low-power jet (P_{jet} = $(1.3 \pm 0.3) \times 10^{40}$ erg s^{-1}) powered by the IMBH in NGC 4395.

3. From *HST* observations we found the [O III]λ5007 emission to be prevalent over the entire extent of the radio emission, with the peak of the [O III]λ5007 emission coinciding with the optical *Gaia* position and the radio core. The [O III]λ5007 emission is asymmetric and shows a convex-shaped structure at the terminal points on either side of the core of NGC 4395, indicating an outflow. This asymmetry in the brightness of [O III]λ5007 emission could be due to intrinsic asymmetries causing different levels of ionisation, or differences in the degree of extinction or a combination of both.

4. The X-ray emission in the $0.5-7$ keV band is found to overlap with the radio jet. Similarly, the peak of the continuum emission at 237 GHz is spatially coincident with the radio core. Also, the molecular $H_2\lambda$2.4085 is found to be extended along the radio jet direction and have a close correspondence with the radio emission.

5. From AGN photoionization and shock modelling from `MAPPINGS-III` and the distribution of the electron temperature distribution, we conclude that the gas in the central region of NGC 4395 is excited mostly by shocks and such shocks could be due to the interaction of the radio jet with the ISM in the central pc region of NGC 4395. This is the first detection of radio jet$-$ISM interaction at such small spatial scales.

6. The cold CO$(2-1)$ emission is found to be displaced northwards of the radio core by about $1''$ ($\sim$ 20 pc). The paucity of cold molecular gas in the central region, possibly due to interactions with the jet, makes conditions less favourable for star formation on scales of about 10 pc in NGC 4395.

The detections of AGN and IMBH in a number of dwarf galaxies in recent years have opened the possibility of studying feedback processes in dwarf galaxies. Studies of nearby dwarfs also enable us to probe feedback processes on pc scales. Schutte & Reines (2022) reported a 150 pc long ionized filament in the dwarf galaxy Henize 2-10 from *HST* observations, which connect the black hole region with a site of recent star formation. Nyland et al. (2017) reported possible evidence of shock excitation in the nearby dwarf AGN galaxy NGC 404 with an amorphous radio outflow extending over $\sim$ 17 pc. NGC 4395 is the clearest example of a dwarf AGN with a triple radio structure, where there is clear evidence of jet−ISM interaction on the smallest scale of $\sim$ 5 pc on either side of the core. A comprehensive picture depicting this jet−ISM interaction in the central pc scale region based on the analysis of images from multiple wavelengths is shown in Fig. 6.18. This finding will bolster the prospect of finding more such instances in dwarf AGN host galaxies, paving the way for a better understanding of the complex interplay between AGN and their hosts on such small scales in these galaxies.

7

Summary and future work

7.1 Summary of the thesis

This thesis has presented observational results towards understanding the complex connection between AGN and the ISM of their host galaxies. From a systematic investigation carried out on a sample of AGN, the thesis has aimed to find clues to (a) what triggers outflows in AGN, (b) the impact of AGN on the star formation characteristics of their hosts, (c) the nature of AGN feedback on a dwarf AGN and (d) the smallest scales at which the AGN jet can affect the ISM of their host galaxies. For this, the thesis has used imaging data in X-rays, UV, optical and infrared wavelengths, and spatially resolved spectroscopic data in the optical, infrared, and mm bands. This chapter summarises the main results presented in this thesis and also outlines plans for investigations to be carried out in the future.

1. **Drivers of outflows in AGN:** Chapter 3 presented the results of a systematic analysis carried out on a sample of AGN to find the physical processes that drive outflows in AGN. The sample used in this study consisted of 538 AGN; of this, 197 are detected in the radio band, and 341 are radio-undetected. A systematic analysis was carried out on the observed [O III]λ5007 line to find ionised outflows. In the radio-detected sample, 56$\pm$7% showed outflows compared to the radio-undetected sample, where only 25$\pm$3%

were found to show outflow signatures. Thus, the outflow detection rate is larger in the radio-detected sample relative to the radio-undetected sample. The thesis has found a strong correlation between the outflow characteristics, such as the mass outflow rate and the kinetic power of the outflow, with the bolometric luminosity. This correlation indicates that radiation from AGN serves as the primary driver of outflows in both radio-detected and radio-undetected samples. Notably, the relationship between outflow properties and bolometric luminosity is more pronounced in radio-detected samples than in radio-undetected ones, and there is a positive correlation between radio jet power and the kinetic power of the outflow. These findings suggest that in radio-detected AGN, radio jets likely play a significant role in enhancing outflow dynamics, in addition to the primary influence of radiation. Also, the thesis has found star formation to be suppressed in the very central regions of their sample of sources, suggesting negative AGN feedback in the very central regions.

2. **Impact of AGN on the star formation characteristics of their host galaxies:** Chapter 4, presented results on the impact of AGN on the star formation characteristics of their hosts. This was done by mapping the star-forming regions in galaxies hosting AGN and looking for any correlations between the deduced star formation and AGN properties. The sample for this study consisted of 8 objects, of which seven were Seyfert type AGN, and one was a LINER. The observations for this study were from *UVIT*. Star-forming regions were identified, and important parameters such as the SFR were estimated. For five out of the eight sources, the surface density of SFR (Σ_{SFR}) was found to gradually decrease from the centre towards the outer regions, while it was not significant in the other three sources. Four sources are found to be located in the main sequence of star-forming galaxies, while the other four sources are found to lie away from the main sequence of star-forming galaxies. The thesis found a steep positive correlation between the Σ_{SFR} and extinction in UV with a slope more than the star-forming galaxies. Additionally, it found that $\Sigma_{SFR}^{Nuclear}$ is higher compared to Σ_{SFR}^{Total}, which points to the influence of AGN in enhancing the star formation characteristics of the host, with the impact being dominant in the central region.

3. **Nature of feedback in a dwarf AGN:** Chapter 5 presented results on new UV and narrow-band Hα observations acquired for studying the spatially resolved star-forming regions in the dwarf AGN. From the narrow-band Hα data, the thesis has found evidence for a gradual decrease in the age of the star-forming regions from the centre of the source outwards. Three star-forming regions close to the AGN were found to have a high surface density of SFR. One out of the three star-forming regions was also found to have a high

surface density of SFR and younger age, suggestive of the signature of positive feedback from the AGN. Few of the star-forming complexes in the source with enhanced 1.4 GHz radio emission were also found to contain more star-forming regions with a higher SFR. These complexes are known to have supernova remnants, arguing for supernova-induced star formation. By combining observations from different wavelengths, the thesis found evidence suggestive of both AGN and supernova feedback in the dwarf AGN, NGC 4395.

4. **Effect of AGN jet on the ISM of their host galaxy:** Chapter 6 presented results on feedback processes operating in the central region of the dwarf AGN using spatially resolved spectroscopic observations in the optical and infrared bands. From high-resolution observations in the radio band at 15 GHz from the *VLA*, the thesis found a triple radio jet-like structure with a projected linear size of $\sim$10 pc, with the central component of the radio source coinciding with the optical *Gaia* position. The triple radio structure seen in NGC 4395 is reminiscent of a bipolar jet. The [O III]λ5007 emission from *HST* was found to be asymmetric and have a convex shape structure at the terminal points on either side of the core, indicating an outflow. From photoionisation modelling, the thesis concluded that the gas in the central region of NGC 4395 is excited mostly by shock, and such shocks could be caused by the interaction of the radio jet with the ISM of NGC 4395. This is the first detection of radio jet$-$ISM interaction at such small spatial scales. Also, the *ALMA* observations used in the thesis have found a paucity of cold molecular gas in the central region. This is possibly due to the interaction of the jet with the medium, which makes conditions less favourable for star formation in the central region of NGC 4395.

7.2 Unique contributions of the thesis

This thesis concentrated on investigating the origin and impact of warm ionized outflows within host galaxies. By addressing key questions, it has contributed to valuable case studies and insights in several areas:

- **AGN feedback in dwarf galaxies:** Theoretical studies have largely suggested that feedback in dwarf galaxies is predominantly supernova-driven due to their relatively low masses and energy outputs. However, observational evidence of AGN feedback in these galaxies remains scarce, with He 2-10 being one of the few notable examples (Schutte & Reines, 2022). This thesis adds another example of AGN-driven feedback within a dwarf galaxy, demonstrating its presence even in lower-mass hosts.

- **Positive and negative AGN feedback:** Previously, both positive and negative feedback effects from AGN have only been documented in one source, NGC 5728 (Shin et al., 2019), where AGN-driven processes were seen to simultaneously suppress and stimulate star formation at different scales within the galaxy. This thesis presents a second example of this phenomenon, providing evidence that such dual feedback may not be unique to single sources but could be a more general feature of AGN activity.

- **Feedback by AGN with IMBH:** IMBHs, with their lower accretion rates and energy outputs, have often been overlooked in feedback studies. However, this thesis presents observational evidence of feedback from an IMBH in NGC 4395, demonstrating that even low-power AGN can significantly impact their surroundings. This finding expands the scope of AGN feedback studies to include a wider range of black hole masses and activity levels.

- **Extending observations to 10 pc scales:** Observational studies of AGN-driven ionized outflows have generally focused on regions 150 pc or larger from the AGN. This work has pushed the limits of resolution to the 10 pc scale, providing insights into how feedback processes unfold in even the innermost regions of the host galaxy. This refinement in scale deepens our understanding of the AGN's immediate environment and its interactions with the surrounding interstellar medium.

- **Radiation vs. Jet-driven outflows:** The mechanisms driving AGN outflows have been a topic of ongoing research, with both radiation-driven and jet-driven modes proposed. Through a statistical study of multiple sources, this thesis demonstrates that jets can play a substantial role in intensifying outflow activity, suggesting a complex interplay between radiation and mechanical feedback. This insight adds to the growing evidence that while radiation remains a major driver, jets can significantly amplify outflow dynamics in certain cases.

These contributions not only deepen our understanding of AGN feedback but also extend its scope, opening avenues for further studies on feedback mechanisms across galaxy types, black hole masses, and spatial scales.

7.3 Future perspective

Outflows in AGN manifest across multiple phases, from UFOs at relativistic speeds to cold molecular outflows, each impacting host galaxies in unique ways. This thesis primarily investigated warm ionized outflows, focusing on their origin and influence on host galaxies.

However, other phases—like UFOs, neutral atomic, and molecular outflows—each exert potentially significant but less explored effects. Understanding how these outflow phases interact with the host galaxy, particularly beyond the warm ionized phase, promises new insights into AGN feedback mechanisms, both positive and negative.

While studies have confirmed the existence of different phases of AGN outflows, their interconnections remain less explored, partly due to the high observational cost of obtaining multi-phase data simultaneously. However, investigating a well-selected sample of AGN sources across these phases could reveal whether these outflows represent evolutionary stages or discrete processes driven by varying feedback mechanisms. An evolutionary scenario could suggest, for instance, that UFOs evolve into slower molecular outflows over time, allowing us to trace a feedback continuum from the AGN's centre to its outskirts.

In this thesis, we detected evidence of both positive and negative AGN feedback in a single source, NGC 4395, using multi-resolution data. Alongside NGC 5728, this provides just two known cases with such dual feedback signatures. This suggests that more extensive surveys, spanning a broad range of AGN types and resolutions, are needed to capture a more complete picture of feedback at different scales. By incorporating high-resolution data across optical, infrared, and radio wavelengths, future studies could map feedback effects across multiple scales and phases.

References

Aalto S., et al., 2016, *A & A*, 590, A73

Abramowicz M. A., Fragile P. C., 2013, Living Reviews in Relativity, 16, 1

Al Yazeedi A., Katkov I. Y., Gelfand J. D., Wylezalek D., Zakamska N. L., Liu W., 2021, *ApJ*, 916, 102

Allison J. R., Sadler E. M., Meekin A. M., 2014, *MNRAS*, 440, 696

Álvarez-Álvarez M., Díaz A. I., Terlevich E., Terlevich R., 2015, *MNRAS*, 451, 3173

Andreani P., Boselli A., Ciesla L., Vio R., Cortese L., Buat V., Miyamoto Y., 2018, *A & A*, 617, A33

Annibali F., Bressan A., Rampazzo R., Zeilinger W. W., Vega O., Panuzzo P., 2010, *A & A*, 519, A40

Arsenault R., 1989, *A & A*, 217, 66

Asmus D., Gandhi P., Hönig S. F., Smette A., Duschl W. J., 2015, *MNRAS*, 454, 766

Ayubinia A., Woo J.-H., Rakshit S., Son D., 2023, *ApJ*, 954, 27

Baldassare V. F., Geha M., Greene J., 2020, *ApJ*, 896, 10

Baldwin J. A., Phillips M. M., Terlevich R., 1981, *Pub. Astron. Soc. Pac.*, 93, 5

Baron D., Ménard B., 2019, *MNRAS*, 487, 3404

Becker R. H., White R. L., Helfand D. J., 1995, *ApJ*, 450, 559

Belli S., et al., 2024, *Nature*, 630, 54

Bennett A. S., 1962, *Memoirs of the Royal Astronomical Society, 68, 163*

Bennett A. S., 1963, MNRAS, 127, 3

Benson A. J., Lacey C. G., Baugh C. M., Cole S., Frenk C. S., 2002, MNRAS, 333, 156

Bentz M. C., Manne-Nicholas E., 2018, ApJ, 864, 146

Bentz M. C., et al., 2006, ApJ, 651, 775

Bentz M. C., et al., 2009, ApJ, 705, 199

Bertin E., Arnouts S., 1996, A & A Suppl., 117, 393

Bing L., et al., 2019, MNRAS, 482, 194

Bischetti M., et al., 2019, A & A, 628, A118

Bluck A. F. L., Maiolino R., Sánchez S. F., Ellison S. L., Thorp M. D., Piotrowska J. M., Teimoorinia H., Bundy K. A., 2020, MNRAS, 492, 96

Bollati F., Lupi A., Dotti M., Haardt F., 2023, arXiv e-prints, p. arXiv:2311.07576

Bolton J. G., 1948, Nature, 162, 141

Bolton J. G., Stanley G. J., 1948, Nature, 161, 312

Boquien M., Burgarella D., Roehlly Y., Buat V., Ciesla L., Corre D., Inoue A. K., Salas H., 2019, A & A, 622, A103

Bosma A., Ekers R. D., Lequeux J., 1977, A & A, 57, 97

Bowyer C. S., Lampton M., Mack J., de Mendonca F., 1970, ApJL, 161, L1

Bradley L., et al., 2020, astropy/photutils: 1.0.0, doi:10.5281/zenodo.4044744, https://doi.org/10.5281/zenodo.4044744

Brenneman L. W., Risaliti G., Elvis M., Nardini E., 2013, MNRAS, 429, 2662

Brown M. J. I., et al., 2017, ApJ, 847, 136

Brum C., et al., 2019, MNRAS, 486, 691

Bruzual G., Charlot S., 2003, MNRAS, 344, 1000

Bruzual A. G., 1983, ApJ, 273, 105

Bundy K., et al., 2015, ApJ, 798, 7

Caccianiga A., et al., 2015, MNRAS, 451, 1795

Calzetti D., 2013a, in Falcón-Barroso J., Knapen J. H., eds, , Secular Evolution of Galaxies. Cambridge University Press, p. 419

Calzetti D., 2013b, Secular Evolution of Galaxies, 419

Calzetti D., Armus L., Bohlin R. C., Kinney A. L., Koornneef J., Storchi-Bergmann T., 2000, ApJ, 533, 682

Cardelli J. A., Clayton G. C., Mathis J. S., 1989, ApJ, 345, 245

Carniani S., et al., 2024, A & A, 685, A99

Cattaneo A., Best P. N., 2009, MNRAS, 395, 518

Cavagnolo K. W., McNamara B. R., Nulsen P. E. J., Carilli C. L., Jones C., Bîrzan L., 2010, ApJ, 720, 1066

Cayatte V., van Gorkom J. H., Balkowski C., Kotanyi C., 1990, AJ, 100, 604

Cedrés B., Cepa J., 2002, A & A, 391, 809

Cerruti M., 2020, Galaxies, 8, 72

Charlot S., Fall S. M., 2000, ApJ, 539, 718

Cid Fernandes R., Gu Q., Melnick J., Terlevich E., Terlevich R., Kunth D., Rodrigues Lacerda R., Joguet B., 2004, MNRAS, 355, 273

Colina L., Alberdi A., Torrelles J. M., Panagia N., Wilson A. S., 2001, ApJL, 553, L19

Comerford J. M., Barrows R. S., Greene J. E., Pooley D., 2017, ApJ, 847, 41

Condon J. J., 1992, Anu Rev. in Astronomy and Astrophysics., 30, 575

Condon J. J., Cotton W. D., Broderick J. J., 2002, AJ, 124, 675

Corbelli E., 2003, MNRAS, 342, 199

Cresci G., Vanzi L., Telles E., Lanzuisi G., Brusa M., Mingozzi M., Sauvage M., Johnson K., 2017, A & A, 604, A101

D'Agostino J. J., Kewley L. J., Groves B. A., Medling A., Dopita M. A., Thomas A. D., 2019a, MNRAS, 485, L38

D'Agostino J. J., et al., 2019b, MNRAS, 487, 4153

Damas-Segovia A., et al., 2016, ApJ, 824, 30

Davies R. I., Sugai H., Ward M. J., 1998, MNRAS, 300, 388

Davies R. I., Tacconi L. J., Genzel R., 2004, The Astrophysical Journal, 602, 148

Davies R. I., Müller Sánchez F., Genzel R., Tacconi L. J., Hicks E. K. S., Friedrich S., Sternberg A., 2007, ApJ, 671, 1388

Davies L. J. M., et al., 2016, MNRAS, 461, 458

Davies R. L., et al., 2024, MNRAS, 528, 4976

Dermer C. D., Giebels B., 2016, Comptes Rendus Physique, 17, 594

Diniz M. R., Riffel R. A., Storchi-Bergmann T., Riffel R., 2019, MNRAS, 487, 3958

Dopita M. A., Sutherland R. S., 1995, ApJ, 455, 468

Dors O. L., Maiolino R., Cardaci M. V., Hägele G. F., Krabbe A. C., Pérez-Montero E., Armah M., 2020, Monthly Notices of the Royal Astronomical Society, 496, 3209

Draine B. T., et al., 2007, ApJ, 663, 866

Draine B. T., et al., 2014, ApJ, 780, 172

Dullo B. T., Gil de Paz A., Knapen J. H., 2021, ApJ, 908, 134

Edge D. O., Shakeshaft J. R., McAdam W. B., Baldwin J. E., Archer S., 1959, MemRAS, 68, 37

Elvis M., 2000, ApJ, 545, 63

Evans I. N., Koratkar A. P., Storchi-Bergmann T., Kirkpatrick H., Heckman T. M., Wilson A. S., 1996, ApJ Suppl., 105, 93

Fabian A. C., 2012, Anu Rev. in Astronomy and Astrophysics., 50, 455

Falcke H., Wilson A. S., Simpson C., 1998, ApJ, 502, 199

Fanaroff B. L., Riley J. M., 1974, MNRAS, 167, 31P

Fath E. A., 1909, Lick Observatory Bulletin, 149, 71

Fernández-Ontiveros J. A., et al., 2020, A & A, 633, A127

Ferreras I., Cropper M., Kawata D., Page M., Hoversten E. A., 2012, MNRAS, 424, 1636

Feruglio C., et al., 2015, A & A, 583, A99

Filippenko A. V., Ho L. C., 2003, ApJL, 588, L13

Filippenko A. V., Sargent W. L. W., 1989, ApJL, 342, L11

Fiore F., et al., 2017, A & A, 601, A143

Flesch E. W., 2023, arXiv e-prints, p. arXiv:2308.01505

Forster K., Leighly K. M., Kay L. E., 1999, ApJ, 523, 521

Friedman H., Byram E. T., 1967, Science, 158, 257

Gadotti D. A., Athanassoula E., Carrasco L., Bosma A., de Souza R. E., Recillas E., 2007, MNRAS, 381, 943

Gaia Collaboration et al., 2022, arXiv e-prints, p. arXiv:2208.00211

Gallo L. C., Gonzalez A. G., Miller J. M., 2021, ApJL, 908, L33

Garcia-Burillo S., Sempere M. J., Combes F., Neri R., 1998, A & A, 333, 864

García-Burillo S., et al., 2014, A & A, 567, A125

García-González J., et al., 2016, MNRAS, 458, 4512

Gebhardt K., et al., 2000, ApJL, 539, L13

Gelli V., Salvadori S., Ferrara A., Pallottini A., Carniani S., 2023, arXiv e-prints, p. arXiv:2303.13574

Georgiev I. Y., Böker T., Leigh N., Lützgendorf N., Neumayer N., 2016, MNRAS, 457, 2122

Ghosh S. K., et al., 2022, Journal of Astrophysics and Astronomy, 43, 77

Giacconi R., Gursky H., Paolini F. R., Rossi B. B., 1962, PRL, 9, 439

González-Martín O., Masegosa J., Márquez I., Guainazzi M., Jiménez-Bailón E., 2009, A & A, 506, 1107

Greene J. E., Ho L. C., 2005, The Astrophysical Journal, 630, 122

Greene J. E., Ho L. C., 2007, ApJ, 670, 92

Greene J. E., Strader J., Ho L. C., 2020, Anu Rev. in Astronomy and Astrophysics., 58, 257

Greenstein J. L., 1963, Nature, 197, 1041

Groves B., Allen M., 2013, ITERA: IDL Tool for Emission-line Ratio Analysis, Astrophysics Source Code Library, record ascl:1307.012 (ascl:1307.012)

Gu Q. S., Huang J. H., de Diego J. A., Dultzin-Hacyan D., Lei S. J., Benítez E., 2001, A & A, 374, 932

Guo Y., et al., 2023, Nature, 624, 53

Gursky H., Kellogg E. M., Leong C., Tananbaum H., Giacconi R., 1971, ApJL, 165, L43

Hägele G. F., Díaz Á. I., Terlevich E., Terlevich R., Pérez-Montero E., Cardaci M. V., 2008, MNRAS, 383, 209

Haidar H., et al., 2024, MNRAS, 532, 4645

Harris J., Zaritsky D., 2009, AJ, 138, 1243

Harrison C., 2014, PhD thesis, Durham University, UK

Harrison C. M., 2017, Nature Astronomy, 1, 0165

Harrison C. M., Alexander D. M., Mullaney J. R., Swinbank A. M., 2014, MNRAS, 441, 3306

Hazard C., Mackey M. B., Shimmins A. J., 1963, Nature, 197, 1037

Heald G., Oosterloo T. A., 2008, in Funes J. G., Corsini E. M., eds, Astronomical Society of the Pacific Conference Series Vol. 396, Formation and Evolution of Galaxy Disks. p. 267 (arXiv:0712.1184)

Heckman T. M., 1980, A & A, 87, 152

Hennig M. G., Riffel R. A., Dors O. L., Riffel R., Storchi-Bergmann T., Colina L., 2018, MNRAS, 477, 1086

Hensler G., 2014, in Ray A., McCray R. A., eds, IAU Symposium Vol. 296, Supernova Environmental Impacts. pp 265–272 (arXiv:1402.0117), doi:10.1017/S1743921313009575

Ho L. C., 2008, Anu Rev. in Astronomy and Astrophysics., 46, 475

Ho L. C., Ulvestad J. S., 2001, ApJ Suppl., 133, 77

Ho I.-T., et al., 2014, Monthly Notices of the Royal Astronomical Society, 444, 3894

Hönig S. F., et al., 2013, ApJ, 771, 87

Hook I. M., Jørgensen I., Allington-Smith J. R., Davies R. L., Metcalfe N., Murowinski R. G., Crampton D., 2004, Pub. Astron. Soc. Pac., 116, 425

Hoyle F., Fowler W. A., 1963, MNRAS, 125, 169

Hummel E., Saikia D. J., 1991, A & A, 249, 43

Husemann B., et al., 2019, ApJ, 879, 75

Ichikawa K., Ricci C., Ueda Y., Matsuoka K., Toba Y., Kawamuro T., Trakhtenbrot B., Koss M. J., 2017, ApJ, 835, 74

Immler S., Pietsch W., Aschenbach B., 1998, A & A, 331, 601

Izumi T., et al., 2023, Science, 382, 554

Järvelä E., Dahale R., Crepaldi L., Berton M., Congiu E., Antonucci R., 2022, A & A, 658, A12

Jarvis M. E., et al., 2019, MNRAS, 485, 2710

Jones S., McHardy I., Moss D., Seymour N., Breedt E., Uttley P., Körding E., Tudose V., 2011a, Monthly Notices of the Royal Astronomical Society, 412, 2641

Jones S., McHardy I., Moss D., Seymour N., Breedt E., Uttley P., Körding E., Tudose V., 2011b, MNRAS, 412, 2641

*Kaiser C. R., Alexander P., 1999, in Giuricin G., Mezzetti M., Salucci P., eds, Astronomical Society of the Pacific Conference Series Vol. 176, Observational Cosmology: The Development of Galaxy Systems. p. 377 (*arXiv:astro-ph/9809110*), doi:10.48550/arXiv.astro-ph/9809110*

Kammoun E. S., et al., 2019, ApJ, 886, 145

Kauffmann G., et al., 2003a, MNRAS, 346, 1055

Kauffmann G., et al., 2003b, Monthly Notices of the Royal Astronomical Society, 346, 1055

Kennicutt Robert C. J., 1998, Anu Rev. in Astronomy and Astrophysics., 36, 189

Kennicutt R. C., Evans N. J., 2012, Anu Rev. in Astronomy and Astrophysics., 50, 531

Kennicutt Robert C. J., et al., 2009, ApJ, 703, 1672

Kewley L. J., Heisler C. A., Dopita M. A., Lumsden S., 2001, ApJ Suppl., 132, 37

Khachikian E. Y., Weedman D. W., 1974a, ApJ, 192, 581

Khachikian E. Y., Weedman D. W., 1974b, ApJ, 192, 581

King A., Pounds K., 2015, Anu Rev. in Astronomy and Astrophysics., 53, 115

Kirk J. G., Guthmann A. W., Gallant Y. A., Achterberg A., 2000, ApJ, 542, 235

Knapen J. H., Arnth-Jensen N., Cepa J., Beckman J. E., 1993, AJ, 106, 56

Kormendy J., Ho L. C., 2013, Anu Rev. in Astronomy and Astrophysics., 51, 511

Koski A. T., 1978, ApJ, 223, 56

Koudmani S., Sijacki D., Smith M. C., 2022, MNRAS, 516, 2112

Kozieł-Wierzbowska D., Vale Asari N., Stasińska G., Herpich F. R., Sikora M., Żywucka N., Goyal A., 2021, ApJ, 910, 64

Kukreti P., Morganti R., Tadhunter C., Santoro F., 2023, A & A, 674, A198

Kumari N., Jana A., Naik S., Nandi P., 2023, MNRAS, 521, 5440

Kuo C. Y., et al., 2011, ApJ, 727, 20

Lal D. V., Shastri P., Gabuzda D. C., 2011, ApJ, 731, 68

Lammers C., Iyer K. G., Ibarra-Medel H., Pacifici C., Sánchez S. F., Tacchella S., Woo J., 2023, ApJ, 953, 26

Law D. R., et al., 2016, AJ, 152, 83

Law D. R., et al., 2022, ApJ, 928, 58

Lee J. C., et al., 2009, ApJ, 706, 599

Leitherer C., et al., 1999, ApJ Suppl., 123, 3

Lemoine-Busserolle M., Comeau N., Kielty C., Klemmer K., Schwamb M. E., 2019, AJ, 158, 153

Leonidaki I., Boumis P., Zezas A., 2013, MNRAS, 429, 189

Liao M., Wang J., Ren W., Zhou M., 2024, MNRAS, 528, 3696

Lira P., Lawrence A., O'Brien P., Johnson R. A., Terlevich R., Bannister N., 1999, MNRAS, 305, 109

Liszt H. S., Dickey J. M., 1995, AJ, 110, 998

Liu T., Wang J.-X., Yang H., Zhu F.-F., Zhou Y.-Y., 2014, ApJ, 783, 106

Lu N. Y., Hoffman G. L., Groff T., Roos T., Lamphier C., 1993, ApJ Suppl., 88, 383

Lu K.-X., et al., 2021, The Astrophysical Journal, 918, 50

Luridiana V., Morisset C., Shaw R. A., 2015, A & A, 573, A42

Lynden-Bell D., 1969, Nature, 223, 690

Magorrian J., et al., 1998, AJ, 115, 2285

Maiolino R., Rieke G. H., 1995, ApJ, 454, 95

Maiolino R., et al., 2012, MNRAS, 425, L66

Maiolino R., et al., 2017, Nature, 544, 202

Marconi A., Hunt L. K., 2003, ApJL, 589, L21

Marquez I., Moles M., 1994, AJ, 108, 90

Márquez I., Masegosa J., González-Martin O., Hernández-Garcia L., Pović M., Netzer H., Cazzoli S., del Olmo A., 2017, Frontiers in Astronomy and Space Sciences, 4, 34

Martin P., 1995, AJ, 109, 2428

Martin D. C., et al., 2005, ApJL, 619, L1

Mathur S., 2000, MNRAS, 314, L17

McGregor P. J., et al., 2003, in Iye M., Moorwood A. F. M., eds, Society of Photo-Optical Instrumentation Engineers (SPIE) Conference Series Vol. 4841, Instrument Design and Performance for Optical/Infrared Ground-based Telescopes. pp 1581–1591, doi:10.1117/12.459448

McHardy I. M., Papadakis I. E., Uttley P., Page M. J., Mason K. O., 2004, MNRAS, 348, 783

Michałowski M. J., et al., 2020, A & A, 642, A84

Miller J. S., Mathews W. G., 1972, ApJ, 172, 593

Minchev I., et al., 2018, MNRAS, 481, 1645

Minkowski R., 1960, ApJ, 132, 908

Molyneux S. J., Harrison C. M., Jarvis M. E., 2019, A & A, 631, A132

Morganti R., Oosterloo T., Oonk J. B. R., Frieswijk W., Tadhunter C., 2015, A & A, 580, A1

Morganti R., Oosterloo T., Tadhunter C., Bernhard E. P., Raymond Oonk J. B., 2021, A & A, 656, A55

Mountrichas G., Buat V., 2023, A & A, 679, A151

Moy E., Rocca-Volmerange B., 2002, A & A, 383, 46

Mukherjee D., Wagner A. Y., Bicknell G. V., Morganti R., Oosterloo T., Nesvadba N., Sutherland R. S., 2018, MNRAS, 476, 80

Mullaney J. R., Alexander D. M., Fine S., Goulding A. D., Harrison C. M., Hickox R. C., 2013, MNRAS, 433, 622

Mundell C. G., Pedlar A., Shone D. L., Robinson A., 1999, Monthly Notices of the Royal Astronomical Society, 304, 481

Murphy E. J., et al., 2011, ApJ, 737, 67

Musiimenta B., et al., 2023, A & A, 679, A84

Nandi P., Stalin C. S., Saikia D. J., Muneer S., Mountrichas G., Wylezalek D., Sagar R., Kissler-Patig M., 2023a, ApJ, 950, 81

Nandi P., et al., 2023b, ApJ, 959, 116

Nandi P., Stalin C. S., Dam P., Saikia D. J., 2024, arXiv e-prints, p. arXiv:2406.18103

Nandi P., Stalin C. S., Saikia D. J., 2025, ApJ under review

Nardini E., Risaliti G., 2011, MNRAS, 417, 2571

Nesvadba N. P. H., Bicknell G. V., Mukherjee D., Wagner A. Y., 2020, A & A, 639, L13

Nyland K., et al., 2017, ApJ, 845, 50

O'Dea C. P., Saikia D. J., 2021, A & A Rev., 29, 3

Oke J. B., 1963, Nature, 197, 1040

Oke J. B., 1990, AJ, 99, 1621

Onken C. A., Bian F., Fan X., Wang F., Wolf C., Yang J., 2020, MNRAS, 496, 2309

Osterbrock D. E., Ferland G. J., 2006, Astrophysics of gaseous nebulae and active galactic nuclei

Osterbrock D. E., Pogge R. W., 1985, ApJ, 297, 166

Padovani P., 2017, Nature Astronomy, 1, 0194

Pan H.-A., Kuno N., 2017, ApJ, 839, 133

Panessa F., Baldi R. D., Laor A., Padovani P., Behar E., McHardy I., 2019, Nature Astronomy, 3, 387

Papadakis I. E., Ioannou Z., Brinkmann W., Xilouris E. M., 2008, A & A, 490, 995

Parkash V., Brown M. J. I., Jarrett T. H., Bonne N. J., 2018, ApJ, 864, 40

Parlanti E., et al., 2024, arXiv e-prints, p. arXiv:2407.19008

Paturel G., Petit C., Prugniel P., Theureau G., Rousseau J., Brouty M., Dubois P., Cambrésy L., 2003, A & A, 412, 45

Paulino-Afonso A., Sobral D., Darvish B., Ribeiro B., Smail I., Best P., Stroe A., Cairns J., 2020, A & A, 633, A70

Pedlar A., Howley P., Axon D. J., Unger S. W., 1992, MNRAS, 259, 369

Penny S. J., et al., 2018, MNRAS, 476, 979

Pérez-Torres M. A., Alberdi A., 2007, MNRAS, 379, 275

Peterson B. M., 1997, An Introduction to Active Galactic Nuclei. Cambridge, New York Cambridge University Press

Peterson B. M., 2014, Space Sci. Rev., 183, 253

Peterson B. M., et al., 2000, ApJ, 542, 161

Peterson B. M., et al., 2005, ApJ, 632, 799

Peterson B. M., et al., 2014, ApJ, 795, 149

Pounds K. A., Reeves J. N., King A. R., Page K. L., 2004, MNRAS, 350, 10

Prabhu T. P., 2014, Proceedings of the Indian National Science Academy Part A, 80, 887

Ramos Almeida C., et al., 2022, A & A, 658, A155

Rampadarath H., et al., 2018, Monthly Notices of the Royal Astronomical Society, 476, 2876

Reines A. E., 2022, Nature Astronomy, 6, 26

Renzini A., Peng Y.-j., 2015, ApJL, 801, L29

Rieke G. H., et al., 2004, ApJ Suppl., 154, 25

Riffel R. A., et al., 2021, MNRAS, 501, L54

Riffel R., et al., 2022, MNRAS, 512, 3906

Riffel R. A., et al., 2023, MNRAS, 521, 1832

Risaliti G., Elvis M., Fabbiano G., Baldi A., Zezas A., 2005, ApJL, 623, L93

Risaliti G., et al., 2009, ApJ, 696, 160

Rodriguez Espinosa J. M., Rudy R. J., Jones B., 1987, ApJ, 312, 555

*Roy A. L., Wilson A. S., Ulvestad J. S., Colbert J. M., 2000, in Conway J. E., Polatidis A. G., Booth R. S., Pihlström Y. M., eds, EVN Symposium 2000, Proceedings of the 5th european VLBI Network Symposium. p. 7 (*arXiv:astro-ph/0009408*), doi:10.48550/arXiv.astro-ph/0009408*

Rusinek K., Sikora M., Kozieł-Wierzbowska D., Godfrey L., 2016, Monthly Notices of the Royal Astronomical Society, 466, 2294

Sabater J., et al., 2019, A & A, 622, A17

Saikia D. J., Pedlar A., Unger S. W., Axon D. J., 1994, MNRAS, 270, 46

Saikia D. J., Jeyakumar S., Mantovani F., Salter C. J., Spencer R. E., Thomasson P., Wiita P. J., 2003, PASA, 20, 50

Saikia P., Körding E., Coppejans D. L., Falcke H., Williams D., Baldi R. D., Mchardy I., Beswick R., 2018, A & A, 616, A152

Salem N., Masters K. L., Stark D. V., Sharma A., 2024, Research Notes of the American Astronomical Society, 8, 188

Salim S., et al., 2007, ApJ Suppl., 173, 267

Salpeter E. E., 1964, ApJ, 140, 796

Sánchez-Portal M., Díaz Á. I., Terlevich E., Terlevich R., 2004, MNRAS, 350, 1087

Sánchez S. F., et al., 2022, ApJ Suppl., 262, 36

Sandage A., Bedke J., 1994, The Carnegie atlas of galaxies. Vol. 638

Sandqvist A., Joersaeter S., Lindblad P. O., 1995, A & A, 295, 585

Sargent A. J., Fischer T. C., Johnson M. C., van der Horst A. J., Secrest N. J., Shuvo O. I., Cigan P. J., Smith K. L., 2024, ApJ, 961, 230

Sarzi M., et al., 2002, ApJ, 567, 237

Schmidt M., 1963, Nature, 197, 1040

Schmidt M., Green R. F., 1983, ApJ, 269, 352

Schutte Z., Reines A. E., 2022, Nature, 601, 329

Seifina E., Chekhtman A., Titarchuk L., 2018, A & A, 613, A48

Seyfert C. K., 1943, ApJ, 97, 28

Shin J., Woo J.-H., Chung A., Baek J., Cho K., Kang D., Bae H.-J., 2019, ApJ, 881, 147

Singh A., Gulati M., Bagla J. S., 2019, MNRAS, 489, 5582

Skrutskie M. F., et al., 2006, AJ, 131, 1163

Slavcheva-Mihova L., Mihov B., 2011, A & A, 526, A43

Slipher V. M., 1917, Proceedings of the American Philosophical Society, 56, 403

Smirnova K. I., Wiebe D. S., Moiseev A. V., Jozsa G. I. G., 2020, Astrophysical Bulletin, 75, 234

Smith F. G., 1951, Nature, 168, 555

Spindler A., et al., 2018, MNRAS, 476, 580

Springob C. M., Haynes M. P., Giovanelli R., Kent B. R., 2005, ApJ Suppl., 160, 149

Stalevski M., Ricci C., Ueda Y., Lira P., Fritz J., Baes M., 2016, MNRAS, 458, 2288

Stalevski M., Tristram K. R. W., Asmus D., 2019, MNRAS, 484, 3334

Stevens I. R., Forbes D. A., Norris R. P., 1999, MNRAS, 306, 479

Su R., et al., 2023, MNRAS, 520, 5712

Sutherland R., Dopita M., Binette L., Groves B., 2013, MAPPINGS III: Modelling And Prediction in PhotoIonized Nebulae and Gasdynamical Shocks, Astrophysics Source Code Library, record ascl:1306.008 (ascl:1306.008)

Swanenburg B. N., et al., 1978, Nature, 275, 298

Sweet S. M., Fisher D., Glazebrook K., Obreschkow D., Lagos C., Wang L., 2018, ApJ, 860, 37

Tadhunter C., 2016, A & A Rev., 24, 10

Tandon S. N., et al., 2020, AJ, 159, 158

Terashima Y., Kunieda H., Misaki K., 1999, Pub. Astron. Soc. Japan, 51, 277

Thim F., Hoessel J. G., Saha A., Claver J., Dolphin A., Tammann G. A., 2004, AJ, 127, 2322

Tody D., 1986, in Crawford D. L., ed., Society of Photo-Optical Instrumentation Engineers (SPIE) Conference Series Vol. 627, Instrumentation in astronomy VI. p. 733, doi:10.1117/12.968154

Torres-Papaqui J. P., Coziol R., Robleto-Orús A. C., Cutiva-Alvarez K. A., Roco-Avilez P., 2024, AJ, 168, 37

Tortosa A., et al., 2018, MNRAS, 473, 3104

Troyer J., Starkey D., Cackett E. M., Bentz M. C., Goad M. R., Horne K., Seals J. E., 2016, MNRAS, 456, 4040

Tsai M., Hwang C.-Y., 2015, AJ, 150, 43

Tucker W., Kellogg E., Gursky H., Giacconi R., Tananbaun H., 1973, ApJ, 180, 715

Tueller J., Mushotzky R. F., Barthelmy S., Cannizzo J. K., Gehrels N., Markwardt C. B., Skinner G. K., Winter L. M., 2008, ApJ, 681, 113

Ulrich M.-H., Maraschi L., Urry C. M., 1997, Anu Rev. in Astronomy and Astrophysics., 35, 445

Ulvestad J. S., Wilson A. S., 1984, ApJ, 285, 439

Urbanik M., Klein U., Graeve R., 1986, A & A, 166, 107

Urry C. M., Padovani P., 1995, Pub. Astron. Soc. Pac., 107, 803

Veilleux S., Kim D. C., Sanders D. B., Mazzarella J. M., Soifer B. T., 1995, ApJ Suppl., 98, 171

Veilleux S., Bland-Hawthorn J., Cecil G., 1999, AJ, 118, 2108

Venturi G., et al., 2021, A & A, 648, A17

Venturi G., et al., 2023, A & A, 678, A127

Verley S., Corbelli E., Giovanardi C., Hunt L. K., 2009, A & A, 493, 453

Véron-Cetty M. P., Véron P., 2006, A & A, 455, 773

Virtanen P., et al., 2020, Nature Methods, 17, 261

Vukotic B., Bojicic I., Pannuti T. G., Urosevic D., 2005, Serbian Astronomical Journal, 170, 101

Wake D. A., et al., 2017, AJ, 154, 86

Waller W. H., 1990, Pub. Astron. Soc. Pac., 102, 1217

Wang J., Risaliti G., Fabbiano G., Elvis M., Zezas A., Karovska M., 2010, The Astrophysical Journal, 714, 1497

Weiler K. W., van der Hulst J. M., Sramek R. A., Panagia N., 1981, ApJL, 243, L151

Weisskopf M. C., Brinkman B., Canizares C., Garmire G., Murray S., Van Speybroeck L. P., 2002, Pub. Astron. Soc. Pac., 114, 1

Wells D. C., 1985, in di Gesu V., Scarsi L., Crane P., Friedman J. H., Levialdi S., eds, Data Analysis in Astronomy. p. 195

Westfall K. B., et al., 2019, AJ, 158, 231

Whitmore B. C., et al., 2023, ApJL, 944, L14

Whittle M., Silverman J. D., Rosario D. J., Wilson A. S., Nelson C. H., 2004, in Storchi-Bergmann T., Ho L. C., Schmitt H. R., eds, Vol. 222, The Interplay Among Black Holes, Stars and ISM in Galactic Nuclei. pp 299–302, doi:10.1017/S1743921304002315

Wilkins S. M., et al., 2024, MNRAS, 527, 7965

Williams D. R. A., et al., 2017, MNRAS, 472, 3842

Wolfinger K., Kilborn V. A., Koribalski B. S., Minchin R. F., Boyce P. J., Disney M. J., Lang R. H., Jordan C. A., 2013, MNRAS, 428, 1790

Woltjer L., 1959, ApJ, 130, 38

Woo J.-H., Bae H.-J., Son D., Karouzos M., 2016, ApJ, 817, 108

Woo J.-H., Cho H., Gallo E., Hodges-Kluck E., Le H. A. N., Shin J., Son D., Horst J. C., 2019, Nature Astronomy, 3, 755

Wright E. L., et al., 2010, AJ, 140, 1868

Wrobel J. M., Ho L. C., 2006, ApJL, 646, L95

Wrobel J. M., Fassnacht C. D., Ho L. C., 2001, ApJL, 553, L23

Wylezalek D., Morganti R., 2018, Nature Astronomy, 2, 181

Xu X., Wang J., 2022, ApJ, 933, 110

Xu C., Livio M., Baum S., 1999, AJ, 118, 1169

Yang J., et al., 2022, MNRAS, 514, 6215

Zakamska N. L., Greene J. E., 2014, MNRAS, 442, 784

Zamanov R., Marziani P., Sulentic J. W., Calvani M., Dultzin-Hacyan D., Bachev R., 2002, ApJL, 576, L9

Zel'dovich Y. B., Novikov I. D., 1964, Soviet Physics Doklady, 9, 246

Zhang L., Ho L. C., 2023, ApJL, 953, L9

Zhang K., Wang T.-G., Yan L., Dong X.-B., 2013, ApJ, 768, 22

Zhuang M.-Y., Ho L. C., 2023, Nature Astronomy, 7, 1376

de Vaucouleurs G., de Vaucouleurs A., Corwin Herold G. J., Buta R. J., Paturel G., Fouque P., 1991, Third Reference Catalogue of Bright Galaxies. Springer

do Nascimento J. C., et al., 2022, MNRAS, 513, 807

van der Marel R. P., Alves D. R., Hardy E., Suntzeff N. B., 2002, AJ, 124, 2639

von Montigny C., et al., 1995, ApJ, 440, 525